Title
Metal-templated assembly of protein cages

Permalink
https://escholarship.org/uc/item/5sh0826r

Author
Huard, Dustin Johnathen Edward

Publication Date
2012

Peer reviewed|Thesis/dissertation

UNIVERSITY OF CALIFORNIA, SAN DIEGO

Metal-Templated Assembly of Protein Cages

A dissertation submitted in partial satisfaction of the
requirements for the degree of Doctor of Philosophy
in
Chemistry

by

Dustin Johnathen Edward Huard

Committee in charge:

Professor F. Akif Tezcan, Chair
Professor Michael Burkart
Professor Clifford Kubiak
Professor Melvin Okamura
Professor Yitzhak Tor

2012

The dissertation of Dustin Johnathen Edward Huard is approved, and it is acceptable in quality and form for publication on microfilm and electronically:

Chair

University of California, San Diego

2012

DEDICATION

I dedicate this dissertation to my parents, Edward and Robin Huard, for their continual love and support throughout my academic journey. My family is my source of inspiration and keeps me moving in the right direction in life. I also dedicate this dissertation to my friends, who are my surrogate family when I am away from home.

EPIGRAPH

The truth may be puzzling. It may take some work to grapple with. It may be counterintuitive. It may contradict deeply held prejudices. It may not be consonant with what we desperately want to be true. But our preferences do not determine what's true. We have a method, and that method helps us to reach not absolute truth, only asymptotic approaches to the truth–never there, just closer and closer, always finding vast new oceans of undiscovered possibilities. Cleverly designed experiments are the key.

Carl Edward Sagan

TABLE OF CONTENTS

LIST OF ABBREVIATIONS

Å	Angstrom
Aβ	amyloid-β
CD	circular dichroism
CID	chemically induced dimerization
Cys	cysteine
$\Delta G_{folding}$	folding free energy
ΔH_{vH}	change in van’t Hoff transition enthalpy
DNA	deoxyribonucleic acid
DOTA	1,4,7,10-tetraazacyclododecane-1,4,7,10-tetraacetic acid
Dps	DNA-binding protein from starved cells
DTPA	diethylenetriaminepentaacetic acid
DTT	dithiothreitol, or (2S,3S)-1,4-bis(sulfanyl)butane-2,3-diol
EDTA	2,2’,2’’,2’’’-(ethane-1,2-diyldinitriolo)tetraacetic acid
f/f_o	frictional ratio
FPLC	fast liquid protein chromatography
f_{Ft}	fraction of total folded protein
f_U	fraction unfolded
GuHCl	guanidine hydrochloride
$[GuHCl]_u$	guanidine hydrochloride unfolding midpoint
H-bond	hydrogen bond
hemin	ferriprotoporphyrin IX
hGH	human growth hormone
His	histidine

HuHF	human H-ferritin
IAEDANS	5-({2-[iodoacetyl)amino]ethyl}amino)naphthalene-1-sulfonic acid
ICP-OES	inductively coupled plasma-optical emission spectroscopy
IPTG	isopropyl β-D-1-thiogalactopyranoside
LB	Luria-Bertani
MALDI-TOF	matrix-assisted laser desorption/ionization time-of-flight
MDPSA	metal-directed protein self-assembly
MeTIR	metal-templated interface redesign
MIC1	metal-induced cage variant 1
MME	monomethyl ether
MOF	metal-organic framework
MRI	magnetic resonance imaging
MRW	mean residue molar weight
NaP_i	sodium phosphate monobasic
NMR	nuclear magnetic resonance
PDB	Protein Data Bank
PEG	polyethylene glycol
PMSF	phenylmethanesulfonyl fluoride
PPI	protein-protein interaction
P_t	total protein concentration
RI	radial invariant
rMeTIR	reverse metal-templated interface redesign
rpm	rotations per minute
SDS-PAGE	sodium dodecyl sulfate polyacrylamide gel electrophoresis

SSRL	Stanford Synchrotron Radiation Laboratory
SV	sedimentation velocity
TEM	transmission electron microscopy
$[\theta]$	molar ellipticity
$[\theta]_{obs}$	measured ellipticity
TI	time invariant
T_m	thermal melting point
Tris	2-amino-2-hydroxymethyl-propane-1,3-diol
UV	ultraviolet
Vbar	partial specific volume

LIST OF FIGURES

LIST OF TABLES

ACKNOWLEDGEMENTS

There are many, many people that deserve acknowledgment and credit for their kindness, support, and guidance in helping me become the person I am today. First and foremost I would like to thank my family, especially my mother and father, who are always willing to stand by me and help give me the inspiration and motivation to always move forward towards accomplishing my goals. They will never fully understand the depth of love and gratitude I have for them and my appreciation of their support.

Throughout my academic experiences, I have made some very wonderful friends who deserve accolades for their support and the happiness they have brought into my life. My friends have been my family, most especially since I have been moored in San Diego. I am constantly drawing inspiration from them, and I appreciate their willingness to put up with me no matter how graduate-student-like I have become. Never have I met a group of people that love to laugh so much, and that bring me laughter and joy.

I would be nowhere in this PhD experience without my advisor, Dr. Akif Tezcan. He has been a terrific mentor, and I thank him very much for sharing his wisdom and mentorship with me. He has put up with me through the highs and lows of graduate school, and I thank him for not giving up on me. Also, many thanks must be extended to my Doctoral Committee members, for their continued support and mentorship.

The people that deserve perhaps the most thanks throughout my academic experiences at UCSD are my fellow Tezcan Laboratory members. These people deserve an award for tolerating me and the crazy energy I am sure I bring into the lab

space for so many hours and for so many years. From them, I have learned many important life lessons, and I have found great friendships. I have had the great pleasure of mentoring several students, Stanley, Kathy, Vanna, Thuy, Allen, and Katie, and they have all made my life in the laboratory a lot of fun.

Chapters 1-4 present materials that this author significantly contributed to as both an author and a researcher. The material has been submitted for publication to Nature Chemical Biology, in “Engineering Chemical Control into Protein-Protein Interactions: Copper-Templated Ferritin Cage Assembly”, with shared authorship with K. M. Kane and F. A. Tezcan.

Chapter 5 presents materials that this author significantly contributed to as a researcher, with contributions from K. M. Kane and F. A. Tezcan. The subject matter has not yet been organized for publication.

VITA

2005 Bachelors of Science, Chemistry, Seattle University, Seattle, WA

2007 Masters of Science, Chemistry, University of California, San Diego, CA

2012 Doctor of Philosophy, Chemistry, University of California, San Diego, CA

PUBLICATIONS

Huard, D. J. E., Kane, K. M., Tezcan, F. A. 2012. Engineering Chemical Control into Protein-Protein Interactions: Copper-Templated Ferritin Cage Assembly. Submitted for publication to Nature Chemical Biology.

FIELDS OF STUDY

Major Field: Chemistry

Chemistry: Biochemistry, Bioinorganic Chemistry, and Organic Chemistry

HONORS AND AWARDS

2011 Congratulatory TA Letter for Winter Quarter

ABSTRACT OF THE DISSERTATION

Metal-Templated Assembly of Protein Cages

by

Dustin Johnathen Edward Huard
Doctor of Philosophy in Chemistry
University of California, San Diego, 2012

Professor F. Akif Tezcan, Chair

The ability to chemically control protein-protein interactions would allow the interrogation of dynamic cellular processes, and lead to better understanding and exploitation of self-assembled protein architectures. Yet, the direct incorporation of a simple chemical switch into highly evolved, finely tuned and extensive protein-protein interfaces is a tremendous design challenge. Here we introduce a new engineering strategy–reverse metal-templated interface redesign (rMeTIR)–which transforms a natural protein-protein interface into one that only engages in selective response to a metal ion. We have applied rMeTIR to render the self-assembly of the cage-like protein human H-ferritin controllable specifically by Cu^{II} binding, which has allowed for the first time: a) the study of the structure and stability of the isolated ferritin monomer, b) the demonstration of the primary role of peripheral H-bonding

interactions in providing geometric specificity for cage assembly, and c) the modification of the interior of the ferritin cage under physiological conditions via an active encapsulation mechanism. Significantly, Cu^{II} acts as a structural template for ferritin assembly in a manner that is highly reminiscent of nucleotide sequences that template virus capsid formation, and we are employing its capacity to facilitate monomer-to-cage formation for the purposes of exploring the ferritin assembly mechanism and furthering materials applications of the ferritin nanocage.

Chapter 1.

Introduction

Protein-protein interactions (PPIs) are central to the governance of all cellular processes. PPIs range in breadth from being responsible for the functioning of dynamic cellular networks and processes to the assembly of complex biological machinery. The ability to assert control over such interactions is an attractive goal, the result of which would provide, through the manipulation and interrogation of cellular processes, an improved understanding and eventual exploitation of self-assembled protein systems.[1-3]

The task of rendering PPIs controllable with external stimuli is not straightforward. As in the case of designing PPIs from first principles, the challenge arises from the fact that PPIs are mediated by a concert of weak, non-covalent interactions spread out over large surface areas (typically >1000 Å^2).[4] The prediction and programming of numerous weak interactions, as required by *de novo* PPI design, is highly challenging.[5, 6] Conversely, the challenge in rendering PPIs externally controllable lies in redesigning a stable interface such that the non-covalent interactions that constitute it can be engaged or disengaged *en masse* in response to a given environmental cue.

Given the difficulty in designing PPIs, the dearth in the literature devoted to external control of PPIs is unsurprising. One strategy in particular has met with a degree of success in this arena, the so-called chemically induced dimerization, or CID, paradigm.[2] CID operates by proximity-driven dimerization of two proteins co-localized by a bifunctional ligand. The ligand can be homo- or hetero-bifunctional, resulting in the production of either homo- or heterodimeric species (Figure 1.1 A). This technique was pioneered by Schreiber and Crabtree, who initially used the bivalent ligand drug FK1012 to homodimerize FKBP12 fused to the proximity-regulated ζ-chain of the T-cell receptor, with the consequence of activating the endogenous signal transduction cascade (Figure 1.1 B).[7] CID has since been employed to control protein subcellular localization[8, 9] and gene expression[10-13], and for drug discovery[14-17] purposes.

One caveat of CID and related methodologies is that control exerted over PPIs is somewhat “indirect” in the sense that often there is the requirement that external interaction modules are fused to targeted proteins.[7, 18-22] Functionality therefore relies on these peripheral moieties, as exemplified above by the ζ-chain fusion, and not necessarily the ligand-dimerized components. These strategies do not strictly impose the correct geometric engagement of protein partners, which is important for most PPI-dependent cellular processes, and absolutely required for the formation of multiprotein assemblies.

The direct integration of a chemical switch into a site of protein-protein contact is a demanding task. Only a single example exists in the literature reporting the induction of PPIs with a small molecule switch: Schultz and co-workers showed that human growth hormone (hGH) could be induced to bind its receptor (both proteins were engineered at their interfaces to decrease binding energy) with the addition of 5-chloro-2-trichloromethyl benzimidazole, a small molecule that acts to repack the variant PPI interface and confer functionality.[23] Considering the design of chemical inducer systems, the switch must provide sufficient interactions with both proteins to afford enough driving force to replace many native non-covalent interactions at the interface. Additionally, the driving force must overcome the entropic cost associated with a switch from a binary to a ternary system. Also, and importantly, the chemical inducer must not interrupt the native geometric alignment of the protein-protein interface.

Metal ions are capable of satisfying the aforementioned requirements of chemical inducers of PPIs. Metal coordination to amino acid side chains can provide significantly higher binding energies in comparison to non-covalent interactions that generally comprise PPIs. At the same time, metal ion coordination is capable of imposing strict stereochemical bonding restraints, even at the level of protein surfaces. This was demonstrated previously in the Tezcan laboratory, where divalent late-first-row transition metal ions, through coordination with engineered surface residues on cytochrome cb_{562}, successfully organized the natively monomeric protein into discrete supramolecular assemblies.[24-26] The oligomerization states of the metal-driven assemblies reflect the respective coordination geometry preferences of the metals bound. For example, with the same protein building block (MBPC-1), Cu^{II} gave rise to square planar-derived dimers, Ni^{II} yielded octahedral-inspired trimers, and Zn^{II} resulted in tetrahedral-based tetramers (Figure 1.2).

Aside from providing strong and directionally specific interactions, metal ions provide additional benefits as inducers of PPIs.[27] The bonds between metal ions and ligands can be kinetically labile, thereby affording PPIs to proceed under thermodynamic rather than kinetic control. Metal coordination by default introduces chemical control into PPIs, and it can be modulated through external factors including competing ligands or chelators, or pH. Finally, metal ions have intrinsic reactivities, which can be incorporated into protein-protein interfaces to build additional functionality.

Metal-directed protein self-assembly (MDPSA), in its most distilled form, reminisces of supramolecular coordination chemistry.[28, 29] In this vein of thought, proteins can essentially be thought of as bulky, multifunctional ligands, or building blocks. Metal ions can be employed to direct the organization of these proteinaceous building blocks to construct higher-ordered assemblies or architectures[30] in a manner controlled by the stereochemical preference of the metal (Figure 1.3).[26] Provided the appropriate selection and design of the “ligand” and metal ion, the resulting architectures should be fairly predictable and reflect a high degree of rational design.

Applying the approach of MDPSA by treating protein building blocks as ligands for metal ions, the Tezcan laboratory was able to demonstrate that a monomeric, natively non-self-associating protein, cytochrome *cb*$_{562}$, could be evolved systematically into a self-associating protein.[31, 32] To achieve this evolution, the strategy of metal-templated interface redesign (MeTIR) was developed (Figure 1.4). Cytochrome *cb*$_{562}$, a four-helix bundle protein, was first modified through site-directed mutagenesis to display metal-chelating groups on its surface. Interaction of this mutein with metal ions yielded protein oligomers with newly established protein-protein interfaces. The metal-mediated PPI interfaces were then stabilized through the installation of complementary interactions; this phase of interface redesign was accomplished through the RosettaDesign algorithm.[33] Ultimately, through minimization of electrostatic and steric mismatches and incorporation of hydrophobic interactions, self-association between protein monomers was achieved independently of metal binding. Importantly, with the elimination of obligate metal binding to trigger protein self-association, alternate metal ions can, post PPI-driven organization, be incorporated into the protein complex, allowing the construction of new metal-based functionalities.

Goals of Dissertation

The successful application of metal coordination to control protein self-assembly (MDPSA) and to create new PPIs (MeTIR) from monomeric proteins led us to ask whether similar principles can be utilized to control the assembly and the disassembly of naturally self-assembling protein complexes. Specifically, we wanted to assert chemical control over the hollow, cage-like proteins. Cage-like protein structures such as ferritin,[34] carboxysomes,[35] the small heat shock proteins[36], and virus capsids[37] are constructed from a minimal number of protein building blocks by virtue of their several self-interacting surfaces that produce highly-cooperative, symmetrical assemblies. Cage-like proteins encapsulate endogenous substrates, and have functional roles including cellular iron and oxygen management[38, 39], RuBisCO sequestration for enhanced CO_2 fixation[40, 41], molecular chaperoning and protein folding[42, 43], and nucleic acid packaging[44].

The ability to render protein cage assembly externally inducible is an attractive goal from both fundamental and practical perspectives. Fundamentally, protein cage formation, which involves the simultaneous engagement of several PPI surfaces, is complex and difficult to study.[45] In some instances (such as in the case of ferritin assembly) this is due to the experimental challenge in isolating the monomeric protein building blocks and the lack of an external means of initiating or controlling cage formation under physiologically relevant conditions.[46, 47] As a target for PPI redesign, the interfaces of protein cages provide a particularly stringent test: the correct geometric alignment of each interface is a strict requirement for the proper orientation of all other subunit contacts. Aside from validation of MDPSA as a powerful tool for exploring complex natural systems, a potential benefit of applying this paradigm to ferritin or other cage-like assemblies is insight into the mechanism of how these systems become organized *in vivo*; assembly processes are often poorly understood, and, in the case of ferritin, canonically disputed.[48]

From a practical standpoint, the ability to assert chemical control over protein cage-like architectures provides a direct means of manipulating a host of favorable attributes that these systems proffer. Properties including high degrees of symmetry, solubility, stability, monodispersity, biocompatibility, and ease of genetic and chemical manipulation[37, 49] have led to a diversity of applications of protein cages in nanoparticle assembly,[50, 51] catalysis,[52, 53] biological imaging,[54, 55] single-molecule molecular studies,[56] and selective protein entrapment.[57] An important practical limitation of protein cages is that most are isolated in already-assembled forms, thereby restricting the size and type of cargo that can be loaded inside. A selection of protein cages exist that have the capacity to disassemble and reassemble *in vitro* under benign conditions. Yet, these systems suffer from setbacks including low stability and large pore sizes that preclude true isolation within their interior.[58, 59] Although the pH-induced disassembly of a cage-like protein system (pyruvate dehydrogenase) has been achieved through the engineering of its interfaces[60], we know of no reports on engineered “inducible assembly”. The major goal of this dissertation was to achieve chemical control over the assembly and disassembly of a prototypical protein cage, the human H-ferritin (HuHF) and gain chemical access to its interior for applications purposes.

The strategy we developed to engineer external control of HuHF cage assembly is a reinterpretation of MeTIR. We envisioned that the optimal way to earn true access to the core of HuHF would be through direct manipulation of monomeric ferritin. Since HuHF exists as a 24-mer upon isolation, we sought to use reverse metal-templated interface redesign, or rMeTIR, as a means with which to access monomeric ferritin; the monomerized protein would display engineered moieties capable of responding to external stimuli, thereby triggering cage assembly (Figure 1.4). Metal ions would be the chemical inducers of oligomerization, and the first stage of rMeTIR requires the grafting of metal-binding sites at the PPI interfaces of HuHF. Key complimentary interactions at these interfaces are then eliminated, resulting in a metal-responsive variant of HuHF that only forms a protein cage upon a metal-binding event satisfying geometrical constraints.

With the advent of top-down, metal-directed protein self-assembly achieved through rMeTIR, we wish to extend the idea of controlling protein-protein interactions with metal ions to other biologically relevant systems with potential for gains in fundamental knowledge and practical applications. The rMeTIR scheme should be wholly generalizable in the context of symmetric protein systems, allowing for the potential probing of a host of PPIs with the eventual aim of their exploitation. In the context of HuHF and other cage-like systems, the ability to externally manipulate the self-assembly of nanocage building blocks provides a handle with which to access the core interiors with the possibility of an expanded set of substrates for new applications and functionalities.

Chapter 1 is reproduced in part with permission from: Huard, D. J. E., Kane, K. M., Tezcan, F. A. 2012. “Engineering Chemical Control into Protein-Protein Interactions: Copper-Templated Ferritin Cage Assembly.” In revision for publication in Nature Chemical Biology.

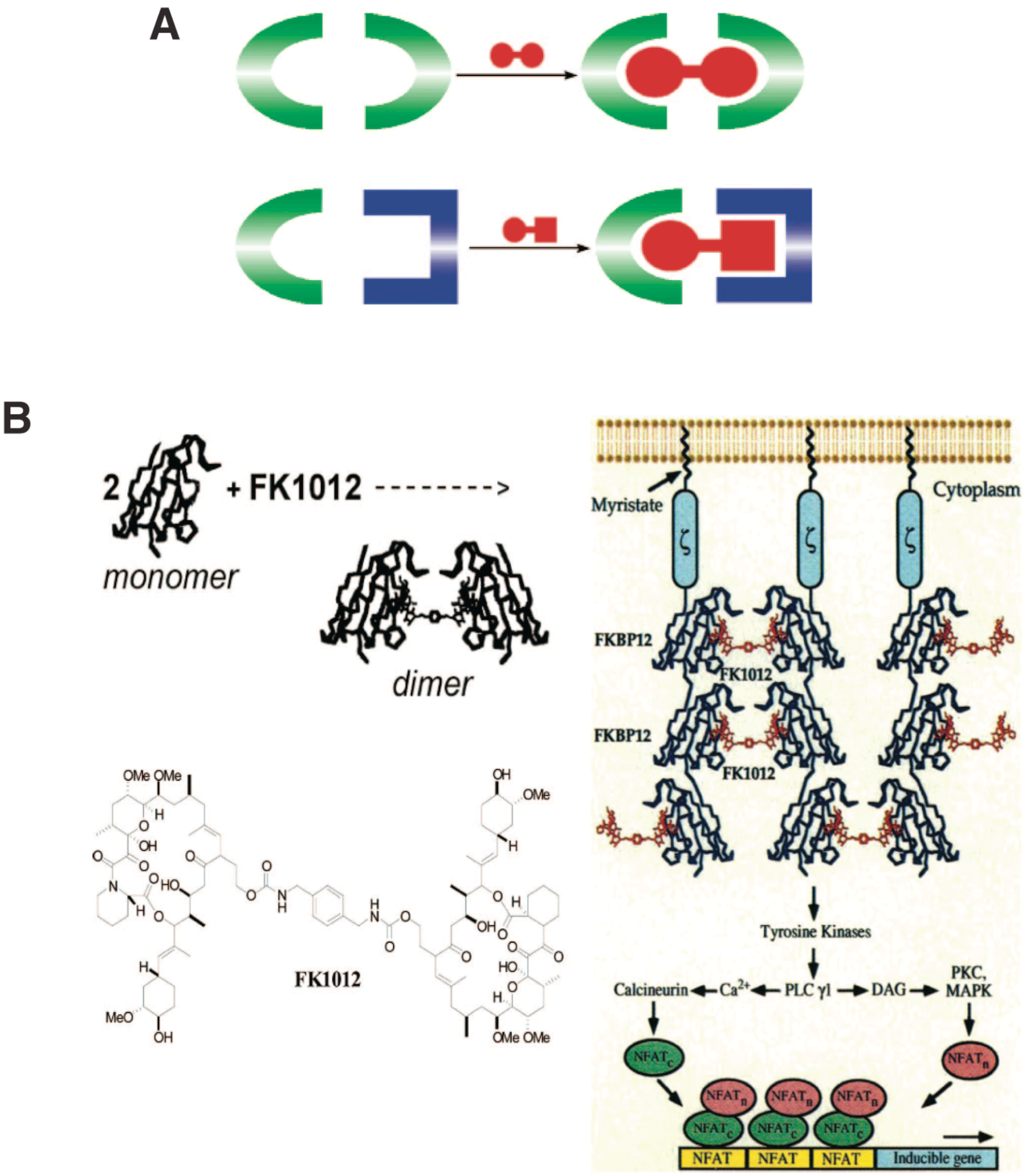

Figure 1.1. Illustration of the chemically induced dimerization, or CID, scheme. A) Cartoon depiction of the CID strategy, resulting in protein homodimerization (top) or heterodimerization (bottom) depending on ligand choice (adapted from reference 2). B) Employing CID to activate a signal transduction cascade through FK1012-mediated dimerization of FKBP12 protein (adapted from reference 2).

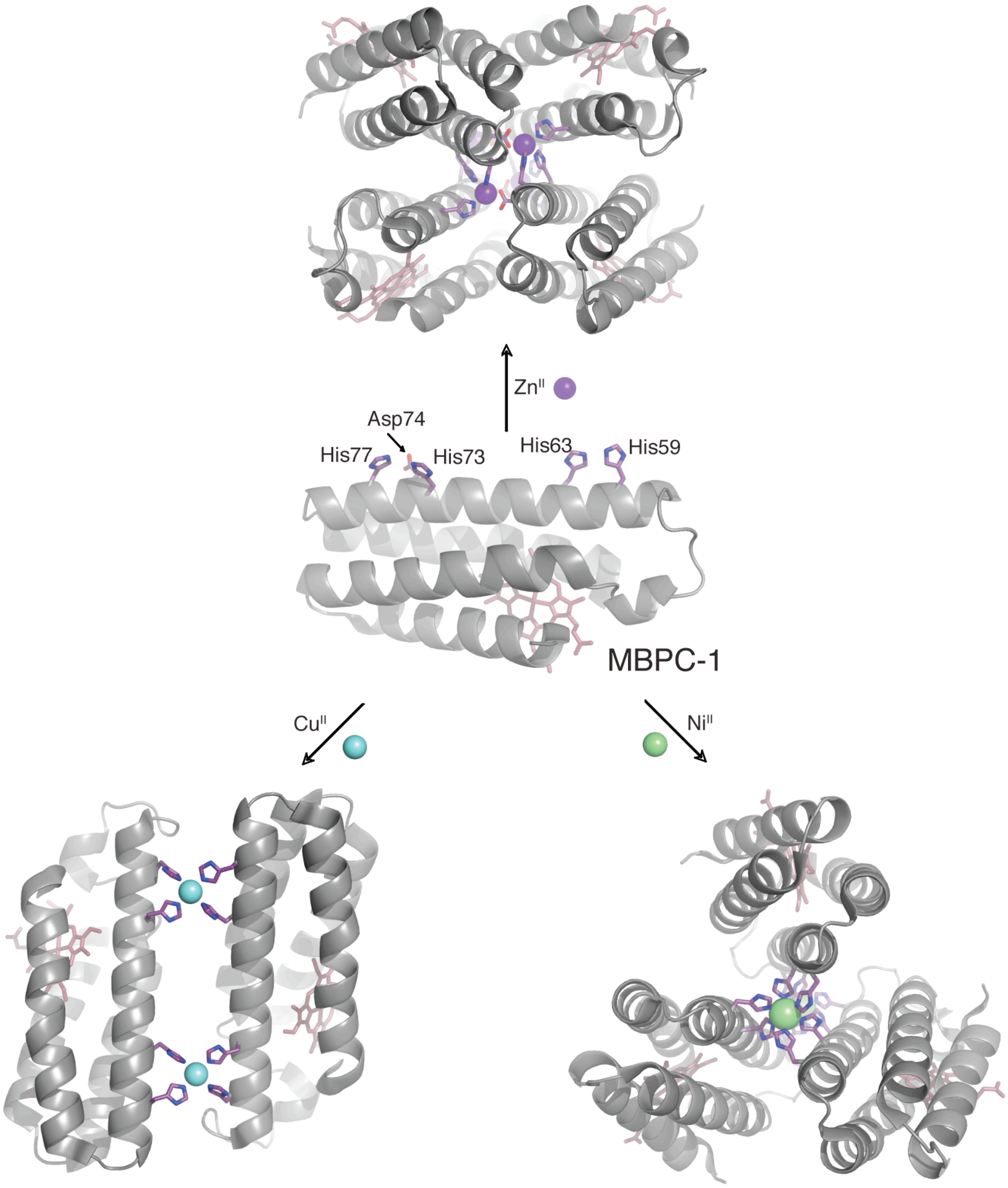

Figure 1.2. Metal-dependent oligomerization states of cytochrome *cb*$_{562}$ variant MBPC-1. Geometric preferences of various divalent late-first-row transition metals manifest in metal-mediated MBPC-1 dimers with Cu^{II} (PDB ID: 3DE8), trimers with Ni^{II} (PDB ID: 3DE9), and tetramers with Zn^{II} (PDB ID: 2QLA) upon protein crystallization (adapted from references 24 and 26).

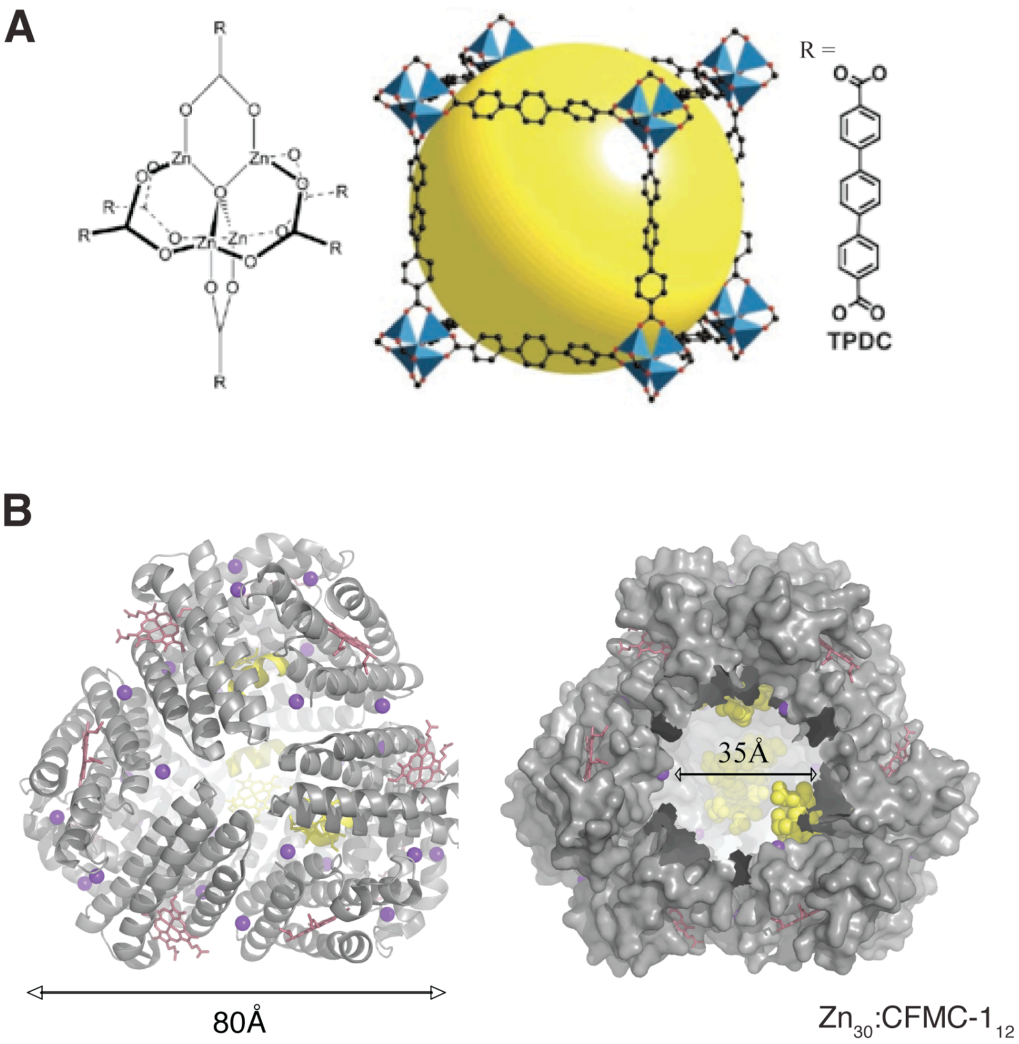

Figure 1.3. Drawing parallels between metal-organic frameworks (MOFs) and protein superstructures consisting of protein building blocks organized by metal-directed protein self-assembly. A) Cubic framework MOF based on dicarboxylate linker TPDC and octahedral $Zn_4O(carboxylate)_6$ secondary building unit, with van der Waals cavity space highlighted in yellow (adapted from references 28 and 29). B) Cytochrome cb_{562} variant CFMC-1 organized by Zn^{II} ions (purple spheres) into a novel tetrahedral superprotein architechture with stoichiometry Zn_{30}:CFMC-1_{12} and encapsulated microperoxidase $MP9_{cb562}$ in yellow (adapted from reference 30).

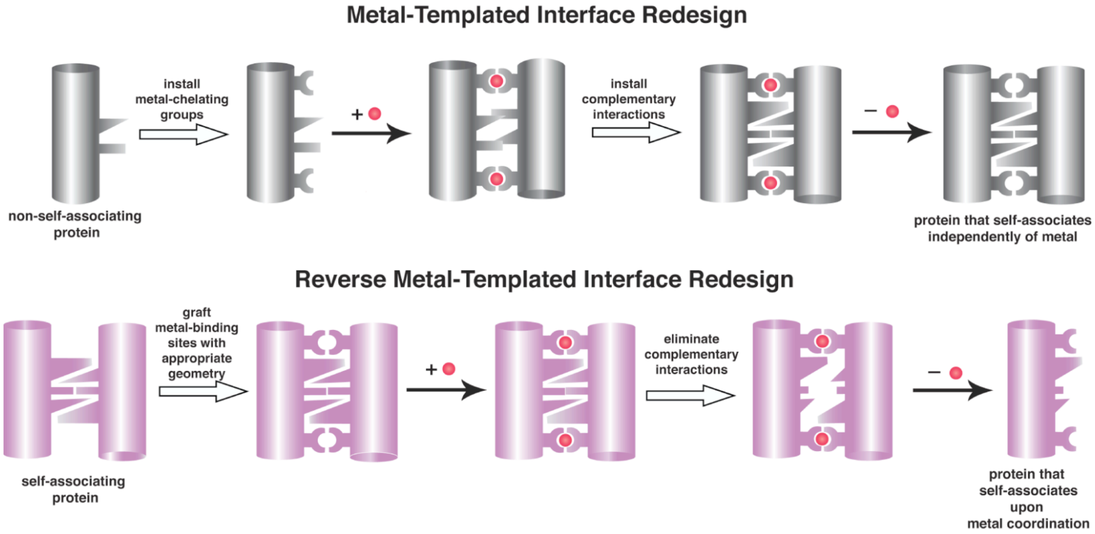

Figure 1.4. Comparative schemes for Metal-Templated Interface Redesign (MeTIR, top) and Reverse Metal-Templated Interface Redesign (rMeTIR, bottom). Actions designated with open arrows correspond to structurally-guided engineering steps. Red spheres indicate metal ions.

References

1. Klemm, J.D., S.L. Schreiber, and G.R. Crabtree, *Dimerization as a regulatory mechanism in signal transduction.* Annual Review of Immunology, 1998. **16**: p. 569-592.

2. Fegan, A., et al., *Chemically Controlled Protein Assembly: Techniques and Applications.* Chemical Reviews, 2010. **110**(6): p. 3315-3336.

3. Corson, T.W., N. Aberle, and C.M. Crews, *Design and Applications of Bifunctional Small Molecules: Why Two Heads Are Better Than One.* ACS Chemical Biology, 2008. **3**(11): p. 677-692.

4. Jones, S. and J.M. Thornton, *Principles of protein-protein interactions.* Proceedings of the National Academy of Sciences of the United States of America, 1996. **93**(1): p. 13-20.

5. Kortemme, T. and D. Baker, *Computational design of protein-protein interactions.* Current Opinion in Chemical Biology, 2004. **8**(1): p. 91-97.

6. Karanicolas, J. and B. Kuhlman, *Computational design of affinity and specificity at protein-protein interfaces.* Current Opinion in Structural Biology, 2009. **19**(4): p. 458-463.

7. Spencer, D.M., et al., *Controlling Signal-Transduction with Synthetic Ligands.* Science, 1993. **262**(5136): p. 1019-1024.

8. Johnston, J., et al., *Regulated expression of erythropoietin from an AAV vector safely improves the anemia of beta-thalassemia in a mouse model.* Molecular Therapy, 2003. **7**(4): p. 493-497.

9. Rivera, V.M., et al., *Regulation of protein secretion through controlled aggregation in the endoplasmic reticulum.* Science, 2000. **287**(5454): p. 826-830.

10. Liberles, S.D., et al., *Inducible gene expression and protein translocation using nontoxic ligands identified by a mammalian three-hybrid screen.* Proceedings of the National Academy of Sciences USA, 1997. **94**(15): p. 7825-7830.

11. Pollock, R., et al., *Delivery of a stringent dimerizer-regulated gene expression system in a single retroviral vector.* Proceedings of the National Academy of Sciences USA, 2000. **97**(24): p. 13221-13226.

12. Pollock, R. and V.M. Rivera, *Regulation of gene expression with synthetic dimerizers.* Methods in Enzymology, 1999. **306**: p. 263-281.

13. Rivera, V.M., *Controlling Gene Expression Using Synthetic Ligands.* Methods, 1998. **14**: p. 421-429.

14. Becker, F., et al., *A three-hybrid approach to scanning the proteome for targets of small molecule kinase inhibitors.* Chemistry & Biology, 2004. **11**(2): p. 211-223.

15. Firestine, S.M., et al., *Using an AraC-based three-hybrid system to detect biocatalysts in vivo.* Nature Biotechnology, 2000. **18**(5): p. 544-547.

16. Henthorn, D.C., A.A. Jaxa-Chamiec, and E. Meldrum, *A GAL4-based yeast three-hybrid system for the identification of small molecule-target protein interactions.* Biochemical Pharmacology, 2002. **63**(9): p. 1619-1628.

17. Koide, K., et al., *A synthetic library of cell-permeable molecules.* Journal of the American Chemical Society, 2001. **123**(3): p. 398-408.

18. Farrar, M.A., J. Alberolalla, and R.M. Perlmutter, *Activation of the Raf-1 kinase cascade by coumermycin-induced dimerization.* Nature, 1996. **383**(6596): p. 178-181.

19. Lin, H.N., et al., *Dexamethasone-methotrexate: An efficient chemical inducer of protein dimerization in vivo.* Journal of the American Chemical Society, 2000. **122**(17): p. 4247-4248.

20. Gendreizig, S., M. Kindermann, and K. Johnsson, *Induced protein dimerization in vivo through covalent labeling.* Journal of the American Chemical Society, 2003. **125**(49): p. 14970-14971.

21. Stankunas, K., et al., *Conditional protein alleles using knockin mice and a chemical inducer of dimerization.* Molecular Cell, 2003. **12**(6): p. 1615-1624.

22. Hussey, S.L., S.S. Muddana, and B.R. Peterson, *Synthesis of a beta-estradiol-biotin chimera that potently heterodimerizes estrogen receptor and streptavidin proteins in a yeast three-hybrid system.* Journal of the American Chemical Society, 2003. **125**(13): p. 3692-3693.

23. Guo, Z.H., D.M. Zhou, and P.G. Schultz, *Designing small-molecule switches for protein-protein interactions.* Science, 2000. **288**(5473): p. 2042-2045.

24. Salgado, E.N., J. Faraone-Mennella, and F.A. Tezcan, *Controlling protein-protein interactions through metal coordination: Assembly of a 16-helix bundle protein.* Journal of the American Chemical Society, 2007. **129**(44): p. 13374-13375.

25. Salgado, E.N., et al., *Metal-mediated self-assembly of protein superstructures: Influence of secondary interactions on protein oligomerization and aggregation.* Journal of the American Chemical Society, 2008. **130**(19): p. 6082-6084.

26. Salgado, E.N., et al., *Control of Protein Oligomerization Symmetry by Metal Coordination: C(2) and C(3) Symmetrical Assemblies through Cu(II) and Ni(II) Coordination.* Inorganic Chemistry, 2009. **48**(7): p. 2726-2728.

27. Salgado, E.N., R.J. Radford, and F.A. Tezcan, *Metal-Directed Protein Self-Assembly.* Accounts of Chemical Research, 2010. **43**(5): p. 661-672.

28. Eddaoudi, M., et al., *Systematic design of pore size and functionality in isoreticular MOFs and their application in methane storage.* Science, 2002. **295**(5554): p. 469-472.

29. James, S.L., *Metal-organic frameworks.* Chemical Society Reviews, 2003. **32**(5): p. 276-288.

30. Ni, T.W. and F.A. Tezcan, *Structural characterization of a microperoxidase inside a metal-directed protein cage.* Angewandte Chemie International Edition (English), 2010. **49**(39): p. 7014-7018.

31. Salgado, E.N., et al., *Metal templated design of protein interfaces.* Proceedings of the National Academy of Sciences of the United States of America, 2010. **107**(5): p. 1827-1832.

32. Brodin, J.D., et al., *Evolution of Metal Selectivity in Templated Protein Interfaces.* Journal of the American Chemical Society, 2010. **132**(25): p. 8610-8617.

33. Liu, Y. and B. Kuhlman, *RosettaDesign server for protein design.* Nucleic Acids Research, 2006. **34**: p. 235-238.

34. Liu, X.F. and E.C. Theil, *Ferritins: Dynamic management of biological iron and oxygen chemistry.* Accounts of Chemical Research, 2005. **38**(3): p. 167-175.

35. Tanaka, S., et al., *Atomic-level models of the bacterial carboxysome shell.* Science, 2008. **319**(5866): p. 1083-1086.

36. Kim, K.K., R. Kim, and S.H. Kim, *Crystal structure of a small heat-shock protein.* Nature, 1998. **394**(6693): p. 595-599.

37. Douglas, T. and M. Young, *Viruses: Making friends with old foes.* Science, 2006. **312**(5775): p. 873-875.

38. Theil, E.C., *Ferritin protein nanocages use ion channels, catalytic sites, and nucleation channels to manage iron/oxygen chemistry.* Current Opinion in Chemical Biology, 2011. **15**(2): p. 304-311.

39. Calhoun, L.N. and Y.M. Kwon, *Structure, function and regulation of the DNA-binding protein Dps and its role in acid and oxidative stress resistance in Escherichia coli: a review.* Journal of Applied Microbiology, 2011. **110**(2): p. 375-386.

40. Cannon, G.C., et al., *Microcompartments in prokaryotes: carboxysomes and related polyhedra.* Applied and Environmental Microbiology, 2001. **67**(12): p. 5351-5361.

41. Shively, J.M., et al., *Functional organelles in prokaryotes: polyhedral inclusions (carboxysomes) of Thiobacillus neapolitanus.* Science, 1973. **182**(4112): p. 584-586.

42. Borges, J.C. and C.H. Ramos, *Protein folding assisted by chaperones.* Protein and Peptide Letters, 2005. **12**(3): p. 257-261.

43. Walter, S. and J. Buchner, *Molecular chaperones--cellular machines for protein folding.* Angewandte Chemie International Edition (English), 2002. **41**(7): p. 1098-1113.

44. Speir, J.A. and J.E. Johnson, *Nucleic acid packaging in viruses.* Current Opinion in Structural Biology, 2012. **22**(1): p. 65-71.

45. Zlotnick, A., *To Build a Virus Capsid - an Equilibrium-Model of the Self-Assembly of Polyhedral Protein Complexes.* Journal of Molecular Biology, 1994. **241**(1): p. 59-67.

46. Stefanini, S., P. Vecchini, and E. Chiancone, *On the Mechanism of Horse Spleen Apoferritin Assembly - a Sedimentation-Velocity and Circular-Dichroism Study.* Biochemistry, 1987. **26**(7): p. 1831-1837.

47. Gerl, M., et al., *Self-Assembly of Apoferritin from Horse Spleen after Reversible Chemical Modification with 2,3-Dimethylmaleic Anhydride.* Biochemistry, 1988. **27**(11): p. 4089-4096.

48. Gerl, M. and R. Jaenicke, *Mechanism of the Self-Assembly of Apoferritin from Horse Spleen - Cross-Linking and Spectroscopic Analysis.* European Biophysics Journal with Biophysics Letters, 1987. **15**(2): p. 103-109.

49. Vriezema, D.M., et al., *Self-assembled nanoreactors.* Chemical Reviews, 2005. **105**(4): p. 1445-1489.

50. Wong, K.K.W., et al., *Biomimetic synthesis and characterization of magnetic proteins (magnetoferritin).* Chemistry of Materials, 1998. **10**(1): p. 279-285.

51. Butts, C.A., et al., *Directing Noble Metal Ion Chemistry within a Designed Ferritin Protein.* Biochemistry, 2008. **47**(48): p. 12729-12739.

52. Ueno, T., et al., *Size-selective olefin hydrogenation by a Pd nanocluster provided in an apo-ferritin cage.* Angewandte Chemie-International Edition, 2004. **43**(19): p. 2527-2530.

53. Abe, S., et al., *Polymerization of Phenylacetylene by Rhodium Complexes within a Discrete Space of apo-Ferritin.* Journal of the American Chemical Society, 2009. **131**(20): p. 6958-6960.

54. Aime, S., L. Frullano, and S.G. Crich, *Compartmentalization of a gadolinium complex in the apoferritin cavity: A route to obtain high relaxivity contrast agents for magnetic resonance imaging.* Angewandte Chemie-International Edition, 2002. **41**(6): p. 1059-1061.

55. Uchida, M., et al., *Targeting of cancer cells with ferrimagnetic ferritin cage nanoparticles.* Journal of the American Chemical Society, 2006. **128**(51): p. 16626-16633.

56. Comellas-Aragones, M., et al., *A virus-based single-enzyme nanoreactor.* Nature Nanotechnology, 2007. **2**(10): p. 635-639.

57. Worsdorfer, B., K.J. Woycechowsky, and D. Hilvert, *Directed Evolution of a Protein Container.* Science, 2011. **331**(6017): p. 589-592.

58. Johnson, E., et al., *Crystal structures of a tetrahedral open pore ferritin from the hyperthermophilic Archaeon Archaeoglobus fulgidus.* Structure, 2005. **13**(4): p. 637-648.

59. Bancroft, J.B., *The Self-Assembly of Spherical Plant Viruses.* Advances in Virus Research, 1970. **16**: p. 99-134.

60. Dalmau, M., S.R. Lim, and S.W. Wang, *Design of a pH-Dependent Molecular Switch in a Caged Protein Platform.* Nano Letters, 2009. **9**(1): p. 160-166.

Chapter 2.

Generation of Metal-Responsive HuHF Building Blocks: Designing Metal-Induced Cage Variant 1 (MIC1)

Introduction

HuHF belongs to the class of maxi-ferritins, ubiquitous cage-like proteins responsible for iron sequestration and storage.[1] HuHF is comprised of 24 four-helix bundle monomers, which are arranged in octahedral (432) symmetry (Figure 2.1) to yield a roughly spherical cage with an inner diameter of 8 nm and an outer diameter of 12 nm.[2] The tight, cooperative packing arrangement of ferritin not only affords its high chemical and thermal stability,[3-5] but also results in the creation of small (<4 Å) pores along its C_3 and C_4 symmetry axes. These pores restrict access of natural substrates (Fe^{II} and O_2) as well as other small species, including metal ions and small metal complexes, into and out of the HuHF cavity.[6-11]

Canonically, the encapsulation of larger species within ferritin requires complete disassembly of the ferritin shell at pH 2, followed by cage reassembly at neutral pH in the presence of guest molecules.[12] This strategy is low-yielding, as it relies on passive encapsulation for molecular entrapment, and suffers from material loss due to protein precipitation from extreme pH changes.[13] Importantly, the acidic conditions requisite for ferritin cage disassembly preclude protocols for the covalent or coordinative coupling of desired substrates to the subunit monomer surfaces, thereby limiting the scope of ferritin and its homologs as nanovessels.

The ability to access the inner core of HuHF depends on the capacity to directly manipulate the monomeric building blocks of the nanocage. Towards this end, reverse metal-templated interface redesign, an extension of metal-directed protein self-assembly developed in the Tezcan laboratory,[14] was applied to the HuHF system. The rMeTIR strategy allows for the redesign of a stable protein-protein interface such that PPIs at that interface become dependent upon a controllable, theoretically reversible metal binding event. With this methodology, the diversity of ferritin cargo may be expanded upon resulting from access to HuHF monomers, and therefore the potential applications for cage-like proteins such as ferritin broaden in foreseeable scope.

The first step in the process of rMeTIR requires the grafting of metal-binding sites onto the surface of a target protein. The location of the chelating moieties must be selected such that, with a given metal ion, the appropriate geometric preference of the metal can dictate the recapturing of the native PPI. Following the establishment that metal binding occurs at the installed sites, complementary interactions that drive PPIs at the protein-protein interface are abolished; only upon metal coordination does self-association yet again occur, and in a chemically-controlled manner.

HuHF nanocages have octahedral symmetry, and therefore offer several interfaces that pose potential sites of modification. For the purposes of rMeTIR, the C_2 interface was focused on: it has substantially more buried surface area (2900 $Å^2$) than the 3- and 4-fold interfaces, and is more tailorable when considering redesign. Also, it has been demonstrated that C_2 dimers are key intermediates in the assembly mechanism of ferritin cage formation.[15-17] Thus, the C_2 interface acts as both a thermodynamic and a kinetic gatekeeper for ferritin assembly. Preventing a dimerization event in the absence of metal binding through rMeTIR should abolish PPIs responsible for the 24-meric nanovessel formation, rendering the HuHF building blocks completely monomerized and amenable to modification.

Materials and Methods

Site-Directed mutagenesis and protein expression, purification, and characterization. DNA coding for wild-type HuHF was obtained directly from DNA 2.0 (Menlo Park, CA) on a pJexpress bacterial vector optimized for expression in *E. coli* and equipped with ampicillin resistance. Ferritin variants were prepared employing QuikChange mutagenesis (Stratagene) with primers from Integrated DNA Technologies. Mutant plasmids were transformed into XL-1 Blue *E. coli* cells and purified using the QIAprep Spin Miniprep kit (Qiagen). Sequencing of variant plasmids was performed by Retrogen. Mutant DNA was transformed into BL21 (DE3) *E. coli* cells, and plated on LB agar containing 100 μg/mL ampicillin. Plates were grown overnight at 37 °C typically for 15 hours.

Individual mutant colonies were utilized to prepare starter cultures for larger-scale bacterial growths and protein preparation. Starter cultures consisted of 35 mL of LB media supplemented with 35 μL of a 100 μg/mL stock of ampicillin. The miniature culture growths were initiated by the addition of a single mutant colony; the cultures were allowed to grow 15 hours with shaking at 220 rpm at a temperature of 37 °C. At this point, 10 mL volumes of miniature culture were utilized to inoculate 1 L quantities of media for preparative bacterial growths (the 1 L growths consisted of LB media with 100 mg/L ampicillin added). Scale-up cultures were then shaken again at 37 °C at a speed of 220 rpm for approximately 4 hours, until the OD_{600} reached the range of 0.6-0.8. Cells were then induced with 1 mM IPTG (Gold Biotechnology) and allowed to grow 4 hours prior to harvesting. Cells were pelleted via centrifugation (centrifugation occurred with a speed of 4,000 rpm at 4 °C for 10 minutes) and stored at -80 °C until immediately before work-up.

Bacteria cell harvesting was initiated by thawing the variant cell pellets. The pellets were then dissolved in minimal standard buffer, which consists of 15 mM Tris buffered at pH 7.4 and supplemented with 150 mM NaCl. To this mixture, 10 mM EDTA and 1 mM PMSF were added, and then the cells were lysed via sonication for 12 minutes on ice. The lysate was centrifuged for 10 minutes at 10,000 rpm at 4 °C, and the supernatant and pellet separated. Some variant species, including 4His-ΔC*, could be isolated in the supernatant and further purified at this point. The majority of mutants, however, including MIC1, remained in inclusion body pellets, and required further work-up for complete solubilization.

The preparation of the variants isolated in inclusion bodies began by re-suspension of the pellets in standard buffer containing 1 mM PMSF, 5 mM DTT, 10 mM EDTA, ~25 μM lysozyme, and ~32 nM DNase. After 30 minutes of incubation at room temperature, 1% vol/vol Triton X-100 was added to the mixture, followed by an additional 7 minutes of sonication over ice. The suspension was centrifuged as before, and the resulting pellet washed twice with standard buffer containing 1 mM PMSF, 10 mM EDTA, and 1% vol/vol Triton X-100. The inclusion body pellet was then treated by addition of a minimal volume of 8 M urea buffered with 50 mM Tris, set at pH 8.0, and also containing 100 mM NaCl, 100 mM PMSF, and 1 mM EDTA. After an hour of incubation in this urea-containing buffer, if insoluble material persisted, 9 volumes of a 50 mM KH_2PO_4 buffer, maintained at pH 10.7, with 50 mM NaCl and 1 mM EDTA was added to fully dissolve the pellet (Figure 2.2 A). If necessary, the mixture was treated with NaOH to ensure the pH remained at 10.7. After 30 minutes of incubation at high pH, the pH was adjusted back to 7.4, and the inclusion body mixture dialyzed exhaustively against standard buffer to remove EDTA and any remaining DTT. Finally, the proteins were exchanged into 8 M urea buffered with 20 mM NaH_2PO_4 at pH 7.4 and containing 1 M NaCl for purification.

The solubilized HuHF variant proteins were purified through the utilization of fast protein liquid chromatography (FPLC) on a DuoFlow workstation (Bio-Rad). Initially, the proteins were purified via metal-affinity chromatography with a HisPrep FF 16/10 column (FE Healthcare) charged with $CuSO_4$, running an imidazole gradient of 0 to 0.25 M in the aforementioned urea buffer (Figure 2.2 B, C). The gradient was performed in 2% incremental steps, with each step lasting a total volume of 45 mL. After this initial purification step, proteins were exhaustively exchanged, through dialysis, into the standard buffer containing 10 mM EDTA. These conditions allow for protein renaturation in a metal-free environment.

The 4His-ΔC* variant, which was isolated in a self-assembled form containing mineralized iron, was further purified to 80-85% purity via a heat step and treated according to previously published protocols[7] for iron removal. The heat step involved ramping the protein to temperatures ≥60 °C for 10 minutes, followed by centrifugation (at a speed of 10,000 rpm at 4 °C for 10 minutes) to remove precipitated protein impurities. Apo-ferritins were prepared, in brief, by dialyzing the protein against a 10 mM sodium acetate buffer maintained at pH 5.5, containing sodium dithionite, $Na_2S_2O_4$, as reductant, followed by chelation with 2,2'-bipyridyl. Protein variants purified in this manner, including 4His-ΔC*, were ultimately exchanged back into standard buffer with 10 mM EDTA for storage purposes.

The HuHF variants isolated from inclusion bodies, such as MIC1, due to their inherent instability, unfolded more completely in the urea-containing buffer utilized in their purification. This propensity toward unfolding allowed for tighter binding to the metal-affinity column, which manifested in higher concentrations of imidazole required for release, and consequently enhanced purity was attained for these proteins. (The more-stable variants, including 4His-ΔC*, elute at similar imidazole concentrations to undesired protein impurities.) Therefore, no heating step was required for further purification. However, a proportion of the mutated proteins, upon purification, existed in misfolded, aggregate states that behooved removal prior to experimentation. Elimination of the aggregated protein was performed using size exclusion chromatography on an XK26/100 column (GE Healthcare) packed with Ultrogel AcA 34 resin (Pall Corporation) running on the standard buffer containing 10 mM EDTA (Figure 2.2 D). In all cases, protein purity was confirmed with SDS-PAGE gel electrophoresis and MALDI-TOF mass spectrometry (Figure 2.2 C, E).

X-ray crystallography. Protein crystals of Cu^{II}-bound 4His-ΔC* were obtained by the sitting-drop vapor diffusion method. The sitting drops yielding diffraction-quality crystals consisted of 2 μL of protein solution and 2 μL of precipitant solution. The wells contained 500 μL of precipitant solution. The protein solution was made of 712 μM of apo-4His-ΔC* in standard buffer. The precipitant consisted of 50 mM Tris buffered at pH 8.0, with 5 mM $CaCl_2$ and 200 μM $CuCl_2$. The crystals grew at room temperature within a one-month period. For cryoprotection, ~1 μL of glycerol was added directly to the 4-μL well solution containing crystals, and the crystals were pulled through this glycerol layer and immediately frozen in liquid N_2.

X-ray diffraction data were collected at 100 K at Beamline 9-2 of the Stanford Synchrotron Radiation Laboratory (SSRL) using 0.98-Å radiation. Data were also collected at the Cu K-edge (1.3 Å) to identify Cu centers through anomalous scattering. Diffraction data were processed using MOSFLM and SCALA.[18] Structures were solved with molecular replacement by MOLREP[19] using the structure of the K86Q[2] mutant (PDB ID: 2CEI) as a model. Rigid-body, positional and thermal refinement was carried out using REFMAC,[20] along with iterative manual model building with COOT.[21] Atomic coordinates and structure factors have been deposited into the Protein Data Bank with the identification number 4DYX. All structural figures were produced using PYMOL.[22]

Analytical ultracentrifugation. Sedimentation velocity (SV) measurements were performed using a Beckman-Optima XL-I Analytical Ultracentrifuge equipped with an An-60 Ti rotor. Protein samples were prepared in standard buffer; for metal-free samples, 10 mM EDTA was included. Typically, the protein concentration utilized was 50 μM as determined by Bradford assay. During experiments screening for Cu^{II}-induced oligomerization of variants, $CuCl_2$ was added to equimolar concentrations with the protein, allowing for at least 30 minutes of metal-protein interaction prior to initiation of centrifugation. The wavelength used for sample detection was 280 nm, and the instrument was run at 41,000 rpm with the temperature set at 25 °C.

All data were processed using the program SEDFIT,[23] employing a continuous c(s) model. Key buffer properties, including density and viscosity, were calculated with SEDNTERP (http://www.jphilo.mailway.com). The partial specific volumes of ferritin variants and theoretical sedimentation coefficients of their oligomers were calculated with HYDROPRO.[24] Data were processed with SEDFIT first by setting the bottom of the cell and sample meniscus parameters. Then, buffer-related properties, along with the protein partial specific volume, were fixed. After complete parameterization, the baseline correction constant was optimized over all data scans with the “Run” command; this step was performed with a 95% confidence level. The time invariant (TI) and radial invariant (RI) systemic noise were then similarly optimized. The weight-averaged frictional ratio (f/f_o) of the sample was next determined using the “Fit” command with a confidence level of 0%; f/f_o was floated from 1.2 until a consensus value was reached. Lastly, a final distribution was obtained after executing the “Run” command with the confidence level increased back to 95%.

Results and Discussion

The first phase of rMeTIR: grafting metal coordination sites onto the surface of HuHF results in the preparation of Cu^{II}-coordinating 4His-ΔC.* The C_2 interface of HuHF was initially targeted for reverse metal-templated interface redesign (Figure 2.3). The immediate goal of this re-design was to engineer a variant of ferritin capable of nanocage formation only in the presence of metal ions; hence, protein oligomerization state is rendered chemically controllable. The first step of rMeTIR involves the installation of metal-binding groups onto the surface of the C_2 interface of HuHF such that metal chelation might be employed to eventually trigger a dimerization event. Previously in the lab, it was showed that Cu^{II} preferentially promoted the C_2-symmetric dimerization of another four-helix bundle protein (cytochrome cb_{562}) through formation of two square planar coordination motifs that consisted of two pairs of surface His residues placed at i, i+4 positions.[25] Using the metrics from these low-energy Cu^{II} coordination sites (including various pairwise C_α and C_β distances between the His residues) as a search criterion (Figure 2.4 A), the C_2 PPI interface of HuHF was scanned for potential sites of metal-chelation group grafting.

Sites 56/60 and 63’/67’ at the dimerization interface, which lie across from each other, were identified as target positions for His-clamp installation (Figure 2.4 B). Modification of these residues (residue 60 is a His in the native protein) to His presents two symmetrically related Cu^{II} coordination sites. The recombinant variant

ΔC*[17] was utilized as a starting platform for rMeTIR engineering. This mutant is devoid of any Cys residues (which precludes the possibility of disulfide bond formation and therefore unwanted, non-specific oligomerization) and contains the K86Q mutation (Figure 2.5) that facilitates ferritin protein crystallization[2], while being essentially indistinguishable from wild type HuHF in terms of assembly, stability, and function. The variant thus prepared with Cu-binding motifs is termed 4His-ΔC*.

The amino acid substitutions to obtain 4His-ΔC* eliminate a number of conserved hydrophobic packing and H-bonding interactions, particularly those involving R63 and E67 (Figure 2.3). Nevertheless, 4His-ΔC* remains capable of self-assembling into a nanocage with Fe mineralization functionality, as indicated by the fact that the mutant is extracted from *E. coli* cells as a soluble, brown-colored lysate. The crystal structure of 4His-ΔC* was determined at 1.8 Å resolution (see Table 2.1 for refinement statistics). An examination of the C_2 interface reveals that the two Cu-4His coordination sites form as planned, in a slightly distorted square planar arrangement (Figure 2.6 A, B). The bond distances and angles closely approximate those of the targeted, low-energy Cu^{II} coordination geometry (Figure 2.6 C). Although the crystallization conditions include less than one molar equivalent of Cu^{II} per protein monomer, several Cu ions are observed to be associated with each monomer, and this is likely due to the chelation of Cu by the protein during metal affinity chromatography.

The Cu-coordinated 4His-ΔC* dimers overlay nearly perfectly with their wild-type counterparts (Figure 2.6 D). Indeed, the overall root mean square deviation (rmsd) between the two dimers is 0.25 Å measured over all C_α positions. The only noticeable structural difference is the local ~1-Å widening of the interface near the His residues to accommodate square planar Cu^{II} coordination. All of the secondary interactions in the C_2 interface that fall outside the immediate Cu^{II} coordination environments are maintained. The engineered His residues are largely uninvolved in secondary interactions, with the exception of H67; this residue is H-bonded to Y39 instead of the Glu that it replaced.

The second phase of rMeTIR as applied to HuHF: engineering instability into the C_2 interface of 4His-ΔC to construct metal-responsive ferritin monomers.* Having incorporated low-engery Cu^{II} coordination sites into the C_2 interface of HuHF without perturbing the ferritin nanocage structure, the next phase of rMeTIR was initiated: re-designing the protein-protein interface such that metal binding is requisite for dimerization and the formation of higher-order oligomers. This mode of engineering requires the identification of amino acid residues whose replacement would sufficiently—but not overly—destabilize the dimer interface. Importantly, any alteration should not manifest in the disruption of the native alignment of the C_2 interface, which is required for the proper orientation of the C_3 and C_4 symmetry interfaces at the cage pores. While the native ferritin cage-like architecture is highly robust and can often withstand extensive modifications, evidence exists that even single mutations at key interfacial sites can sometimes abolish cage formation.[26]

Given the variable response of ferritin sensitivity to mutagenesis, a number of C_2-interface variants were prepared, as summarized in Table 2.2. In particular, residues Y39 and N74 were focus targets. These two residues lie near the inner surface of the ferritin shell on Helices B and C, and point away from the core of the C_2 interface; however, Y39 and N74 are still involved in conserved H-bonding interactions (Figure 2.7 A, B). Mutations of the residues that are buried in the dimer interface core were largely avoided (except L28E in variants 8 and 11, and Y32D in variants 3 and 15), along with non-conservative mutations on the BC-loop (except for the I85D mutation in variant 12), with the reasoning that such mutations would not only drastically destabilize the C_2 interface, but also prohibit its correct alignment (Figure 2.7 C). The observation that variants 11 and 12 do not organize into cages under any circumstances accord with this expectation.

The variants were first screened based on their cellular state of assembly as they were overexpressed in *E. coli* cells. The free concentrations of divalent metal ions (Co^{II}, Cu^{II}, Ni^{II}, Zn^{II}) in the cytoplasm are exceedingly low.[27] Therefore, there was no expectation that the variants with the desired metal-switch characteristic would form intact cages in solution, but rather that the muteins would be localized in insoluble aggregates of monomers. Indeed, a majority of the variants were expressed in inclusion bodies, requiring solubilization with urea and high-pH buffer. These proteins were purified via metal-affinity and size-exclusion chromatography prior to further analysis.

In the second stage of screening, the oligomerization states of the purified variants were determined by SV measurements in the presence of EDTA (metal-free conditions) or equimolar Cu^{II}. Based on these experiments, three variants (9, 10, and 13) were identified that showed the desired transition from a monomer to a 24mer upon Cu^{II} binding. Of the metal-responsive HuHF variants, mutant 13 (containing Y39E/N74E/P88A mutations) was chosen to proceed with, as it displayed the greatest propensity toward Cu-driven monomer conversion to ferritin cage; this variant was deemed Metal-Induced Cage Variant 1, or MIC1. The objective with the Y39E and N74E mutations was to both eliminate the native network of H-bonds involving these residues without creating a cavity and introduce repulsive charge interactions involving E39, E74 and D42. The nearly-isosteric P88A mutation on the BC-loop was intended for the entropic destabilization of the C_2 interface, based on the assumption that the conserved P88 residue may be responsible for the pre-organization of the BC-loop for self-assembly (Figure 2.7 D).[28] The MIC1 variant was moved forward with to explore metal-driven ferritin cage assembly.

Alternative Cu^{II}*-binding 4His coordination motif variant 4His-loop-ΔC*.* Concomitant with the preparation of the 4His-ΔC* metal-binding template protein, the C_2 interface of HuHF was scanned for alternative positioning for the grafting of sites of metal coordination during the first phase of rMeTIR. Beyond the A and B helices at this interface, the BC loop comprises considerable interfacial contact, with enough room to accommodate a set of two 4His Cu^{II}-binding motifs (Figure 2.8 A). Residues F81, Q83, K87, and D91 could feasibly be mutated to histidines to prepare two such coordination sites. The metrics of the proposed metal binding sites (Figure 2.8 B) are considerably more snug, based on crystallographic models, than the MBPC-1 and 4His-ΔC* systems (refer to Figure 2.4). However, it was hypothesized that the potential flexibility of the BC loop region, in solution, would allow for square planar Cu^{II} binding. Several variants containing the loop-clamp mutations 81/83/87/91H were prepared. All, including those with rMeTIR secondary phase perturbation mutations, proved soluble and 24-meric in solution. Due to the success found with the 4His-ΔC* template, particularly in the form of MIC1, further exploration of the 4His-loop-ΔC* variants was aborted.

Conclusions

Our initial experimental objective was to render the oligomerization state of cage-like protein HuHF externally controllable through the design strategy of rMeTIR. The first step of rMeTIR calls for the grafting of metal-chelating moieties onto the surface of a protein at the protein-protein interface, with the intention of using metal binding to drive PPIs. The C_2 interface was targeted for installation of His residues at i, i+4 positions at sites 56/60 and 63'/67' on the template protein ΔC*. The crystal structure of this 4His-ΔC* variant, determined from protein crystals grown in the presence of Cu^{II}, indicated that Cu was bound as planned in a slightly distorted square planar arrangement with the Cu-His_4 coordination motif.

After incorporating low-energy Cu^{II} coordination sites into the C_2 interface of HuHF, the dimerization surface of 4His-ΔC* was scanned for residues whose replacement would perturb the natural PPIs that drive cage formation such that in the absence of metal ions, only HuHF monomers would exist. Several variants were identified having the desired chemical switch characteristic of metal-induced cage formation, the most promising of which included the mutations Y39E/N74E/P88A. We chose this variant, referred to as MIC1, to proceed with for further characterization and applications.

Chapter 2 is reproduced in part with permission from: Huard, D. J. E., Kane, K. M., Tezcan, F. A. 2012. "Engineering Chemical Control into Protein-Protein Interactions: Copper-Templated Ferritin Cage Assembly." In revision for publication in Nature Chemical Biology.

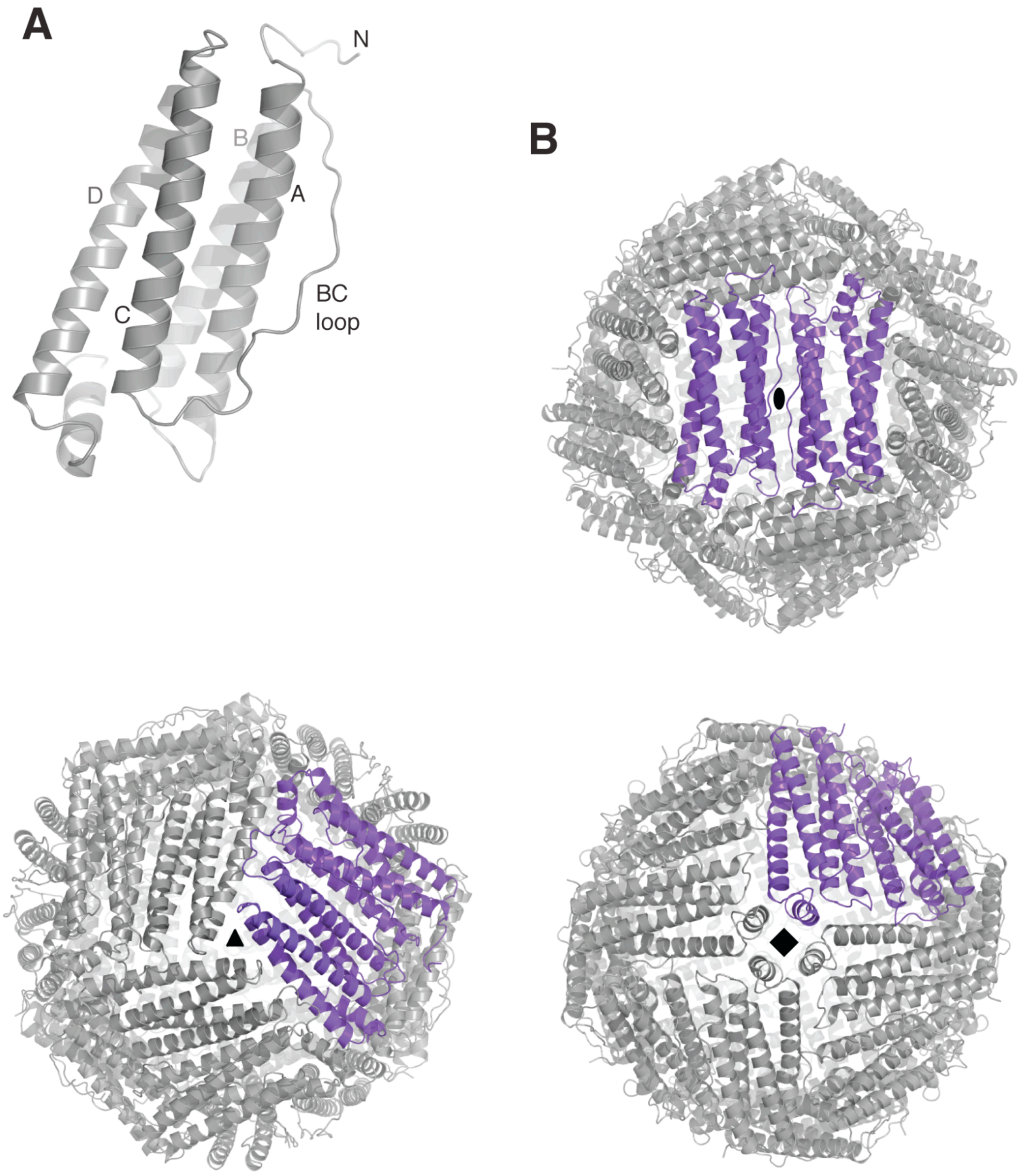

Figure 2.1. The 234-symmetric ferritin cage architecture. A) Monomeric HuHF subunit, highlighting its four constituent helices A-D and the BC loop (adapted from reference 2, PDB ID: 1FHA). B) Putting the C_2, C_3, and C_4 interfaces into the context of the C_2-symmetric dimer highlighted in purple (adapted from reference 2, PDB ID: 1FHA).

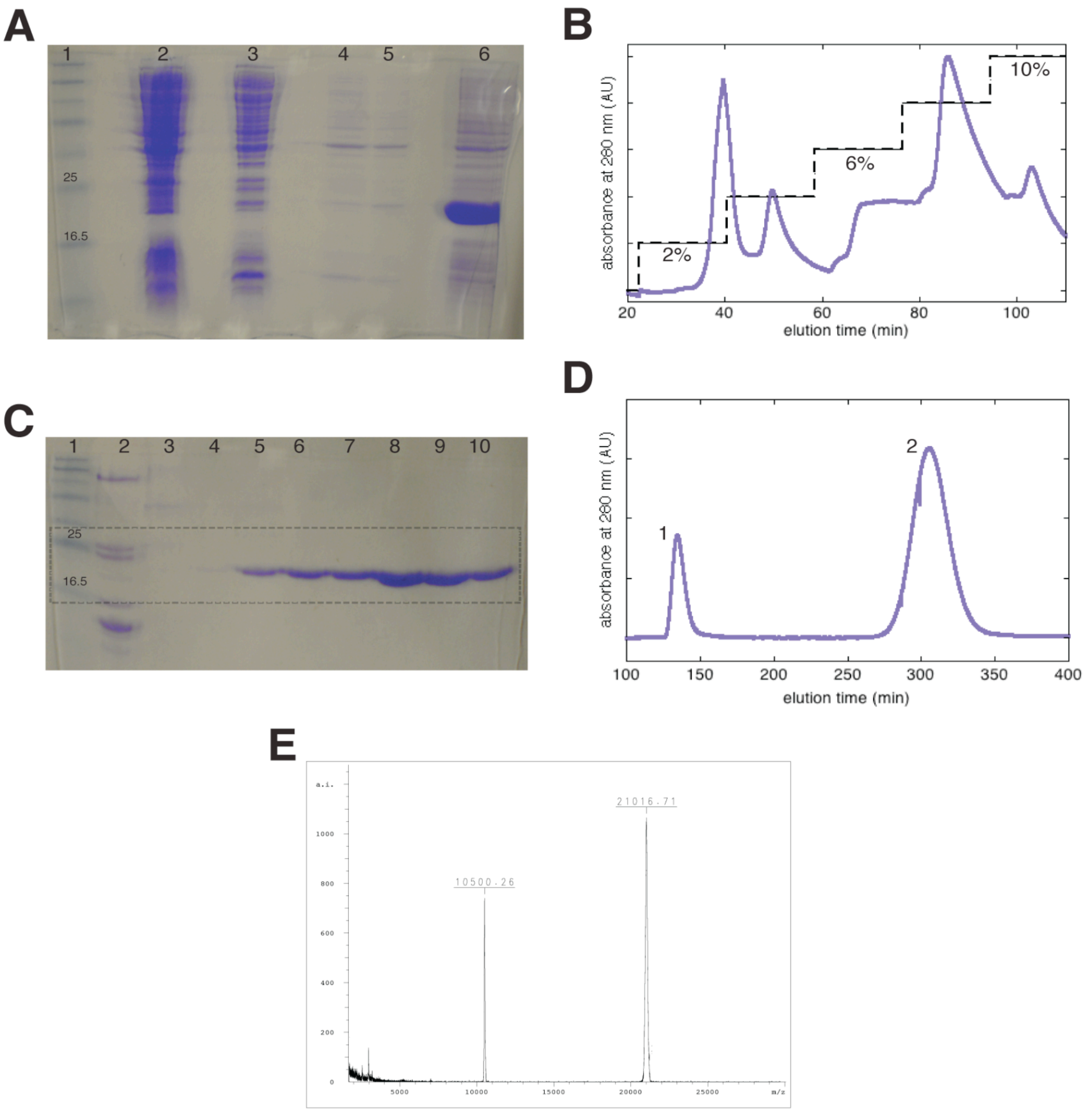

Figure 2.2. HuHF variant purification scheme, illustrating results with MIC1. A) 15% SDS-PAGE gel of the various steps of the process of obtaining MIC1 protein from *E. coli* cells. Lane 1 is a molecular weight marker; lanes 2 and 3 correspond to supernatants following the first and second sonication events, respectively; lanes 4 and 5 represent wash-phase supernatants; lane 6 depicts the typical content of the inclusion-body pellet, solubilized with urea and elevated pH (this includes MIC1 protein at ~21 kDa molecular weight). B) FPLC trace of MIC1 eluting off the Cu-charged HisPrep affinity column, highlighting the stepwise imidazole gradient; protein generally elutes fully by 25 mM imidazole. C) 15% SDS-PAGE gel depicting the elution results from (B). Lane 1 is a molecular weight marker; lanes 2-4 correspond to the 0-4% gradient steps; lanes 5-10 correspond to the clean protein obtained during the steps from 6-10% imidazole-containing buffer. D) Size exclusion chromatogram showing the separation of MIC1 aggregate species (peak 1) from monomeric protein (peak 2) as run in the standard buffer with 10 mM EDTA. E) MALDI-TOF mass spectrometry data for the MIC1 variant confirming protein veracity.

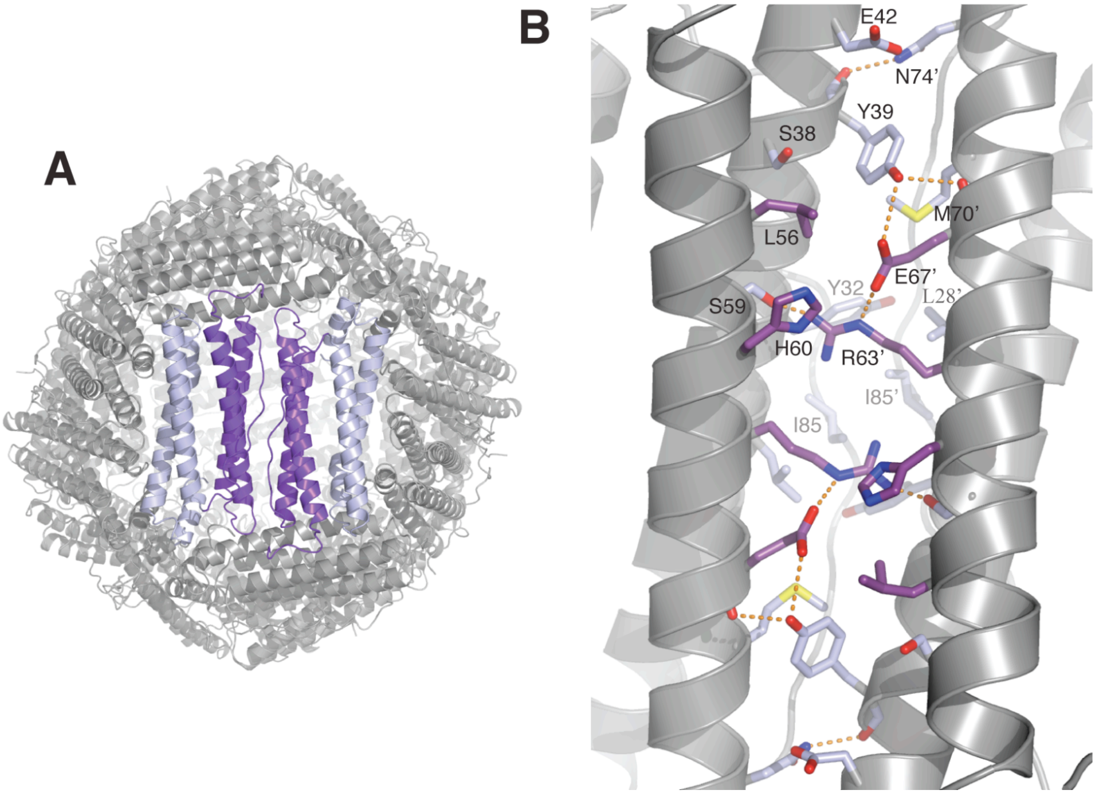

Figure 2.3. The C_2 interface of HuHF. A) The C_2 dimerization interface of ferritin is highlighted in the context of the 24-meric nanocage. The constituents of this protein-protein interface, namely helices A and B, and the BC loop, are colored violet-purple. The C and D helices are shown in silver-blue. B) Zoom-in of the C_2 interface, with key residues named. Shown in violet-purple are residues considered for mutagenesis in the installation of metal-chelating motifs for the first stage of rMeTIR. The remaining interfacial amino acid residues of import are colored silver-blue. Hydrogen bond interactions are indicated with orange dashes.

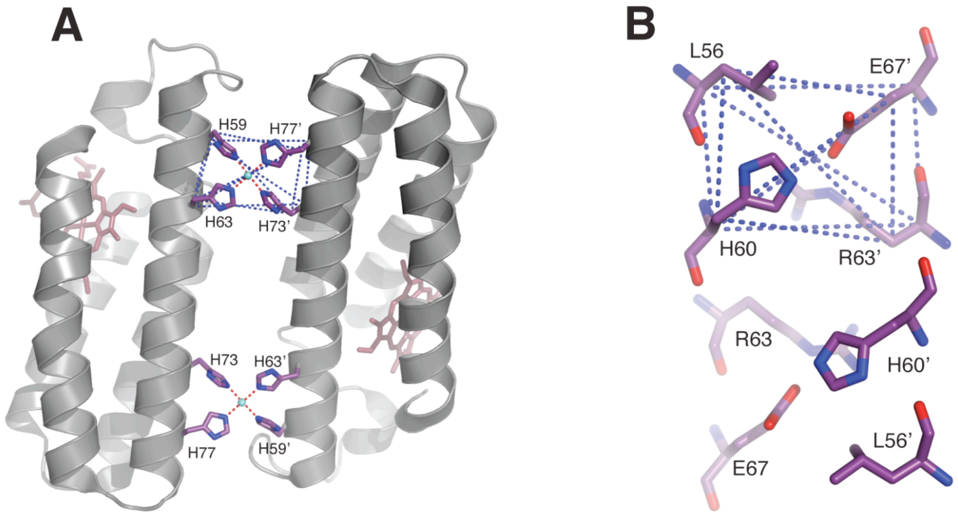

Cu_2:MBPC-1_2

	H59-H63	H59-H77'	H59-H73'	H63-H77'	H63-H73'	H73'-H77'
avg. dist. (Ca- Ca)	6.3 Å	10.6 Å	11.7 Å	12.6 Å	10.8 Å	6.4 Å
avg. dist. (Cb- Cb)	6.5 Å	8.8 Å	10.7 Å	10.9 Å	9.5 Å	6.7 Å

HuHF

	L56-H60	L56-E67'	L56-R63'	H60-E67'	H60-R63'	R63'-E67'
avg. dist. (Ca- Ca)	6.4 Å	9.6 Å	11.7 Å	11.3 Å	9.6 Å	6.3 Å
avg. dist. (Cb- Cb)	6.7 Å	7.7 Å	11.0 Å	9.7 Å	8.5 Å	6.6 Å

Figure 2.4. Identification of interfacial sites for grafting a stable Cu^{II} coordination motif. A) The C_2-symmetric Cu_2:MBPC-1_2 structure directed by Cu^{II} coordination to bis-histidine motifs on the MBPC-1 surface. The resulting stable, Cu-coordination sites are defined by pairwise Cα and Cβ distances (listed in the table below) among the four coordinating histidines. B) Pairwise Cα and Cβ distances among residues 56, 60, 63, and 67 chosen in the HuHF C_2 interface (see Figure 2.3 B for more context) for grafting a stable 4His-Cu coordination site.

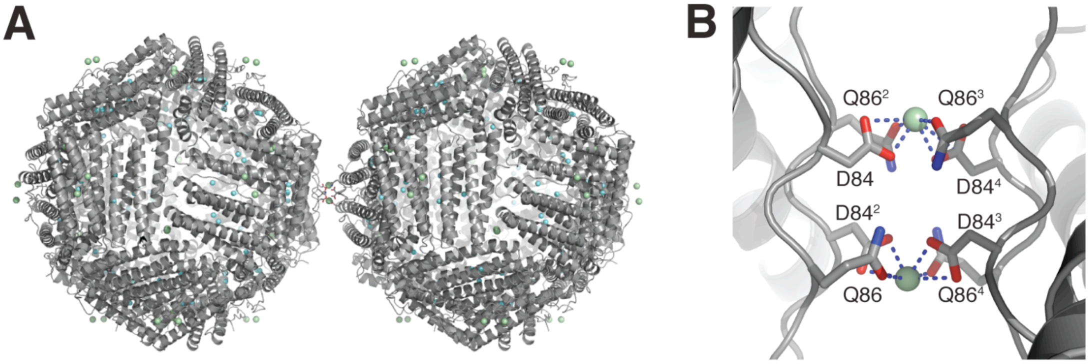

Figure 2.5. Engineered crystal contact with mutation K86Q to facilitate HuHF protein crystallization. A) Depiction of crystal contact established between two ferritin nanocages through the interaction of D84 and Q86 residues from four subunits, located on their respective BC loops, with divalent calcium ions (shown as pale-green spheres). B) Zoomed-in perspective of the engineered crystal contact. Both figures (A) and (B) prepared with the variant 4His-ΔC* crystal structure (*vide infra*) available with PDB ID: 4DYX.

Table 2.1. X-ray data collection and refinement statistics for the protein crystal structure of Cu-4His-ΔC*. * denotes the highest resolution shell.

	Cu-4His-ΔC*
Data Collection Location	SSRL BL 9-2
Unit Cell Dimensions	a = b = c = 179.3 Å
	$\alpha = \beta = \gamma = 90°$
Symmetry Group	F432
Resolution (Å)	103.5-1.85
X-Ray Wavelength (Å)	0.98
Number of Unique Reflections	21660
Redundancy	15.2
Completeness (%)*	100 (100)
$\langle I/\sigma I \rangle$*	9.2 (3.2)
R_{symm} (%)*	6.0 (21.5)
R_{work} (%)*	16.9 (19.8)
R_{free} (%)*	19.7 (23.4)
Number of Atoms	
Protein (including alternative side chain conformations)	1416
Ligands/Ions	7
Water	215
B-Factors ($Å^2$)	
Protein	15.3
Ligands/Ions	29.7
Water	31.8
RMS Deviations	
Bond Lengths (Å)	0.006
Bond Angles (^{o})	0.842
Ramachandran plot (%)	
Residues in favored regions	98.8
Residues in allowed regions	1.2
Residues in generously allowed regions	0.0
Residues in disallowed regions	0.0

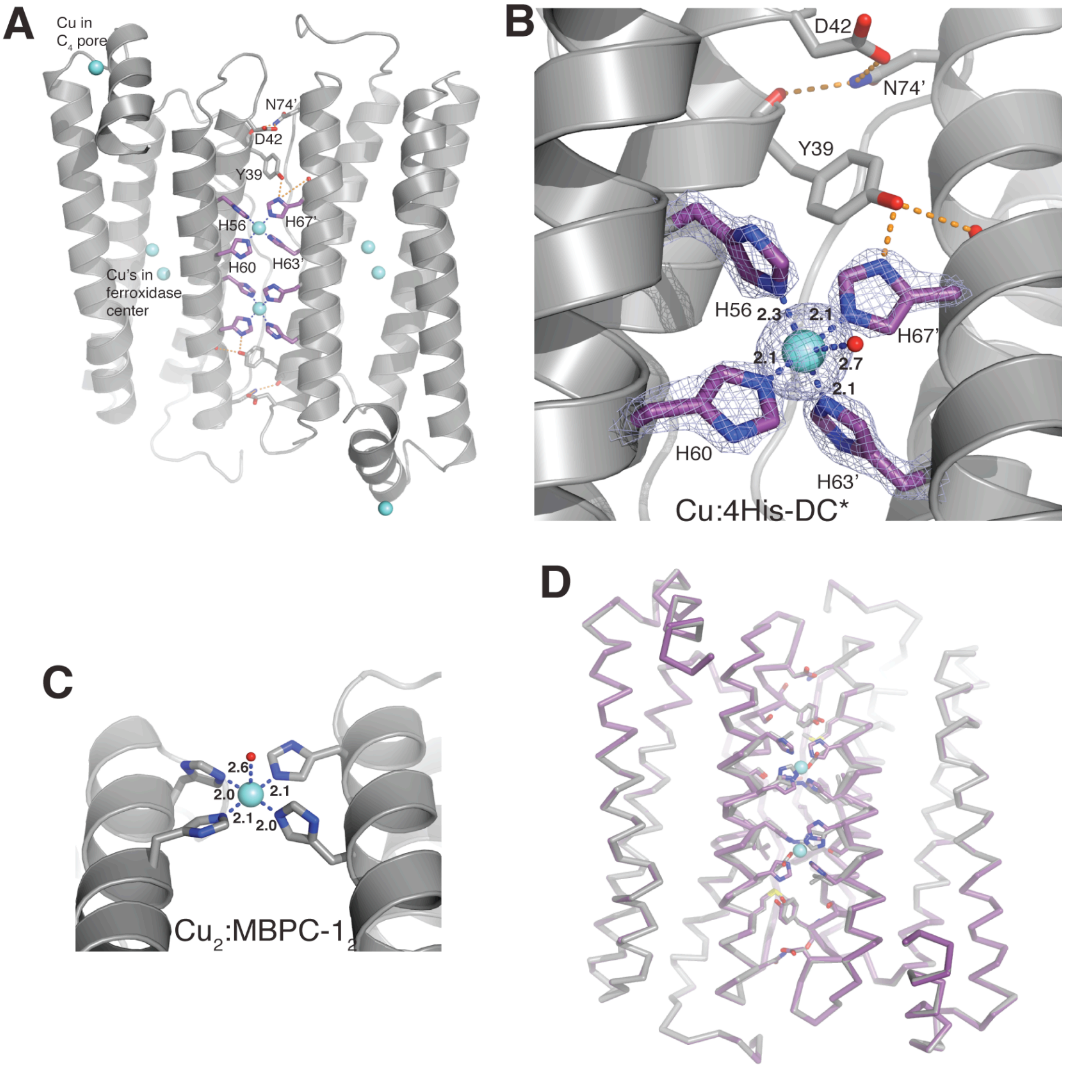

Figure 2.6. Structural features of the Cu-adduct of HuHF variant 4His-ΔC* and its C_2 interface. A) View of the C_2 dimer of the Cu-4His-ΔC* cage down the C_2 symmetry axis. Engineered His clamps are in violet-purple, with copper ions shown as aquamarine spheres and H-bonds as orange dashes. Blue dashes highlight Cu-His coordination. B) Close-up view of one of the two symmetrically related 4His-Cu^{II} coordination motifs in the C_2 interface. The $2F_o$-F_c electron density map associated with the square pyramidal (square plane of 4 His's and an axial water molecule shown as a red sphere) Cu^{II} coordination site is shown as a silver-blue mesh contoured at 2σ, with bond distances in Å as indicated. C) The square pyramidal Cu coordination motif in the Cu_2:MBPC-1_2 structure that served as a model for the construction of 4His-ΔC*. Bond lengths of both model and 4His-ΔC* metal-binding motifs are well matched. D) Backbone superposition of the C_2 dimers of native HuHF (gray, PDB ID: 1FHA) and 4His-ΔC* (violet-purple). The only noticeable different is the slight widening of the C_2 interface of 4His-ΔC* near the metal coordination sites.

Table 2.2. Table of HuHF variants prepared and their assembly characteristics.

	HuHF Variant	**Cellular Form**	**Oligomerization State with EDTA**	**Oligomerization State upon Cu^{II} addition**
I	**ΔC*** (native + K86Q/C90E/ C102A/C130A)	soluble, brown-colored lysate	24mer	24mer
2	**4His-ΔC*** (ΔC* + L56H/R63H/E67H)	soluble, brown-colored lysate	24mer	24mer
3	**4His-ΔC* + Y32D**	inclusion bodies	24mer + some monomer	dimer + 24mer
4	**4His-ΔC* + Y39D**	inclusion bodies	24mer	not determined
5	**4His-ΔC* + Y39E**	soluble, brown-colored lysate	24mer	not determined
6	**4His-ΔC* + Y39K**	soluble, brown-colored lysate	24mer	not determined
7	**4His-ΔC* + P88A**	majority in inclusion bodies	24mer	not determined
8	**4His-ΔC* + L28E/Y39D**	inclusion bodies	24mer + some monomer	24mer (major species) + monomer + dimer
9	**4His-ΔC* + Y39D/N74E**	inclusion bodies	monomer	monomer + dimer + 24mer
10	**4His-ΔC* + Y39E/N74E**	inclusion bodies	monomer	monomer + dimer + 24mer
11	**4His-ΔC* + L28E/Y39D/N74E**	inclusion bodies	monomer	monomer + dimer + mixture of n-mers (no 24mer)
12	**4His-ΔC* + Y39E/N74E/I85D**	inclusion bodies	monomer	monomer + dimer
13	**MIC1** (4His-ΔC* + Y39E/N74E/P88A)	inclusion bodies	monomer	24mer
14	**4His-Loop-ΔC*** (ΔC* + F81H/Q83H/K87H/D91H)	soluble, brown-colored lysate	24mer	not determined
15	**4His-Loop-ΔC* + Y32D**	soluble, brown-colored lysate	24mer	not determined
16	**4His-Loop-ΔC* + Y32D/H128A**	soluble, brown-colored lysate	24mer	not determined

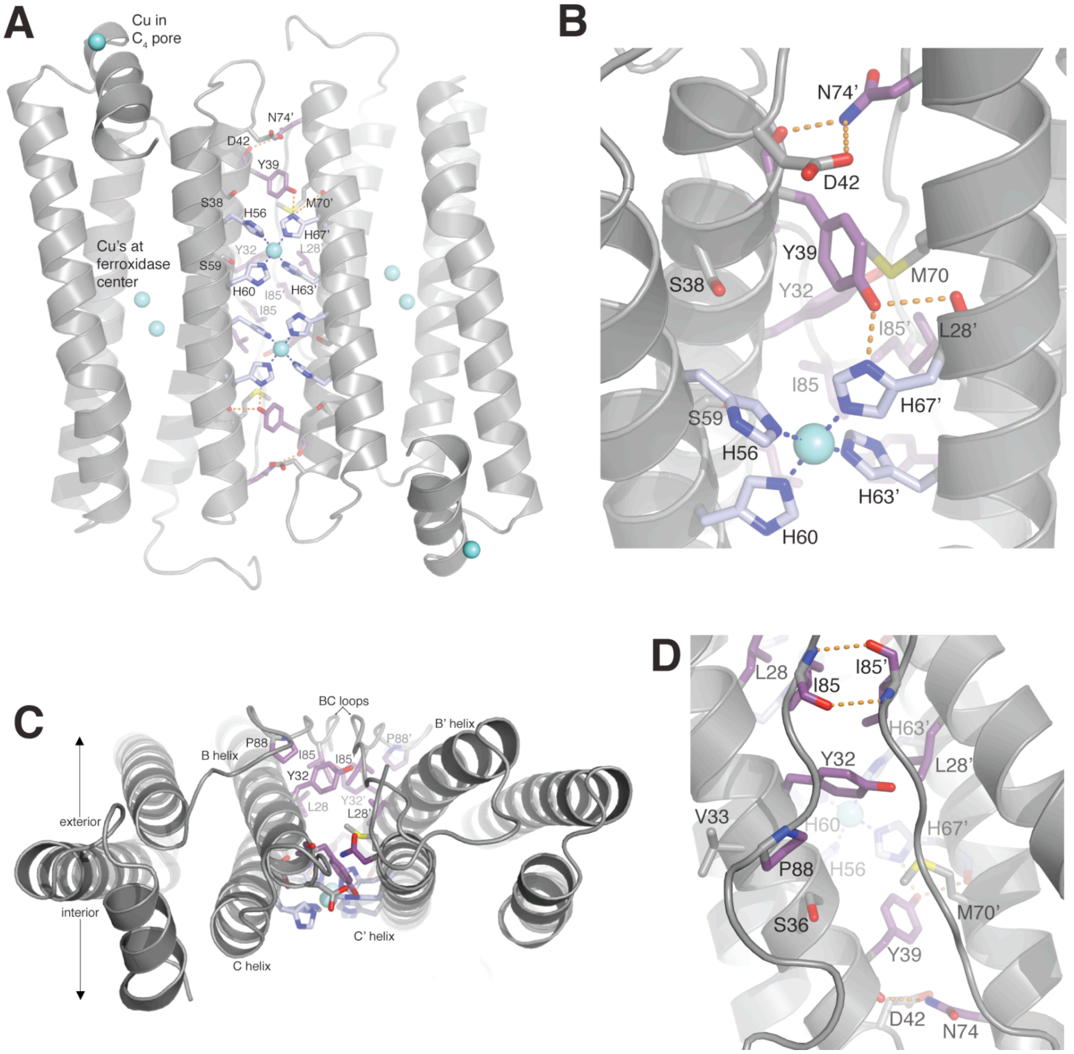

Figure 2.7. Destabilizing the C_2 interface of HuHF variant 4His-ΔC*. A) View down the C_2 dimer interface of the 4His-ΔC* cage, with key interfacial residues named. Cu^{II} (aquamarine spheres) interaction with the 4His (silver-blue) coordination motifs is indicated by blue dashes. Hydrogen bonds are shown as orange dashes. Residues considered for interfacial destabilization mutagenesis are highlighted in violet-purple. B) Close-up view of one half of the C_2 interface, highlighting residues to be screened for perturbation mutagenesis, including Y39 and N74. C) Top-down view of the C_2 interface contextualizing the different regions of the interface where mutagenic screening was planned. These regions include the BC loops (I85, P88), the inner C_2 core (L28, Y32), and the C_2 surface facing the ferritin cage interior (Y39, N74). D) View of P88, which is thought to make van der Waals contacts with Y32, V33, and S36, thereby conferring the proper organization of the BC loop.

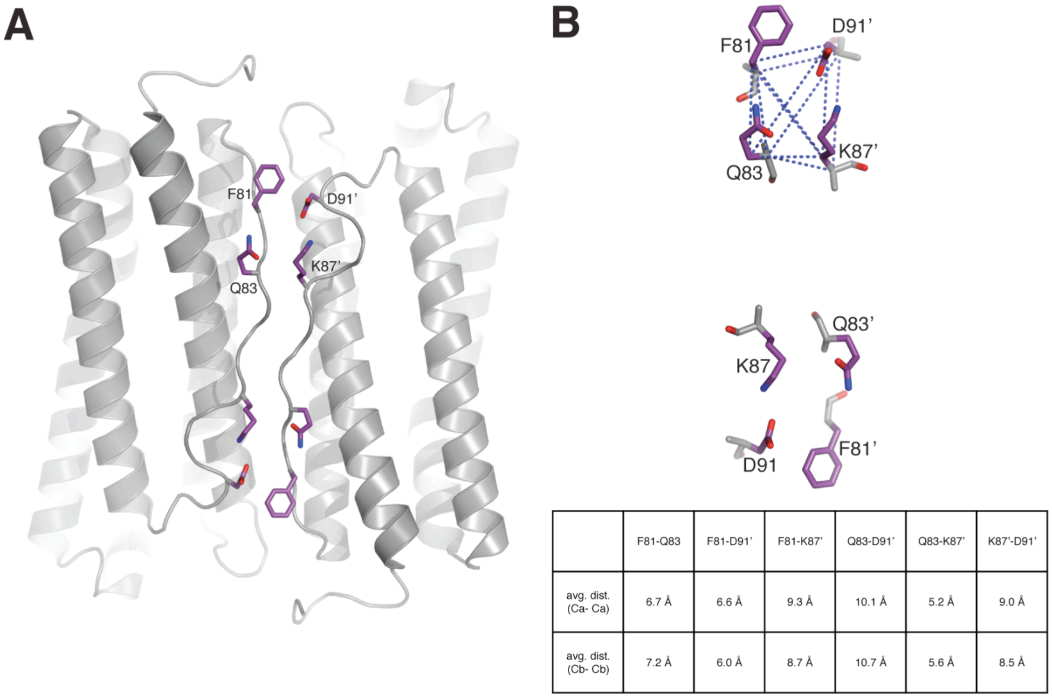

	F81-Q83	F81-D91'	F81-K87'	Q83-D91'	Q83-K87'	K87'-D91'
avg. dist. (Ca- Ca)	6.7 Å	6.6 Å	9.3 Å	10.1 Å	5.2 Å	9.0 Å
avg. dist. (Cb- Cb)	7.2 Å	6.0 Å	8.7 Å	10.7 Å	5.6 Å	8.5 Å

Figure 2.8. Alternative site of Cu^{II} coordination motif installation proposed for the ΔC* HuHF template. A) View down the C_2 dimerization interface of native HuHF (with K86Q, figure made with PDB ID: 1FHA) showcasing the position of a potential set of two 4His metal-binding clamps. The amino acid residues to be mutated are colored in violet-purple. B) Pairwise Cα and Cβ distances among residues 81, 83, 87, and 91 chosen on the BC loop of the C_2 interface as an alternative site for grafting a 4His-Cu coordination site. Distances are, on average, much shorter than those of the model Cu-binding site of cytochrome *cb*$_{562}$ variant MBPC-1 (see Figure 2.4). However, the BC loop is presumed to be flexible enough to accommodate Cu^{II}-4His coordination.

References

1. Liu, X.F. and E.C. Theil, *Ferritins: Dynamic management of biological iron and oxygen chemistry.* Accounts of Chemical Research, 2005. **38**(3): p. 167-175.

2. Lawson, D.M., et al., *Solving the Structure of Human H-Ferritin by Genetically Engineering Intermolecular Crystal Contacts.* Nature, 1991. **349**(6309): p. 541-544.

3. Listowsk.I, et al., *Denaturation of Horse Spleen Ferritin in Aqueous Guanidinium Chloride Solutions.* Biochemistry, 1972. **11**(11): p. 2176-2182.

4. Crichton, R.R. and C.F.A. Bryce, *Subunit Interactions in Horse Spleen Apoferritin - Dissociation by Extremes of Ph.* Biochem. J., 1973. **133**(2): p. 289-299.

5. Stefanini, S., et al., *Thermal stability of horse spleen apoferritin and human recombinant H apoferritin.* Archives of Biochemistry and Biophysics, 1996. **325**(1): p. 58-64.

6. Treffry, A., et al., *Defining the Roles of the Threefold Channels in Iron Uptake, Iron Oxidation and Iron-Core Formation in Ferritin - a Study Aided by Site-Directed Mutagenesis.* Biochemical Journal, 1993. **296**: p. 721-728.

7. Bou-Abdallah, F., et al., *Defining metal ion inhibitor interactions with recombinant human H- and L-chain ferritins and site-directed variants: an isothermal titration calorimetry study.* Journal of Biological Inorganic Chemistry, 2003. **8**(4): p. 489-497.

8. Butts, C.A., et al., *Directing Noble Metal Ion Chemistry within a Designed Ferritin Protein.* Biochemistry, 2008. **47**(48): p. 12729-12739.

9. Ueno, T., et al., *Process of Accumulation of Metal Ions on the Interior Surface of apo-Ferritin: Crystal Structures of a Series of apo-Ferritins Containing Variable Quantities of Pd(II) Ions.* Journal of the American Chemical Society, 2009. **131**(14): p. 5094-5100.

10. d'Estaintot, B.L., et al., *Crystal structure and biochemical properties of the human mitochondrial ferritin and its mutant Ser144Ala.* Journal of Molecular Biology, 2004. **340**(2): p. 277-293.

11. Barnes, C.M., E.C. Theil, and K.N. Raymond, *Iron uptake in ferritin is blocked by binding of a slow dissociating.* Proceedings of the National Academy of Sciences of the United States of America, 2002. **99**(8): p. 5195-5200.

12. Webb, B., et al., *Molecular Entrapment of Small Molecules within the Interior of Horse Spleen Ferritin.* Archives of Biochemistry and Biophysics, 1994. **309**(1): p. 178-183.

13. Xing, R.M., et al., *Characterization and cellular uptake of platinum anticancer drugs encapsulated in apoferritin.* Journal of Inorganic Biochemistry, 2009. **103**(7): p. 1039-1044.

14. Salgado, E.N., R.J. Radford, and F.A. Tezcan, *Metal-Directed Protein Self-Assembly.* Accounts of Chemical Research, 2010. **43**(5): p. 661-672.

15. Stefanini, S., P. Vecchini, and E. Chiancone, *On the Mechanism of Horse Spleen Apoferritin Assembly - a Sedimentation-Velocity and Circular-Dichroism Study.* Biochemistry, 1987. **26**(7): p. 1831-1837.

16. Gerl, M., et al., *Self-Assembly of Apoferritin from Horse Spleen after Reversible Chemical Modification with 2,3-Dimethylmaleic Anhydride.* Biochemistry, 1988. **27**(11): p. 4089-4096.

17. Santambrogio, P., et al., *Effects of modifications near the 2-, 3- and 4-fold symmetry axes an human ferritin renaturation.* Biochemical Journal, 1997. **322**: p. 461-468.

18. Winn, M.D., et al., *Overview of the CCP4 suite and current developments.* Acta Crystallographica Section D-Biological Crystallography, 2011. **67**: p. 235-242.

19. Vagin, A. and A. Teplyakov, *MOLREP: an automated program for molecular replacement.* Journal of Applied Crystallography, 1997. **30**: p. 1022-1025.

20. Murshudov, G.N., A.A. Vagin, and E.J. Dodson, *Refinement of macromolecular structures by the maximum-likelihood method.* Acta Crystallographica Section D-Biological Crystallography, 1997. **53**: p. 240-255.

21. Emsley, P. and K. Cowtan, *Coot: model-building tools for molecular graphics.* Acta Crystallographica Section D-Biological Crystallography, 2004. **60**: p. 2126-2132.

22. DeLano, W.L., *The PYMOL Molecular Graphics System.* 2003.

23. Schuck, P., *A model for sedimentation in inhomogeneous media. I. Dynamic density gradients from sedimenting co-solutes.* Biophysical Chemistry, 2004. **108**(1-3): p. 187-200.

24. de la Torre, J.G., M.L. Huertas, and B. Carrasco, *Calculation of hydrodynamic properties of globular proteins from their atomic-level structure.* Biophysical Journal, 2000. **78**(2): p. 719-730.

25. Salgado, E.N., et al., *Control of Protein Oligomerization Symmetry by Metal Coordination: C(2) and C(3) Symmetrical Assemblies through Cu(II) and Ni(II) Coordination.* Inorganic Chemistry, 2009. **48**(7): p. 2726-2728.

26. Zhang, Y. and B.P. Orner, *Self-Assembly in the Ferritin Nano-Cage Protein Superfamily.* International Journal of Molecular Sciences, 2011. **12**(8): p. 5406-5421.

27. Waldron, K.J. and N.J. Robinson, *How do bacterial cells ensure that metalloproteins get the correct metal?* Nature Reviews Microbiology, 2009. **7**(1): p. 25-35.

28. Hempstead, P.D., et al., *Comparison of the three-dimensional structures of recombinant human H and horse L ferritins at high resolution.* Journal of Molecular Biology, 1997. **268**(2): p. 424-448.

Chapter 3.

Copper-Templated Ferritin Cage Assembly:

Cu^{II} is a True Template for MIC1 Oligomerization

Introduction

Application of the protein-protein interface re-design strategy reverse metal-templated interface redesign to the C_2 dimerization surface of cage-like protein HuHF afforded metal-responsive protein building blocks that, in the presence of Cu^{II}, self-assembled from monomeric species to 24-meric nanocages. The chemically-inducible cage-forming HuHF variant was termed MIC1, for Metal-Induced Cage Variant 1, and it contained two sets of mutagenic modifications at the C_2 interface on the ΔC*[1] protein scaffold. The first group of mutations, L56H, R63H, and E67H, along with native residue H60, imparted metal-chelation capability at the dimer interface with two 4His binding motifs. The second set of mutations, Y39E, N74E, and P88A, were included to destabilize the C_2 PPI surface such that metal binding becomes requisite for driving MIC1 to higher oligomerization states than simple monomers.

Initial solution-state screening with sedimentation velocity experiments identified MIC1 monomers as responsive to Cu^{II} in their capacity to form ferritin cages. The screens reflected “quick” reactions of the protein with Cu^{II} ions, and by no means showcased complete conversion to the 24-meric species. A more thorough exploration of the metal-binding switch phenomenon was required. In particular, we sought a higher-yielding self-assembly protocol. With such a scheme developed, we could begin to explore whether cage conversion was unique to Cu^{II} and other metal ions favoring square planar binding arrangements, as hypothesized based on previous results with the cytochrome *cb₅₆₂* system[2-4] and the crystal structure of 4His-ΔC*. Also, the question of reversibility with regards to cage formation arose; we expected that upon the removal of the metal “glue” responsible for 24mer organization from monomers, the nanocage would disassemble. Taken together, we hoped to gain insight into the assembly process of HuHF nanocages through the advent of controlling their creation from building blocks rendered externally responsive, with the ultimate goal of applying our understanding of the MIC1 system to gains in practical applications.

Materials and Methods

Protein expression, purification and characterization. Proteins were expressed, as above, in *E. coli* BL21 (DE3) cells, with expression initiated by IPTG induction. As previously outlined, following cell lysis, proteins were obtained from inclusion body pellets. After solubilization with urea and high-pH buffers, variants were purified via FPLC using a combination of metal-affinity and size-exclusion chromatographies. Protein purity and veracity were determined through SDS-PAGE gel electrophoresis and MALDI-TOF mass spectrometry, respectively.

Metal-Mediated MIC1 self-assembly. Purified, monomeric MIC1 was concentrated to 100 μM in standard buffer containing 10 mM EDTA; EDTA ensured prevention of oligomerization of the MIC1 protein. 7-mL portions of the MIC1 stock were dialyzed against 2 x 5 L of solutions containing 100 μM (equimolar) $CuCl_2$, $NiCl_2$, or $ZnCl_2$ prepared in standard buffer over 40 hours at 4 °C. Following dialysis, the metal-reacted protein samples were centrifuged for 10 minutes at a speed of 10,000 rpm at 4 °C to remove precipitated protein. In each case, approximately 40-50% of the total protein formed insoluble aggregates as quantified by the Bradford assay. Prior to further characterization, metal-mediated MIC1 assemblies in soluble fractions were separated by size exclusion chromatography on an XK26/100 column packed with Ultrogel AcA 34 resin as described before, running on the standard buffer.

Analytical ultracentrifugation. SV measurements were performed as described above using a Beckman-Optima XL-I Analytical Ultracentrifuge equipped with an An-60 Ti rotor. Protein samples were prepared in standard buffer, which included 10 mM EDTA when metal-free conditions were required. Typically, the experimental protein concentration was set to 50 μM, and was determined by Bradford assay. The wavelength used for sample detection was 280 nm, and the instrument was run at 41,000 rpm with the temperature maintained at 25 °C for the duration of the run.

SV data were processed using the program SEDFIT[5] and fit to a continuous c(s) model. Key buffer properties, including density and viscosity, were calculated for 25 °C temperature with SEDNTERP (http://www.jphilo.mailway.com). The partial specific volume of MIC1 and the theoretical sedimentation coefficients of various MIC1 oligomers were calculated with HYDROPRO.[6] Data were processed with SEDFIT in the manner outlined above. Table 3.1 summarizes all parameters utilized in the analysis of the SV measurements.

Transmission electron microscopy (TEM) imaging. Solution-state characterization of MIC1 oligomers was corroborated by TEM imaging experiments. Copper-coated carbon grids (Electron Microscopy Services) were glow discharged for ~1 minute in an Emitech K350 evaporation unit. Immediately following 5 μM protein samples in standard buffer were deposited onto the grids in 3 μL aliquots; in the case of metal-free specimens, 10 mM EDTA was included in the protein buffer solution. After 1 minute of incubation, the grids were washed with double-distilled water, and the excess solution was wicked away. The samples were then stained twice with 3 μL of a 1% uranyl acetate solution. After drying, the grids were imaged on an FEI Sphera transmission electron microscope equipped with an LaB_6 electron gun operating at 200 keV. Objective lens underfocus settings ranging from 400-800 nm on a Gatan $2K^2$ CCD were employed. Analysis of the TEM micrographs was carried out with Image J (Freeware, National Institutes of Health, USA).

Iron oxidation/storage assay. The capacity of the MIC1 variant to perform native HuHF chemistry, the oxidation and storage of iron within the 24mer cavity, was probed using the method outlined by Liu and Theil.[7] MIC1 monomeric or Cu^{II}-driven 24-meric protein was exchanged into 0.2 M MOPS buffered at pH 7.0, with a final concentration of 90 μM protein (in terms of monomeric units). A stock solution of 0.1 M $FeSO_4$ was prepared (from $FeSO_4 \cdot 7H_20$ salt) in 1 mM HCl. Additions from this stock were given to 500 μL volumes of MIC1 proteins to achieve a final ratio of 24 Fe^{II} ions per each MIC1 subunit. Immediately after mixing, the protein solutions became turbid, and precipitation was accompanied by a color change from clear and colorless to murky yellow-red. The samples were centrifuged for 10 minutes at 12,000 rpm, and the supernatants were characterized by TEM in the case of the Fe-treated MIC1 cages. When MIC1 monomers alone were reacted with the FeSO4 solution, all protein became insoluble. Similarly, MIC1 monomeric protein that was reacted with $FeSO_4$ and $CuCl_2$ simultaneously also precipitated from solution.

Metal content analysis. The technique of inductively coupled plasma-optical emission spectroscopy (ICP-OES) was employed to quantify the metal content of MIC1 protein samples. Standard solutions used to generate a calibration curve were prepared from 1000-ppm certified ICP-OES metal stock solutions (Ricca). The calibration concentrations ranged from 0.05 to 10 ppm metal, and 15 data points altogether were used to construct each calibration curve. The experimental blank was high-quality Milli-Q water (with resistance higher than 18 MΩ/cm) treated with Chelex resin (Bio-Rad) to ensure the absence of metal ions. Protein samples were prepared in 0.1 M NaP_i buffered at pH 7.4 with or without 1 mM EDTA. To facilitate MIC1 protein solubilization, the protein samples were mixed, with the aid of a vortex apparatus, with equivalent volumes of 8 M guanidine hydrochloride (GuHCl) dissolved in the same buffer, 0.1 M NaP_i maintained at pH 7.4. All samples for ICP-OES measurements contained 3% reagent grade HNO_3 (Fluka).

Data were collected on a Perkin-Elmer Optima 3000 DV ICP-OES spectrometer housed in the Analytical Facility of the Scripps Institution of Oceanography. Wavelengths used for the detection of Cu included: 221.459 nm, 222.778 nm, 224.700 nm, 324.752 nm, and 327.393 nm. Values reported for metal content reflect averages of the data obtained at these wavelengths.

Far-UV circular dichroism (CD) characterization. MIC1 protein in both monomeric and Cu^{II}-driven nanocage oligomerization states was exchanged from the standard buffer into Chelex resin-treated high-quality Milli-Q water. The protein samples were diluted to a final concentration of 2 μM. The MIC1 monomer samples were left metal-free, or treated with equimolar concentrations of $CuCl_2$, $NiCl_2$, or $ZnCl_2$. CD measurements were taken with the samples in a 1-cm pathlength quartz cuvette using an Aviv 215 circular dichroism spectrometer. The temperature for each data set was held at 25 °C, with samples being equilibrated at this temperature for 1 minute prior to measurement initiation. Ellipticity was monitored over a wavelength range of 260-190 nm, with sampling occurring every 1 nm with a 1.5 second integration period. Data presented reflect the average of 5 scans performed per sample, with a water blank taken as reference.

Unfolding titrations. Chemical and thermal unfolding titrations were performed on the MIC1 protein in various oligomerization states to explore their respective stabilities. All unfolding experiment samples contained 2.5 μM protein that had been exhaustively dialyzed at 4 °C into a buffer containing 0.1 M NaP_i maintained at pH 7.4. In the case of metal-free experiments, 1 mM EDTA was included in the protein buffer solution. For chemical denaturation titrations, samples included GuHCl ranging in concentration from 0 to 8 M. After mixing, the sample solutions were equilibrated for 18 hours at 4 °C prior to taking measurements.[1] Samples were then placed in a 1-cm pathlength quartz cuvette for analysis.

CD measurements were performed on an Aviv 215 circular dichroism spectrometer. For chemical denaturation titrations, ellipticity was monitored at 222 nm following 1 minute of equilibration at 25 °C. Thermal denaturation titrations were performed over a temperature range of 4-95 °C at 2-°C steps. Again, ellipticity was monitored at 222 nm, with sampling occurring after samples were allowed to equilibrate for 45-60 seconds. All data were collected in triplicate, and fit according to published protocols (see the relevant data analysis section in the Appendix).

X-ray crystallography. Protein crystals of Cu-bound MIC1 and apo-MIC1 were obtained by the sitting-drop vapor diffusion method. The sitting drops yielding diffraction-quality crystals consisted of 2 μL of protein solution and 2 μL of precipitant solution. The wells contained 500 μL of precipitant solution. In the case of Cu-containing MIC1 crystals, the protein solution was made of 642 μM of MIC1 in standard buffer. The precipitant consisted of 50 mM Tris buffered at pH 8.0, with 5 mM $CaCl_2$ and 700 μM $CuCl_2$. The precipitant also contained 8% (by weight) PEG 1900 MME. Apo-MIC1 crystals were grown with a 666 μM protein stock that had been pre-reacted with equimolar $CuCl_2$ to induce cage formation; the protein stock was prepared in standard buffer. The precipitant solution was 4% (by weight) PEG 400, and contained 50 mM Tris buffered at pH 8.0, 10 mM CaCl2, and 20 mM EDTA. The EDTA was present to prepare apo-MIC1 cages *in situ* from the Cu-assembled protein nanovessels. The crystals grew at room temperature within a one-month period. For cryoprotection, ~1 μL of glycerol was added directly to the 4-μL well solution containing crystals, and the crystals were pulled through this glycerol layer and immediately frozen in liquid N_2.

X-ray diffraction data were collected at 100 K at Beamline 9-2 of the SSRL facility using 0.98-Å radiation. Data were also collected at the Cu K-edge (1.3 Å) to identify Cu centers through anomalous scattering. Diffraction data were processed using MOSFLM and SCALA.[8] Structures were solved with molecular replacement by MOLREP[9] using the structure of the K86Q[10] mutant (PDB ID:2CEI) as a model. Rigid-body, positional and thermal refinement was carried out using REFMAC,[11] along with iterative manual model building with COOT.[12] Atomic coordinates and structure factors have been deposited into the Protein Data Bank with identification numbers 4DYY and 4DYZ corresponding to the structures of Cu-MIC1 and apo-MIC1, respectively. All structural figures were produced using PYMOL.[13]

Results and Discussion

The Cu^{II}-induced self-assembly of MIC1 monomers into ferritin nanocages. In its as-isolated form in the presence of EDTA, and hence the absence of free metal ions, MIC1 is completely monomeric. The MIC1 monomers exhibited a peak sedimentation coefficient of 2.2 S (Figure 3.1 A, red trace). Upon exchange into an equimolar Cu^{II} solution (typically both metal and protein species were at 100 μM concentrations) at physiologic pH, MIC1 is converted into a 24-meric cage with a sedimentation coefficient of ~20 S. (As will become apparent, the observed sedimentation coefficient of the nanocages is sensitive to the quantity of Cu^{II} ions bound.) Both size exclusion chromatography and sedimentation velocity experiments were used to characterize the solution-state of the MIC1 protein oligomers; the latter technique was used as a calibration guide for the former.

"Quick" reactions of MIC1 monomers with Cu^{II}, in which the protein and metal were rapidly mixed and assayed for oligomeric state, resulted in incomplete monomer-to-cage turnover. It was found that through slow mixing of monomeric MIC1 protein and Cu by dialysis over a two-day period at 4 °C essentially complete cage conversion was achieved. That is, of the soluble proteins remaining, neither monomeric nor dimeric MIC1 species were detected, only 24-meric MIC1 (Figure 3.1 A, blue trace).

The progression from MIC1 monomers to ferritin nanocages upon Cu^{II}-binding is clearly visible in TEM images of MIC1 protein taken before and after metal addition (Figure 3.1 B). The as-isolated MIC1 monomers in standard buffer with 10 mM EDTA appear devoid of noticeable features in captured TEM images. However, Cu-treated MIC1 samples are imaged as typical ferritin nanocages, with normal, ~12 nm diameters. It is important to note that, despite the fact that TEM is a "dry" technique, MIC1 monomers still appeared featureless with no conversion upon sample drying to cages; it has been observed in the literature that partially-destabilized ferritin variants can form nanocages when subjected to TEM imaging conditions.[14] Also confirmed by TEM is the capacity of the Cu-assembled MIC1 cages to perform native enzymatic function, the oxidation and storage of iron within the ferritin cavity (Figure 3.2).

The intended templating strategy for metal-induced MIC1 cage formation was indeed specific for Cu^{II} over other divalent late-first-row transition metal ions including Ni^{II} and Zn^{II} (Figure 3.3). The 4His binding motif installed at the C_2 interface was expected to best accommodate square planar Cu^{II} under turnover conditions. At the protein and metal concentrations tested (≤100 μM), Zn^{II} binding produced a noticeably lower yield of 24mer formation, whereas Ni^{II} binding produced no species greater in oligomerization state than dimers. The Cu^{II}-selectivity of MIC1 cage assembly is attributed to the alternative stereochemical preferences of Ni^{II} (octahedral) and Zn^{II} (tetrahedral) that do not enforce the correct alignment of the C_2 interface upon metal binding and are therefore not conducive to monomer organization into 24-meric species.

MIC1 cages persist despite removal of Cu. Interestingly, the Cu-induced MIC1 cage does not disassemble upon the removal of bound Cu^{II} ions by chelation with EDTA. This phenomenon was determined by size exclusion chromatography and confirmed with sedimentation velocity and TEM measurements (Figure 3.1), all of which indicated that metal chelation left MIC1 cages intact. Additional confirmation of the complete removal of Cu from the C_2 interface coordination sites came from X-ray crystallography results (*vide infra*). These findings were corroborated by ICP-OES measurements, which showed that the Cu content of isolated MIC1 cages decreased from 1.05±0.15 Cu/monomer to 0.24±0.05 Cu/monomer upon EDTA treatment. This remaining fraction of Cu is associated with other metal binding sites on the protein cage such as the ferroxidase site that displays ~50% Cu occupancy in the crystals.

In the MIC1 system, Cu^{II} behaves as a true template for cage formation. Cu^{II} promotes the correct structural alignment of the MIC1 monomers across the engineered C_2 interface, and once all of the “sticky surfaces” of MIC1 associate to form the thermodynamically and kinetically stable cage, it can be removed without disrupting the nanocage architecture. Substitution of one or all of the coordinating His residues (with the mutation H60A or coordination motif reversal mutations H56L/H63R/H67E) manifested in the partial or complete loss of capacity for Cu^{II}-triggered MIC1 monomer-to-cage transition (Figure 3.4). These observations reinforce the importance of correct alignment along the C_2 dimerization interface in the cage formation process.

Protein crystal structures of the Cu-mediated MIC1 cage and the apo-MIC1 cage (obtained following treatment of the former with EDTA) were determined at resolutions of 1.9 Å and 2.3 Å, respectively (see Table 3.2 for refinement statistics and Figures 3.5 and 3.6). The C_2 dimers of both MIC1 structures superpose well onto the 4His-ΔC* dimer, with respective rmsd values of 0.15 Å and 0.28 Å over all C_α positions (Figures 3.5 C and 3.6 C). In the C_2 interface of the Cu^{II}-induced MIC1 structure, the newly incorporated E39 residue now anchors a well-ordered, water-mediated H-bonding network, which involves residue S38 and H67’ involved in Cu-coordination (Figure 3.5 B). Mutation E39 also is within H-bonding distance to the engineered E74’ residue, which raises the possibility that E39 may be protonated. Both mutated E74’ and native D42 side chains assume multiple conformations in the crystal structure, each pointing away from the other. This observation is consistent with repulsive electrostatic interactions between the two residues that were originally planned with the N74E mutation to destabilize the C_2 interface during the second phase of rMeTIR HuHF re-design.

The crux for chemically-initiated self-assembly of MIC1 monomers into nanocage structures is the engineered 4His binding motif that favors square planar Cu^{II} binding at the C_2 interface, thereby allowing for proper protein building block alignment and cage assembly. Indeed, the square planar Cu^{II} geometry observed in the Cu-MIC1 structure is unaltered from that seen in the 4His-ΔC* protein crystal structure. Removal of Cu^{II} ions to yield apo-MIC1 cages renders all coordinating His residues disordered, with the exception of H56 (Figure 3.6 B). The water-mediated H-bonding network centered on E39 also becomes eliminated in the apo-MIC1 structure. The observations that a) the native C_2 interface geometry is retained in the apo-MIC1 cage despite the removal of many native H-bonding interactions, and b) MIC1 monomers do not self-assemble in the absence of Cu coordination, point to the key role of the polar interactions that have been removed in MIC1 primarily providing geometric specificity, rather than thermodynamic stability, in native ferritin cage assembly.

Thermodynamics of folding and self-assembly of MIC1. The canonical understanding of the mechanism of ferritin cage disassembly and reassembly has been hampered by the unavailability of a means of obtaining well-characterized monomeric protein subunits under moderate conditions. Previously, an acidification procedure requiring ferritins to be subjected to pH 2 for disassembly, followed by neutralization at pH 7 for cage organization, had been implemented to probe these mechanisms. Such pH changes bring about the simultaneous unfolding/folding of the ferritin monomers, and therefore it has not been possible to fully uncouple and thus dissect the self-assembly and folding processes of this system.

The self-assembly mechanism of ferritin monomers into dimers and subsequently into higher-order oligomers was postulated to be preceded by the folding of the monomers into their native four-helix bundle structures: $24\ M_1 \rightarrow 24\ \mathrm{M}_1 \rightarrow 8\ \mathrm{M}_2 + 8\ \mathrm{M}_1 \rightarrow 8\ \mathrm{M}_3 \rightarrow 4\ \mathrm{M}_6 \rightarrow 2\ \mathrm{M}_{12} \rightarrow 1\ \mathrm{M}_{24}$.[15, 16] Here, M_1 and M_1 refer to the unfolded and folded monomers, respectively, and the subscripts refer to the number of subunits in an intermediate. The given mechanism is by no means a consensus mechanism,[17] but most agree in the literature that the starting point for ferritin cage assembly beings with an unfolded monomer transitioning into a folded state and thereby triggering dimerization and the following formation of greater oligomeric species. However, one can envision, under physiological conditions, an alternative self-assembly pathway, which involves the dimerization-coupled folding of the monomers as a first step.

The MIC1 protein is monomeric in nature in the absence of metal ions at physiological pH, and therefore allows for the probing of the initial steps of HuHF self-assembly. Far-UV CD measurements show that the MIC1 protein, in its monomeric state, is highly α-helical. MIC1 monomers exhibit well-defined minima at 208 and 222 nm, as well as a maximum at 195 nm, hallmark features of α-helicity (Figure 3.7 A). The molar ellipticity of MIC1 changes negligibly as the protein transitions from the monomeric to the 24-meric Cu^{II}-induced cage-like state, reinforcing the fact that the isolated MIC1 monomer is indeed a folded four-helix bundle. Observed molar ellipticities coincide well with those found for ferritins.[18]

At dilute protein concentrations that do not promote self-assembly, the secondary structure of MIC1 remains essentially unaltered in the presence of late-first-row transition metal ions as measured by far-UV CD. Monomers mixed with equimolar Cu^{II}, Ni^{II}, or Zn^{II} exhibited CD traces that superimpose nearly perfectly with that obtained for the metal-free MIC1 monomers (Figure 3.7 A). These findings suggest that the folding of the ferritin monomer is uncoupled from its dimerization/self-assembly at physiologically relevant pH. Also, the role of Cu^{II} binding in cage formation does not involve the folding/pre-organization of the MIC1 monomer, as metal binding appears to impart no additional α-helicity to the protein building blocks. This further corroborates the function of Cu^{II} as a specific structural template for the formation of the C_2 dimer, since no change in CD signature was detected amongst various divalent metal cations.

The folding free energy, or $\Delta G_{folding}$, of MIC1 was determined through chemical and thermal denaturation studies. In these experiments, loss of α-helicity was monitored via changes in 222 nm CD signal at neutral pH. Although it was found to be a fully-folded four-helix bundle in solution, the MIC1 monomer remains rather unstable, with a guanidine hydrochloride unfolding midpoint ($[GuHCl]_u$) of ~1 M and a thermal melting point (T_m) of 39 °C (Figure 3.7 B, C). With the assumption of a two-state unfolding behavior for the MIC1 monomer, a value for $\Delta G_{folding}$ of -9 kJ/mol was obtained.

MIC1 becomes drastically more resistant to chemical and thermal unfolding in its Cu^{II}-induced cage form. The stability values obtained for the Cu-cage equal or slightly surpass those observed for the native HuHF system,[19] with a $[GuHCl]_u$ at 5.2 M and $T_m \geq 87$ °C. Removal of Cu through chelation with EDTA eliminates both intra- and intermonomeric stabilization of the α-helical MIC1 framework by Cu coordination. This causes a shift in $[GuHCl]_u$ and T_m to intermediate values, as they become, respectively, 3.2 M and 71 °C.

Apo-MIC1 cages could be treated with Cu^{II} to "rescue" their stability properties. The Cu was added back by means of slow dialysis, in a method identical to the self-assembly scheme mentioned above. Cage stability was completely recoverable, and, judging from steeper unfolding transitions indicative of more cooperative unfolding behavior, the Cu-reconstituted cage appears to be even more stable in comparison to the isolated Cu-MIC1 cage. This extra stability is likely due to additional Cu binding sites existing on the ferritin cage, which act to further crosslink the ferritin interfaces. An example of additional sites of chelation can be found at the C_4 pores, where four H173 residues, each donated from a separate monomeric building block, can bind a Cu^{II} ion (Figure 3.8). ICP-OES measurements indeed indicate the presence of additional Cu associated with the Cu-reconstituted MIC1 cages: 1.54±0.22 Cu^{II} ions were found bound per monomer. With the apo-cage already in its assembled state, it is unsurprising that additional Cu was detected over the assembling MIC1 24mers, because more sites are initially available to bind metal ions on the pre-formed cage.

Estimations for the values of $\Delta G_{formation}$ were calculated for MIC1 in its cage-like states (apo-, Cu-bound) following the treatment outlined by Swift *et al.*[20] Folding free energies were approximated with the assumption that the MIC1 protein exists in one of two states, where the transition equilibrium "folded 24mer ⇔ unfolded monomer" occurs without observable intermediates. Given this approximation, $\Delta G_{formation}$ of the apo-MIC1 cage is estimated to be -39 kJ/mol per MIC1 monomer (Figure 3.9). Since $\Delta G_{folding}$ was determined to be -9 kJ/mol/monomer of MIC1, one can deduce that cage formation alone imparts 30 kJ/mol of stability per monomer even in the absence of Cu^{II} coordination. Cu-binding contributes an additional 3-6 kJ/mol stability per monomeric protein building block.

The 30-kJ/mol gain in monomer stability upon MIC1 cage formation is comparable to the folding free energy of a stable, globular protein like cytochrome c.[21] This finding clearly showcases how multiple cooperative interactions can produce an exceptionally stable protein architecture out of a generally unstable building block[22] such as MIC1. The fact that Cu coordination adds relatively little to the stability of the MIC1 cage, while being essential for driving cage assembly, reinforces the supposition that the polar interactions that were replaced by Cu coordination at the C_2 interface may primarily guide the cage formation process without providing a significant thermodynamic driving force.

Conclusions

The MIC1 protein, constructed under the design principles of rMeTIR, exhibits chemically-controllable self-assembly properties imparted through engineered Cu^{II} sensitivity. Binding of Cu^{II} triggers the oligomerization of MIC1 monomers into ferritin nanocages, the progress of which can be tracked by solution-state techniques including size exclusion chromatography and sedimentation velocity analytical ultracentrifugation, as well as TEM imaging. The metal-induced organization of MIC1 monomers into 24-meric species is dependent on the stereochemical preferences of the metal ions utilized. The C_2 dimerization interface of MIC1 was engineered such that metals capable of forming square planar arrangements could properly align monomers at that interface through a metal binding event. Therefore, it was no surprise that Cu^{II} binding, and to a lesser extent Zn^{II} binding, initiated cage formation, whereas Ni^{II} failed to do so.

In the MIC1 system, cage assembly is absolutely dependent on metal binding to drive first dimerization and, precipitously, 24mer formation. However, the Cu^{II} “glue” responsible for assembling nanocages from monomers can be removed without consequence of disassembly. This cage persistence phenomenon was supported by a host of experimental endeavors ranging from size exclusion chromatography and sedimentation velocity experiments, to TEM imaging, protein X-ray crystallography, and ICP-OES metal content analysis. Cu^{II}-induced cage formation is partially inhibited with removal of one metal-coordinating His residue

(H60A), or completely inhibited with the reversal variant with mutations H56L/H63R/H67E on the MIC1 template.

Protein X-ray crystal structures of MIC1 compliment the design strategy of rMeTIR. In the Cu-bound MIC1 structure, the square planar Cu^{II} geometry observed is essentially identical to that found in the structure of 4His-ΔC*; the coordinating His clamps become disordered in the apo-MIC1 structure. The E74 mutation illustrates its intended destabilization purpose, with E74' and D42 assuming multiple conformations and pointing away from one another due to electrostatic repulsion. E39 anchors a well-ordered H-bonding network in the Cu-MIC1 structure, which is not present in the metal-free structure. The fact that the apo-cage persists in the absence of Cu^{II} despite mutagenic perturbations of native H-bonding interactions suggests the importance of key polar interactions at the C_2 interface in providing and enforcing geometric specificity, rather than thermodynamic stability, in the cage assembly process. This conclusion is reinforced by the relatively minimal (3-6 kJ/mol) gain observed in stability on a per-monomer basis between the MIC1 apo- and Cu-cages.

The oligomerization process in the self-assembly mechanism of ferritin was proposed to proceed following the folding of monomeric building blocks. Previously, due to experimental limitations, monomer folding and self-association events could not be uncoupled. However, we showed that MIC1 monomers are essentially completely folded 4-helix bundles under physiological pH, and that there is little change in ellipticity as MIC1 proteins proceed from monomeric to cage-like states. Additionally, metal binding does not appear to pre-organize the MIC1 monomer. These findings refute the initial steps of canonical ferritin assembly mechanisms, and also contradict the hypothesis that self-assembly involves the dimerization-coupled folding of the monomers as a first step. Taken together, our results implicate Cu^{II} as a true structural template for the formation of the C_2 dimer of ferritin.

Chapter 3 is reproduced in part with permission from: Huard, D. J. E., Kane, K. M., Tezcan, F. A. 2012. “Engineering Chemical Control into Protein-Protein Interactions: Copper-Templated Ferritin Cage Assembly.” In revision for publication in Nature Chemical Biology.

Table 3.1. Parameters for sedimentation velocity measurements.

	Buffer Density (g/mL)	**Buffer Viscosity (poise)**	**Vbar (mL/g)**	**Theoretical Sedimentation Coefficient (S)**	**Observed Sedimentation Coefficient (S)**
MIC1 Monomer	1.00724	0.010412	0.72	2.091	2.16107
MIC1 Dimer	1.00706	0.010401	0.72	3.364	3.81526
Cu-induced MIC1 cage	1.00706	0.010401	0.72	18.22	19.9598
apo-MIC1 cage	1.00724	0.010412	0.72	18.14	19.3976
Cu-reconstituted MIC1 cage	1.00706	0.010401	0.72	18.24	20.3815

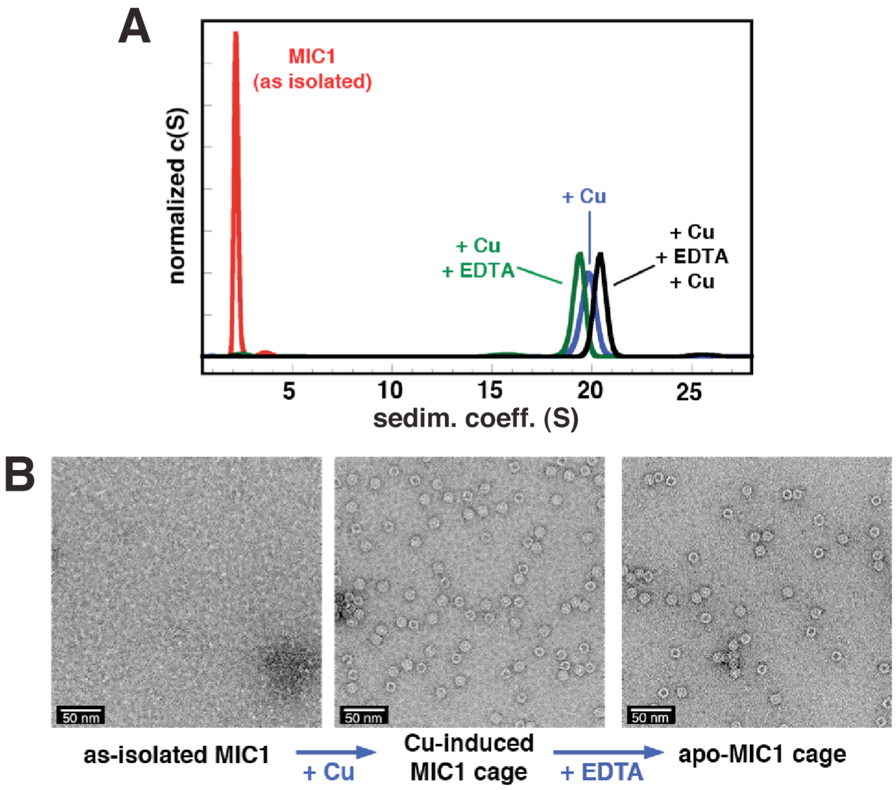

Figure 3.1. Solution assembly properties of MIC1. A) Sedimentation velocity profile of MIC1 in the following states: as-isolated, monomeric (red trace); Cu-bound, cage (blue trace); EDTA-treated, cage (green trace); Cu-reconstituted (black trace). B) Negative-stain TEM images of MIC1, showing the formation of 24mer cages upon Cu^{II} addition, and the retention of the cages upon the subsequent chelation of interfacial Cu's with EDTA.

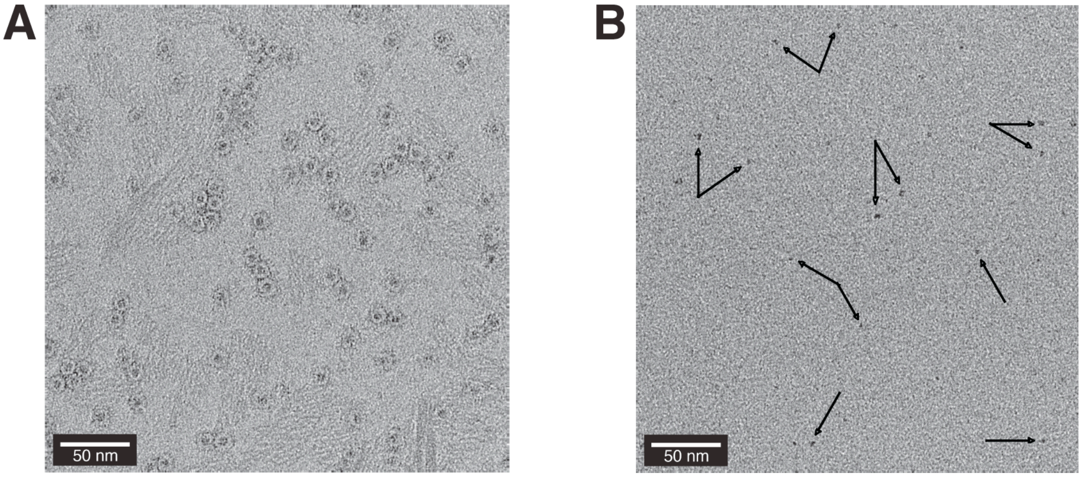

Figure 3.2. The MIC1 Cu^{II}-induced nanocages retain native HuHF enzymatic function as seen by TEM imaging. A) Negative-stain TEM image of MIC1 Cu-cages with Fe cores following treatment of the cages with an $FeSO_4$ salt. Empty nanocages appear as white protein spheres, and cages with Fe cores are visible with darkened interiors. B) TEM image of the Fe-encapsulating Cu-MIC1 cages without stain. The stored Fe nanoparticles appear as small dark spots, indicated by arrows. Without the uranyl acetate stain, the MIC1 protein is no longer visible.

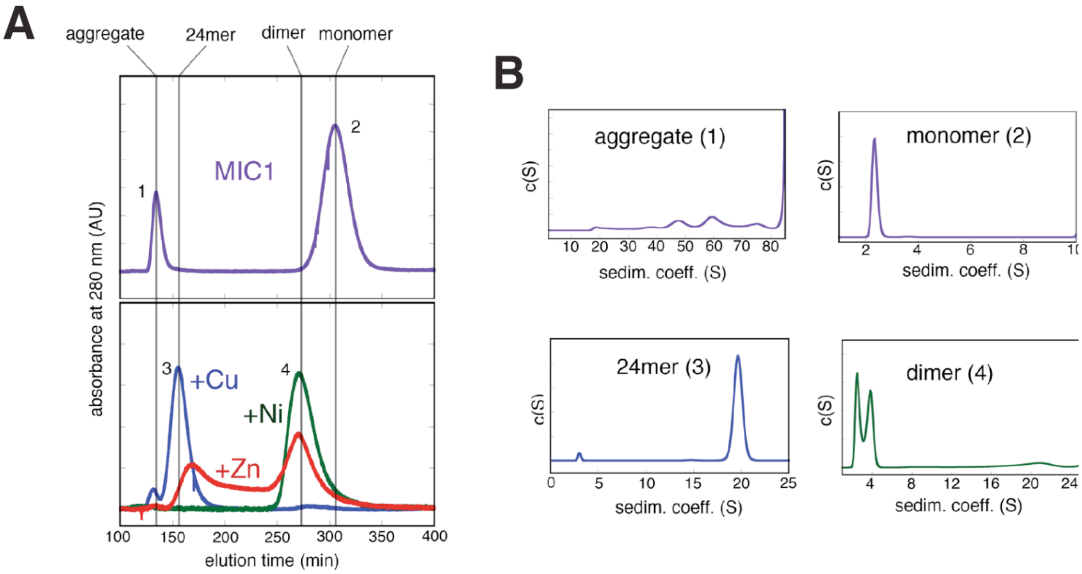

Figure 3.3. Hydrodynamic properties of isolated MIC1 and its metal-mediated oligomers. A) (top) Size-exclusion chromatogram of a MIC1 protein solution, in the presence of EDTA, obtained following protein isolation from inclusion bodies and metal-affinity chromatography. The majority of the protein is in a monomeric state, with a minor fraction existing as large, yet soluble, aggregates that elute in the dead volume. (bottom) Size-exclusion chromatogram of MIC1 exchanged into solutions containing equimolar Cu^{II} (blue trace), Ni^{II} (green trace), and Zn^{II} (red trace). B) Sedimentation profiles of various fractions (indicated with numbers 1-4 in (A)) isolated via size-exclusion chromatography. See Table 3.1 for sedimentation velocity parameters.

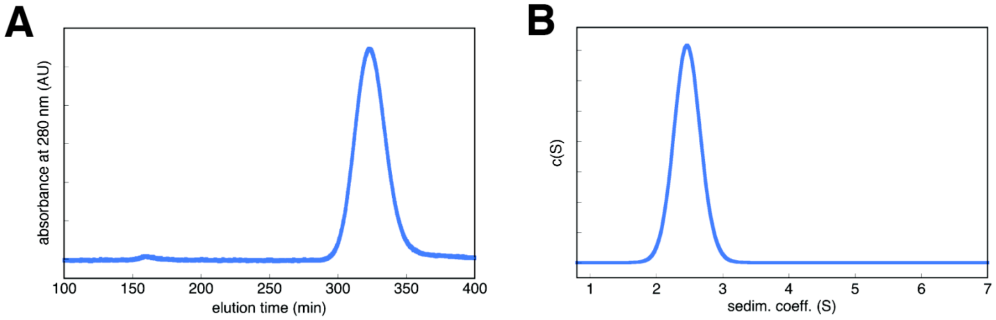

Figure 3.4. Elimination of the Cu^{II}-4His coordination motif with reversal mutations H56L/H63R/H67E prevents Cu-induced cage formation. A) Size-exclusion chromatogram showing that, following Cu^{II} dialysis reaction, the reversal mutant remains monomeric in nature. B) Sedimentation velocity measurements confirm the monomeric state of the MIC1 H56L/H63R/H67E coordination site reversal mutant after reaction of the protein with Cu^{II}.

Table 3.2. X-ray data collection and refinement statistics for protein crystal structures of Cu-MIC1 and apo-MIC1. * denotes highest resolution shell.

	Cu-MIC1	**Apo-MIC1**
Data Collection Location	SSRL BL 9-2	SSRL BL 9-2
Unit Cell Dimensions	a = b = c = 179.6 Å	a = b = c = 181.1 Å
	$\alpha = \beta = \gamma = 90°$	$\alpha = \beta = \gamma = 90°$
Symmetry Group	F432	F432
Resolution (Å)	104.5-1.90	104.5-2.30
X-Ray Wavelength (Å)	0.98	0.98
Number of Unique Reflections	20095	11848
Redundancy	27.1	42.0
Completeness (%)*	99.8 (100)	100 (100)
$\langle I/\sigma I \rangle$*	5.6 (1.4)	6.8 (1.9)
R_{symm} (%)*	10.2 (49.2)	9.7 (39.7)
R_{work} (%)*	21.8 (32.1)	22.0 (25.3)
R_{free} (%)*	24.1 (33.1)	27.2 (30.3)
Number of Atoms		
Protein (including alternative side chain conformations)	1448	1446
Ligands/Ions	17	5
Water	165	93
B-Factors (Å^2)		
Protein	27.3	25.6
Ligands/Ions	37.5	34.1
Water	42.3	31.7
RMS Deviations		
Bond Lengths (Å)	0.007	0.008
Bond Angles (^{o})	0.886	0.996
Ramachandran plot (%)		
Residues in favored regions	98.8	98.2
Residues in allowed regions	1.2	1.8
Residues in generously allowed regions	0.0	0.0
Residues in disallowed regions	0.0	0.0

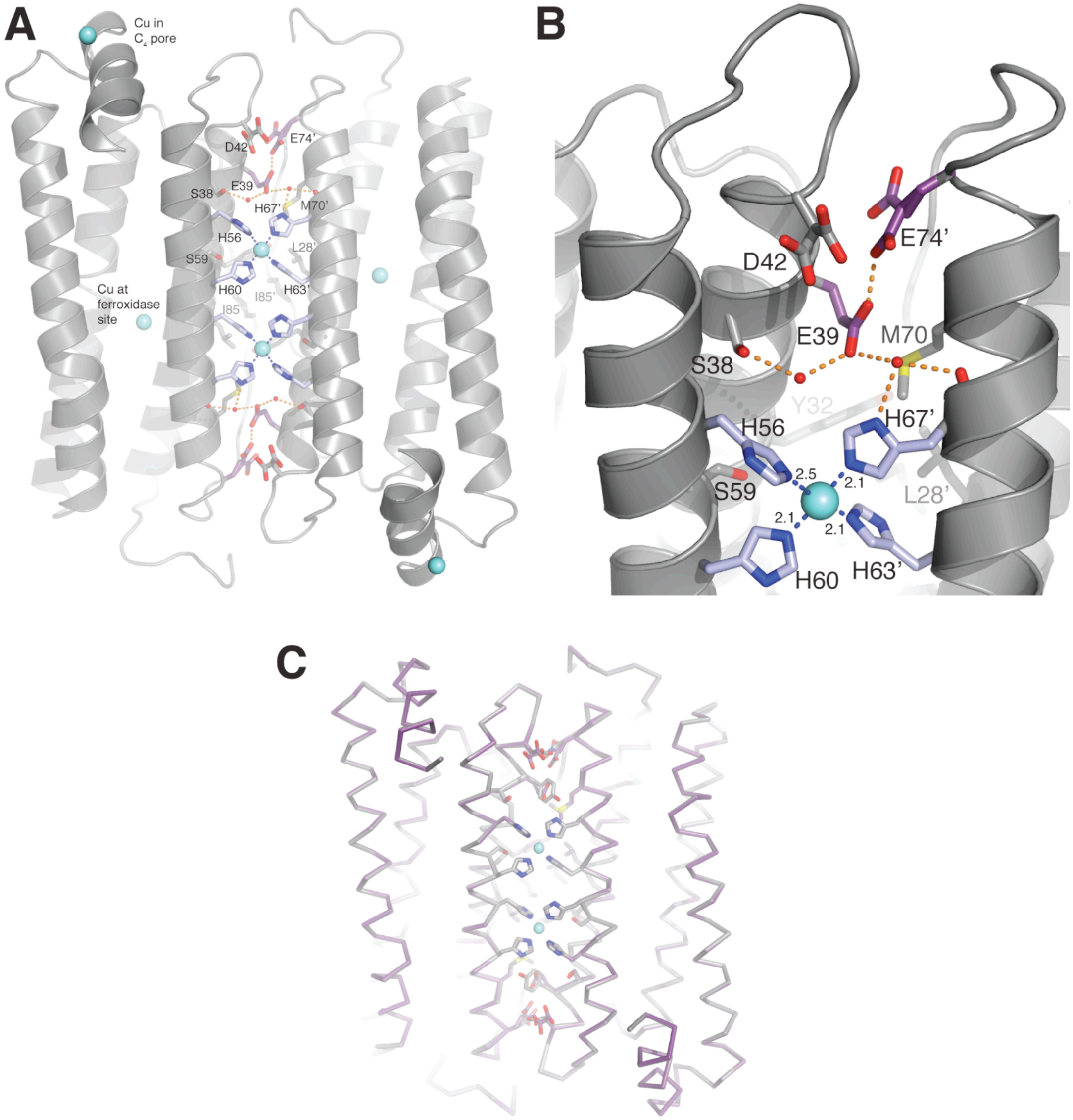

Figure 3.5. Key intersubunit interactions in the C_2 interface of the MIC1 cage in the presence of Cu. A) The C_2 dimer interface of the Cu-MIC1 cage. Mutated residues are colored violet-purple. Interactions between Cu ions (aquamarine spheres) and metal-binding His clamps (silver-blue) are highlighted with blue dashes. Hydrogen bonds are depicted as orange dashes, and water molecules as red spheres. B) Close-up view of half of the C_2 interface. The Y39E and N74E mutations in MIC1 result in a new network of hydrogen bonds, now involving two water molecules. The side chains of E74 and D42 are observed in two alternate conformations (both given in the structure), suggestive of repulsive interactions between the two residues. The Cu coordination as well as the backbone arrangements remain unchanged from 4His-ΔC*. C) Backbone superposition of Cu-4His-ΔC* (gray) and Cu-MIC1 (violet-purple).

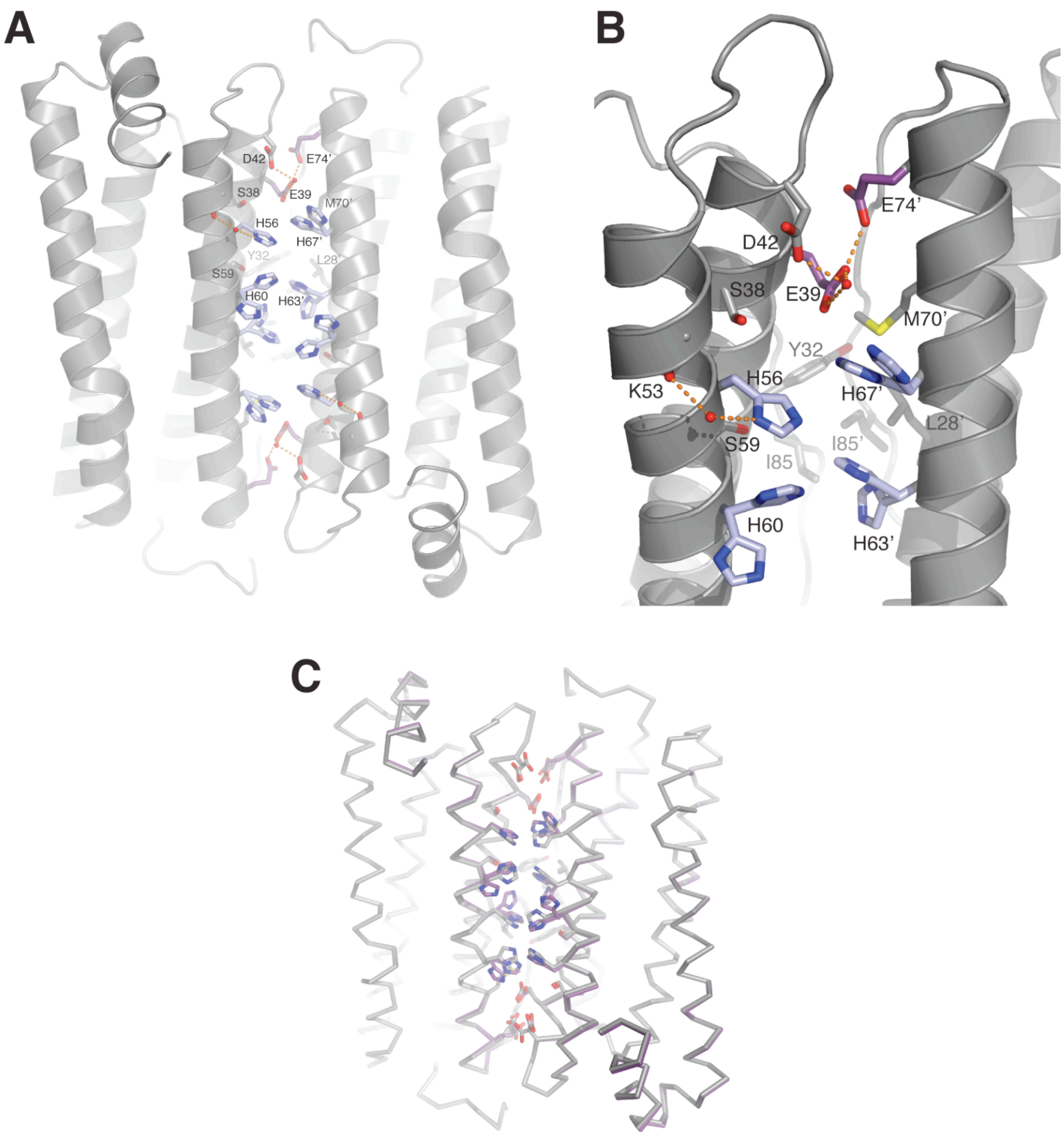

Figure 3.6. Key intersubunit interactions in the C_2 interface of the MIC1 cage in the absence of Cu due to EDTA chelation. A) The C_2 dimer interface of the apo-MIC1 cage. Destabilizing mutation residues 39E and 74E are show in violet-purple. The empty 4His Cu-binding clamps are shown in silver-blue. Hydrogen bonds are represented as orange dashes, and water molecules are shown as red spheres. B) Close-up view of one half of the C_2 interface of EDTA-prepared apo-MIC1. Three of the four coordinating His side chains (H60, H63, and H67) become disordered, as indicated by the presence of multiple conformations presented for each. Only the side chain of H56 is found in a singular orientation, owing to a water-mediated hydrogen bond to the K53 backbone carbonyl group. C) Backbone superposition of Cu-MIC1 (gray) and apo-MIC1 (violet-purple) structures. Upon the removal of Cu coordination, the backbone of MIC1 does not undergo a significant conformational change.

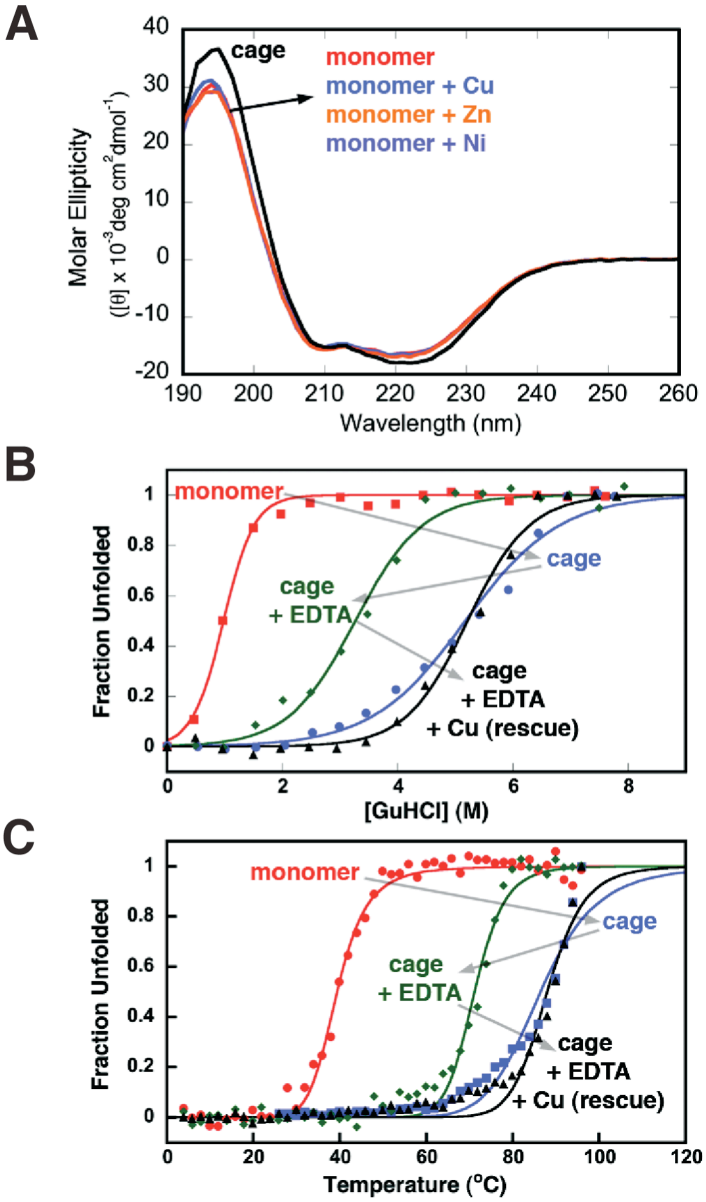

Figure 3.7. Secondary structure and stability of MIC1. A) Far-UV CD spectra of MIC1 in its isolated monomeric state (red trace), in the presence of equimolar Cu^{II} (blue trace), Ni^{II} (magenta trace), Zn^{II} (orange trace), and in the cage form (black trace). B) Guanidine hydrochloride (GuHCl) unfolding titrations of various states of MIC1, performed by monitoring loss of α-helicity of MIC1 by CD spectroscopy at 222 nm. Gray arrows illustrate the shifts in unfolding transitions upon Cu-induced cage formation, removal of Cu from the cage, and reconstitution of the apo-cage with Cu. The coloring scheme is consistent with that in Figure 3.1. The linear relationships between the folding free energy of MIC1 cages and [GuHCl], which were used to determine the stabilities of the cages, are show in Figure X. C) Thermal unfolding of various states of MIC1, performed by monitoring the loss of α-helicity of MIC1 by CD spectroscopy at 222 nm.

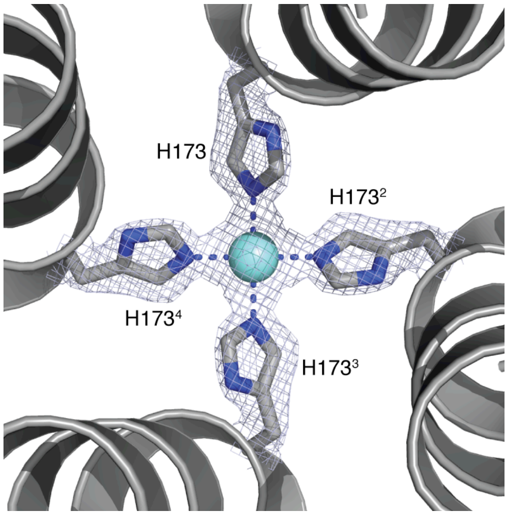

Figure 3.8. Cu^{II} coordination in the C_4 pore of the Cu-MIC1 cage. The $2F_o$-F_c map (silver-blue mesh) is contoured at 1.5 σ. The Cu ion is indicated by the aquamarine sphere.

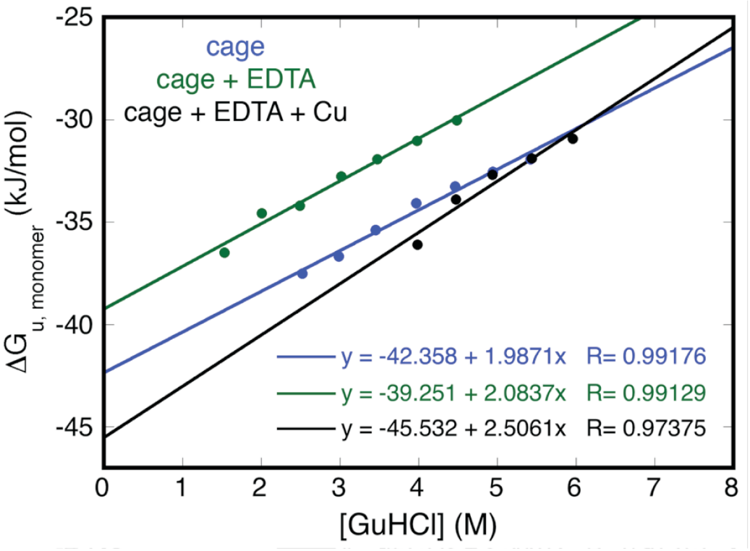

Figure 3.9. Linear relationship between the unfolding free energy of various MIC1 cage species and guanidine hydrochloride (GuHCl) concentrations used to obtain cage stabilities at [GuHCl] = 0 M. (See the relevant section of the Appendix for the description of data treatment.) The coloring scheme matches that in Figures 3.1 and 3.7 B, C).

References

1. Santambrogio, P., et al., *Effects of modifications near the 2-, 3- and 4-fold symmetry axes an human ferritin renaturation.* Biochemical Journal, 1997. **322**: p. 461-468.

2. Salgado, E.N., J. Faraone-Mennella, and F.A. Tezcan, *Controlling protein-protein interactions through metal coordination: Assembly of a 16-helix bundle protein.* Journal of the American Chemical Society, 2007. **129**(44): p. 13374-13375.

3. Salgado, E.N., et al., *Metal-mediated self-assembly of protein superstructures: Influence of secondary interactions on protein oligomerization and aggregation.* Journal of the American Chemical Society, 2008. **130**(19): p. 6082-6084.

4. Salgado, E.N., et al., *Control of Protein Oligomerization Symmetry by Metal Coordination: C(2) and C(3) Symmetrical Assemblies through Cu(II) and Ni(II) Coordination.* Inorganic Chemistry, 2009. **48**(7): p. 2726-2728.

5. Schuck, P., *A model for sedimentation in inhomogeneous media. I. Dynamic density gradients from sedimenting co-solutes.* Biophysical Chemistry, 2004. **108**(1-3): p. 187-200.

6. de la Torre, J.G., M.L. Huertas, and B. Carrasco, *Calculation of hydrodynamic properties of globular proteins from their atomic-level structure.* Biophysical Journal, 2000. **78**(2): p. 719-730.

7. Liu, X. and E.C. Theil, *Ferritin reactions: direct identification of the site for the diferric peroxide reaction intermediate.* Proc Natl Acad Sci U S A, 2004. **101**(23): p. 8557-8562.

8. Winn, M.D., et al., *Overview of the CCP4 suite and current developments.* Acta Crystallographica Section D-Biological Crystallography, 2011. **67**: p. 235-242.

9. Vagin, A. and A. Teplyakov, *MOLREP: an automated program for molecular replacement.* Journal of Applied Crystallography, 1997. **30**: p. 1022-1025.

10. Lawson, D.M., et al., *Solving the Structure of Human H-Ferritin by Genetically Engineering Intermolecular Crystal Contacts.* Nature, 1991. **349**(6309): p. 541-544.

11. Murshudov, G.N., A.A. Vagin, and E.J. Dodson, *Refinement of macromolecular structures by the maximum-likelihood method.* Acta Crystallographica Section D-Biological Crystallography, 1997. **53**: p. 240-255.

12. Emsley, P. and K. Cowtan, *Coot: model-building tools for molecular graphics.* Acta Crystallographica Section D-Biological Crystallography, 2004. **60**: p. 2126-2132.

13. DeLano, W.L., *The PYMOL Molecular Graphics System.* 2003.

14. Zhang, Y., et al., *Alanine-shaving Mutagenesis to Determine Key Interfacial Residues Governing the Assembly of a Nano-cage Maxi-ferritin.* Journal of Biological Chemistry, 2010. **285**(16): p. 12078-12086.

15. Gerl, M., et al., *Self-Assembly of Apoferritin from Horse Spleen after Reversible Chemical Modification with 2,3-Dimethylmaleic Anhydride.* Biochemistry, 1988. **27**(11): p. 4089-4096.

16. Jaenicke, R., *Protein Folding and Protein Association.* Angewandte Chemie International Edition in English, 1984. **23**(6): p. 395-413.

17. Stefanini, S., P. Vecchini, and E. Chiancone, *On the Mechanism of Horse Spleen Apoferritin Assembly - a Sedimentation-Velocity and Circular-Dichroism Study.* Biochemistry, 1987. **26**(7): p. 1831-1837.

18. Lavoie, D.J., et al., *Characterization of ferritin from human placenta. Implications for analysis of tissue specificity and microheterogeneity of ferritins.* Biochimica et Biophysica Acta, 1979. **579**(2): p. 359-366.

19. Butts, C.A., et al., *Directing Noble Metal Ion Chemistry within a Designed Ferritin Protein.* Biochemistry, 2008. **47**(48): p. 12729-12739.

20. Swift, J., et al., *Design of functional ferritin-like proteins with hydrophobic cavities.* Journal of the American Chemical Society, 2006. **128**(20): p. 6611-6619.

21. Mines, G.A., et al., *Cytochrome c folding triggered by electron transfer.* Chemistry and Biology, 1996. **3**(6): p. 491-497.

22. Zlotnick, A., *To Build a Virus Capsid - an Equilibrium-Model of the Self-Assembly of Polyhedral Protein Complexes.* Journal of Molecular Biology, 1994. **241**(1): p. 59-67.

Chapter 4.

Chemical Modification of the Ferritin Cage Interior: Labeling ^{C53}MIC1 with AEDANS

Introduction

Beyond expanding the understanding of the process of self-assembly of the cage-like protein HuHF, the goal of applying reverse metal-templated interface redesign to ferritin and instilling chemical control over its PPIs has myriad practical applications. A majority of these applications require access to the ferritin core, an 8 nm cavity employed toward iron storage in the native system.[1] Cage-like proteins including ferritin are attractive for materials applications because they present favorable characteristics such as high degrees of solubility, stability (both chemical and thermal), and symmetry, as well as properties like biocompatibility, uniformity of size, and ease of engineering through chemical and genetic manipulation.[2-4] Molecular entrapment by and sequestration in the nanocages is limited in scope of potential guests due to restrictive pore sizes. Many systems are reliant upon guest diffusion for encapsulation, which precludes larger targets if cage entranceways are small, or proper sequestration if pores are too large.

In the ferritin protein family, to which HuHF belongs, the C_3- and C_4-symmetric pores modulate guest molecule access to the cage-like cavity. These pores are <4 Å in size, and consequently limit guest identity to natural substrates and small species including metal ions and small metal complexes. In all cases, entrapment of guest molecules is reliant upon diffusion into the nanocage space. Despite the restrictive nature of this system in terms of potential cargo, materials applications of ferritin abound in the literature, ranging from catalysis efforts[5, 6] to nanomaterials synthesis[7-11] and biosensor production[12, 13].

In an effort to combat pore size restriction and increase the diversity of potential guest molecules–a direct correlate of the utility of the ferritin system–Webb *et al.* developed a scheme whereby which access to the core could be granted in a pH-dependent fashion.[14] Decreasing the pH of the ferritin environment down to 2 triggers nanocage disassembly; restoring the protein solution pH back to neutrality allows for 24mer reassembly (Figure 4.1 A). If this process is performed in the presence of small guest molecules, they might become trapped during the reassembly process. This methodology has been utilized, for example, in the compartmentalization of a gadolinium complex for the purposes of preparing an enhanced magnetic resonance imaging (MRI) contrast agent[15], and in the entrapment of platinum anticancer drugs to create a biocompatible drug-delivery system.[16, 17] In general, however, the pH-driven encapsulation strategy struggles with setbacks. Entrapment yields are low because the technique still depends on passive encapsulation. Material loss arising from the necessity of using a pH of 2 for disassembly also contributes to low entrapment efficiencies. Concomitantly, the acidic conditions needed to monomerize ferritin preclude protocols for the covalent or coordinative coupling of substrates to the building block surfaces.

The MIC1 variant of HuHF we designed through rMeTIR grants immediate access to the inner core of the 24-meric assembly. In the absence of metal ions (particularly Cu^{II}) MIC1 is a monomeric species. The monomers persist at neutral pH, allowing for the chemical or coordinative modification of the surfaces of these protein building blocks. We hypothesized that treating labeled or modified MIC1 with Cu^{II} would allow for the active encapsulation of guest species (Figure 4.1 B). This scheme is superior to the pH-driven entrapment technique in that cargo yields can be both enhanced and tightly controlled in a stoichiometric fashion. Also, the diversity of potential guest molecules for the nanocages becomes nearly limitless, so long as the molecules can fit in the 24mer core space.

As a proof of concept, we decided to take advantage of the relative ease of crystallization of MIC1 and use the protein nanocage as a scaffold to access the crystal structure of a guest molecule. The goal of employing Cu^{II}-induced MIC1 cages to facilitate crystallization of molecular targets not only highlights a practical application of using top-down strategies to control PPIs in cage-like protein systems, but also demonstrates stoichiometric control over encapsulated cargo. In the Tezcan laboratory, a similar approach using a cytochrome cb_{562} cage-forming variant allowed for the determination of a novel solid-state structure of a microperoxidase.[18] Yet, unlike the case of MIC1, this cytochrome system has the limitation that the protein cage is not isolable in solution, thereby limiting its use in guest-molecule co-crystallization. In this study, we chose a cargo target small enough in scale so as not to sterically prevent Cu^{II}-induced cage assembly; our guest was 5-({2-[iodoacetyl)amino]ethyl}amino)naphthalene-1-sulfonic acid (IAEDANS), a common fluorophore. Successful implementation of this strategy paves the way for use in the potential entrapment and structural characterization of flexible and crystallographically recalcitrant substrates, as well as applications beyond crystallography into the realms of biological sensing and drug delivery.

Materials and Methods

Site-Directed mutagenesis and protein expression, purification, and characterization. The MIC1 template was modified employing QuikChange mutagenesis (Stratagene) with primers from Integrated DNA Technologies. Mutant plasmids were transformed into XL-1 Blue *E. coli* cells and purified using the QIAprep Spin Miniprep kit (Qiagen). Variant plasmid sequencing was performed by Retrogen.

The ^{C53}MIC1 mutant DNA was transformed into BL21 (DE3) *E. coli* cells for expression as outlined before.

The ^{C53}MIC1 protein was shunted into–and therefore isolated from–inclusion bodies. Protein purification protocols for this variant were slightly modified from those given for MIC1 and other muteins. Following liberation of the protein from the inclusion body pellet, it was exchanged into an 8 M urea-denaturing buffer maintained at pH 7.4 with 20 mM NaH_2PO_4 containing 1 M NaCl. Purification was carried out with metal-affinity chromatography with a HisPrep FF 16/10 column charged with $CuSO_4$, running an imidazole step gradient of 0 to 0.25 M imidazole in the aforementioned urea buffer. After elution from the column, the ^{C53}MIC1 protein was exhaustively dialyzed into standard buffer (15 mM Tris buffered at pH 7.4 and with 150 mM NaCl) containing 10 mM EDTA. Additionally, at least 1 mM DTT reductant was maintained in the purified protein solution to ensure prevention of undesired disulfide bond formation between ^{C53}MIC1 monomers. Any aggregated or misfolded ^{C53}MIC1 protein present was not removed by size exclusion chromatography at this point, as in the case of MIC1. Protein purity and veracity were confirmed by SDS-PAGE gel electrophoresis and MALDI-TOF mass spectrometry. Stocks of purified protein were frozen with liquid N_2 and stored at -80 °C prior to use.

Chemical modification of ^{C53}MIC1 with IAEDANS. Frozen stocks of ^{C53}MIC1 were slowly thawed, and the protein was quantified by the Bradford assay. With fresh standard buffer containing 10 mM EDTA and 5 mM DTT, the protein was diluted to a concentration of 15 μM. Following dilution, the protein solution was then further dialyzed against the dilution buffer, and portions of this were degassed and brought into an anaerobic chamber. Once in an anaerobic environment, the ^{C53}MIC1 protein was exchanged into degassed, Chelex-treated standard buffer to remove DTT and

EDTA. Immediately following, the proteins samples were reacted with 1.5 mM 5-({2-[iodoacetyl)amino]ethyl}amino)naphthalene-1-sulfonic acid IAEDANS, a common fluorophore, in darkness with stirring for 1 hour. Unreacted label was removed with the aid of Econo-Pac 10DG Desalting Columns (Bio-Rad). Quantitative modification of ^{C53}MIC1 with AEDANS was confirmed by MALDI-TOF mass spectrometry. The labeled protein was kept in darkness for the duration of its use.

Fluorescence properties of AEDANS-modified ^{C53}MIC1. Fluorescence spectroscopy measurements were performed on the probe-labeled ^{C53}MIC1 protein as further confirmation of modification. AEDANS-labeled protein at 1.3 μM concentration in the standard buffer with 10 mM EDTA was placed in a 1-cm pathlength quartz cuvette and subjected to fluorescence spectroscopy characterization. Measurements were taken with a Horiba Jobin Yvon Fluorolog-3 Spectrofluorometer, with excitation at 336 nm and maximal emission monitored at 441 nm. Excitation and emission slits were maintained at 5 nm, being modulated only if emission signal surpassed the dynamic range of the instrument; sample integration time was 0.25 seconds per nm. Fluorescence scans of buffer alone and supplemented with free IAEDANS were performed as controls.

X-ray crystallography. Protein crystals of Cu^{II}-bound AEDANS-^{C53}MIC1 were obtained by the sitting-drop vapor diffusion method. The sitting drops yielding diffraction-quality crystals consisted of 2 μL of protein solution and 2 μL of precipitant solution. The wells contained 500 μL of precipitant solution. The protein solution was constituted of 666 μM of AEDANS-modified ^{C53}MIC1 in standard buffer, or 15 mM Tris maintained at pH 7.4 and including 150 mM NaCl. The precipitant consisted of 50 mM Tris buffered at pH 8.0, with 5 mM $CaCl_2$ and 350 μM $CuCl_2$. The precipitant solution also contained 10% (by weight) PEG 3350. The crystal trays were set up and maintained in darkness for the duration of crystal growth, which concluded after approximately a one-month interval. Protein crystals were cryoprotected with the addition of ~1 μL of glycerol directly to the 4-μL well solution containing crystals, and the crystals were pulled through this glycerol layer and immediately frozen in liquid N_2.

X-ray diffraction data were collected at 100 K at Beamline 9-2 of the SSRL facility using 0.98-Å radiation. For the identification of Cu centers through anomalous scattering, data were also collected at the Cu K-edge (1.3 Å). Diffraction data were processed using MOSFLM and SCALA.[19] The crystal structure of Cu^{II}-bound, AEDANS-modified ^{C53}MIC1 was solved with molecular replacement by MOLREP[20] using the structure of the K86Q[21] mutant (PDB ID: 2CEI) as a model. The structure of the dansyl fluorophore is available online in the PDB database (PDB ID: AEN).[22] Rigid-body, positional and thermal refinement was carried out using REFMAC,[23] along with iterative manual model building with COOT.[24] Atomic coordinates and structure factors for the crystal structure of Cu-dansyl-^{C53}MIC1 have been deposited into the Protein Data Bank with the identification number 4DZ0. All structural figures were produced using PYMOL.[25]

Results and Discussion

Active encapsulation and crystallization of a guest molecule with the ferritin nanocage employing the Cu^{II} self-assembly responsiveness of HuHF variant MIC1. The process of chemical modification of MIC1 monomers for the purposes of demonstrating the functional utility of accessing the inner cavity of cage-like protein ferritin began with a scan of the core surface for ideal positioning of substrates. The objective was to harness the facile crystallizability of MIC1 (HuHF) to structurally characterize a cargo molecule. Cysteine chemistry was decided as the mode of linking an iodinated dansyl guest (IAEDANS) to the protein surface. The AEDANS fluorophore is an ideal molecule for proof-of-principle modification, as it is small enough to be innocuous and not, based on steric arguments, inhibit cage assembly. Position 53 was chosen for mutation to a Cys residue, as it faces the interior cavity of the ferritin 24mer (Figure 4.2). Importantly, Cys53 is not involved in the C_2 dimerization interface.

As expected, the variant ^{C53}MIC1, like its parent counterpart, was expressed in inclusion bodies and was shown to be monomeric in solution in the absence of metal ions. Due to the presence of the engineered Cys residue at position 53, the protein had to be kept reduced to avoid unwanted disulfide bond formation; sedimentation velocity experiments indicated that oxidized protein samples existed in aggregated states with a high degree of polydispersity. ^{C53}MIC1 in its monomeric form was reacted with IAEDANS, and dansyl modification was found quantitative as gauged by MALDI-TOF mass spectrometry. The expected mass of AEDANS-modified ^{C53}MIC1 is 21,305.77 Da, and a mass of 21,310.13 Da was observed, with no unmodified protein present. Fluorescence measurements indeed indicate the presence of the label on the HuHF variant, with characteristic excitation and emission maxima at 336 nm and 441 nm, respectively (Figure 4.3).

The protein crystal structure of the dansyl-functionalized ^{C53}MIC1 cage was determined at 2.5-Å resolution (see Table 4.1 for refinement statistics). Formation of the modified nanocages was facilitated with Cu^{II}, which was added to the precipitant solution. The obtained structure shows that the dansyl groups are aligned parallel to the C_2 interface and extend over the Cu coordination sites (Figure 4.5). Aside from the covalent thioether bond to residue Cys53 and an H-bond from the amide carbonyl of the linker to the H56 sidechain, each naphthyl moiety only makes long-distance (>3.4 Å) contacts with H56, H57, and H60. This limited amount of interactions with the cage surface account for the higher average B-factor of the dansyl group (65 Å^2) compared to the cage scaffold (38 Å^2). Nevertheless, the electron density for each AEDANS group can be traced along the entire length of the molecule.

Conclusions

Rendering the oligomerization state of HuHF chemically-controllable through metal binding with the rMeTIR strategy has allowed for access to the ferritin cage interior through means of direct manipulation of the nanocage monomeric building blocks. Monomers, once obtainable only under very acidic (pH of 2) conditions and thus precluding most chemical modification schemes, are now available for decoration with a host of substrate molecules previously unavailable to the ferritin interior. Not only does this technique expand the diversity of possible guests for encapsulation, but it provides a means for controlling the absolute stoichiometry of species trapped in the 24mer cavity.

To demonstrate the ability to introduce new substrates into the ferritin cavity in a specific, highly-controlled fashion, MIC1 monomers with the C53 mutation, which faces the cage interior, were modified with thiol-reactive IAEDANS. The ^{C53}MIC1 protein was quantitatively labeled with the dansyl fluorophore, and utilized to prepare diffraction-quality protein crystals. (Cu^{II} was included in the precipitation solution to encourage cage assembly from guest-bound building blocks.) In this way, the crystal structure of the ferritin guest molecule, along with the protein scaffold, was obtained.

We envision implementation of this strategy to afford the entrapment of crystallographically challenging substrates with the goal of structural characterization. Beyond the realm of crystallography, guests including bioimaging agents, catalysts, and drug molecules might be sequestered within ferritin to further push the scope of this protein as a nanovessel.

Chapter 4 is reproduced in part with permission from: Huard, D. J. E., Kane, K. M., Tezcan, F. A. 2012. Engineering Chemical Control into Protein-Protein Interactions: Copper-Templated Ferritin Cage Assembly. In revision for publication in Nature Chemical Biology.

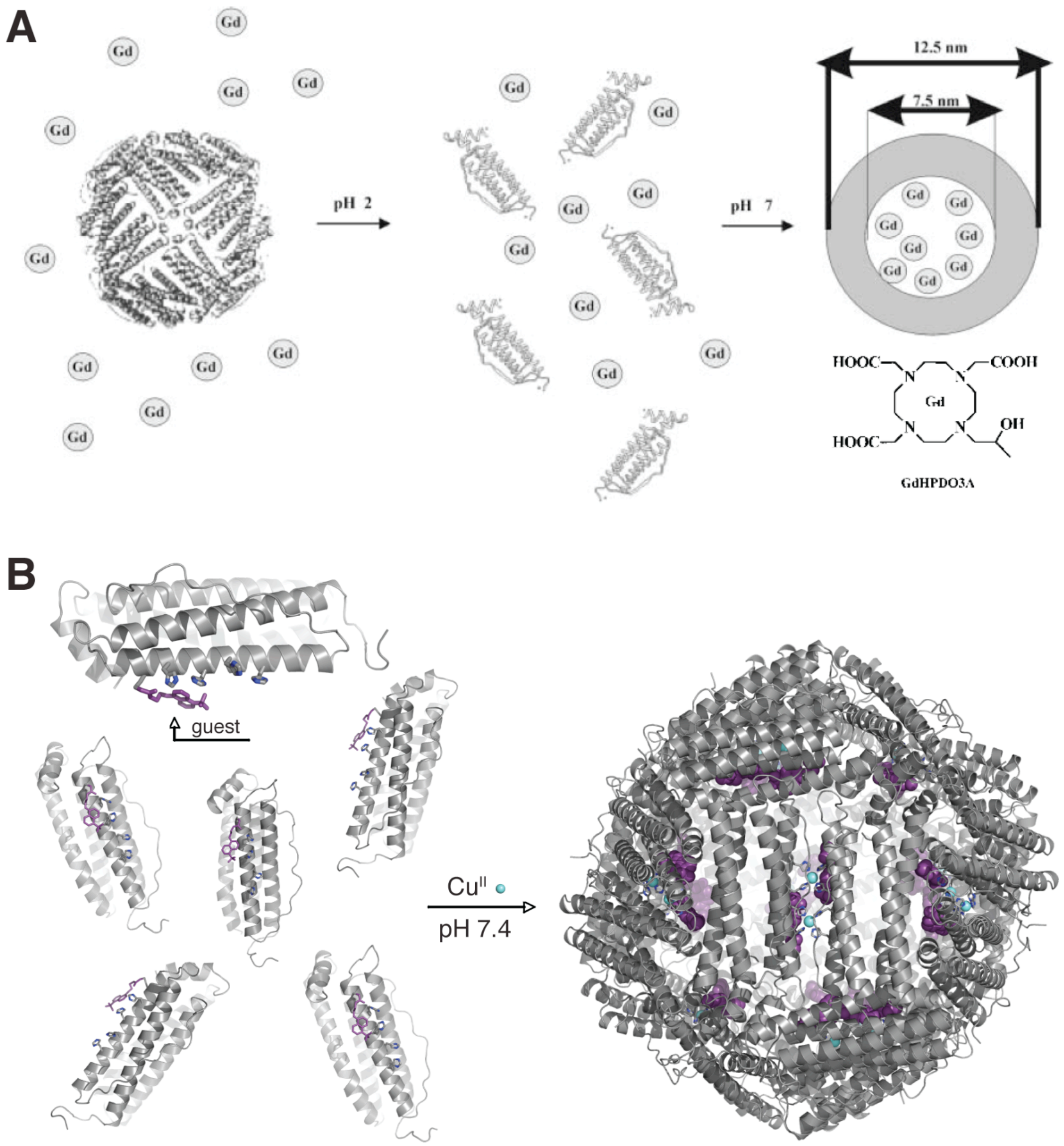

Figure 4.1. Schemes by which to access the core interior of ferritin nanocages. A) Schematic representation of the canonical pH-driven ferritin encapsulation methodology, where cage dissociation is triggered by a pH of 2, and entrapment of small molecules occurs by adjusting the pH back to 7, which leads to the re-forming of cages, in the presence of guest species (adapted from reference 15). B) Schematic illustrating metal-directed protein self-assembly applied to the MIC1 ferritin system to actively encapsulate guest molecules in a stoichiometrically controlled fashion. MIC1 monomers modified with a substrate (violet-purple) assemble into 24mer cages in the presence of Cu^{II} (aquamarine spheres), leading to the active entrapment of the substrate.

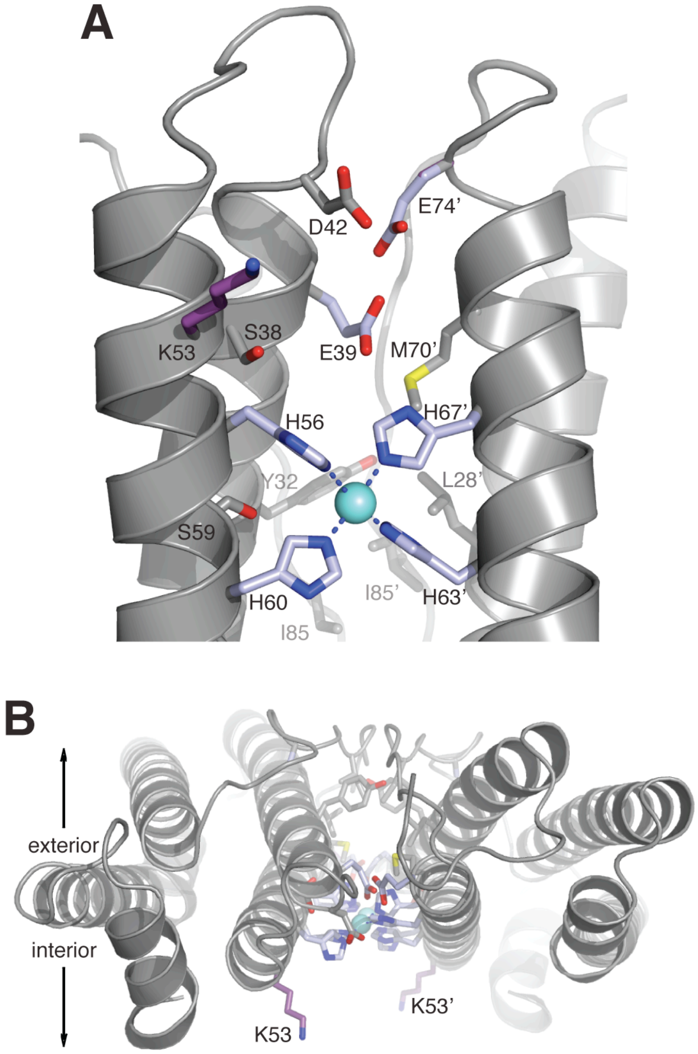

Figure 4.2. Visualizing residue K53, the target of mutagenesis for the purposes of MIC1 modification by cysteine chemistry, in the context of the MIC1 C_2 dimer interface. A) Close-up view of the half of the C_2 interface of the Cu-MIC1 structure, highlighting the fact that K53 (violet-purple) points away from the C_2 dimerization surface. Mutations relevant to MIC1 are colored silver-blue. The interaction of Cu^{II} (aquamarine sphere) with the engineered 4His coordination motif is depicted by blue dashes. Mutated residues E39 and E74 are show in one position for clarity. B) Top-down view of the Cu-MIC1 cage C_2 interface, emphasizing that residue K53 points into the interior cavity of the ferritin nanocage. Modification of this residue should allow for active encapsulation of guest molecules into the 24mer core following Cu^{II}-induced self-assembly of the decorate monomers.

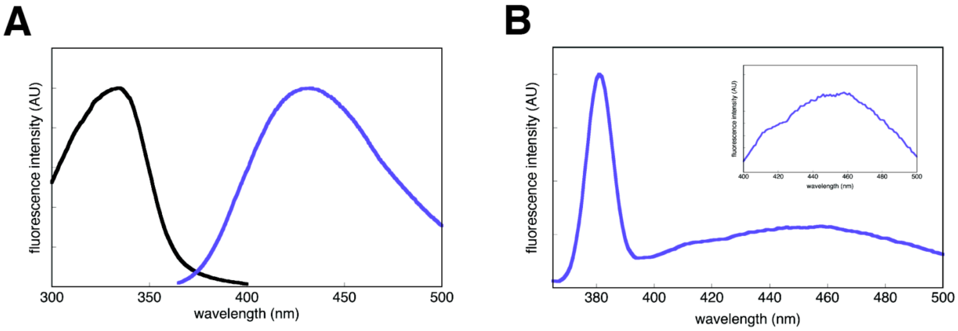

Figure 4.3. Fluorescence properties of the dansyl-modified ^{C53}MIC1 protein. A) Dansyl excitation (black trace) and emission (blue-violet trace) spectra in the standard buffer (15 mM Tris buffered at pH 7.4 and with 150 mM NaCl) containing 10 mM EDTA. B) Fluorescence emission spectrum of the ^{C53}MIC1 variant modified with AEDANS, in the standard buffer supplemented with 10 mM EDTA to maintain protein monomerization. The spectrum includes the water Raman signature as a reference. Inset is a blow-up view of the emission maximum.

Table 4.1. X-ray data collection and refinement statistics for the protein crystal structure of Cu-AEDANS-^{C53}MIC1. * denotes highest resolution shell.

	Cu-AEDANS-^{C53}MIC1
Data Collection Location	SSRL BL 9-2
Unit Cell Dimensions	a = b = c = 180.4 Å
	$\alpha = \beta = \gamma = 90°$
Symmetry Group	F432
Resolution (Å)	104.1-2.50
X-Ray Wavelength (Å)	0.98
Number of Unique Reflections	9200
Redundancy	20.3
Completeness (%)*	100 (100)
$\langle I/\sigma I \rangle$*	7.5 (1.9)
R_{symm} (%)*	8.5 (40.5)
R_{work} (%)*	22.4 (29.4)
R_{free} (%)*	30.0 (35.3)
Number of Atoms	
Protein (including alternative side chain conformations)	1416
Ligands/Ions	27
Water	51
B-Factors (Å^2)	
Protein	38.1
Ligands/Ions	61.7
Water	40.2
RMS Deviations	
Bond Lengths (Å)	0.009
Bond Angles (^{o})	0.953
Ramachandran plot (%)	
Residues in favored regions	98.2
Residues in allowed regions	1.8
Residues in generously allowed regions	0.0
Residues in disallowed regions	0.0

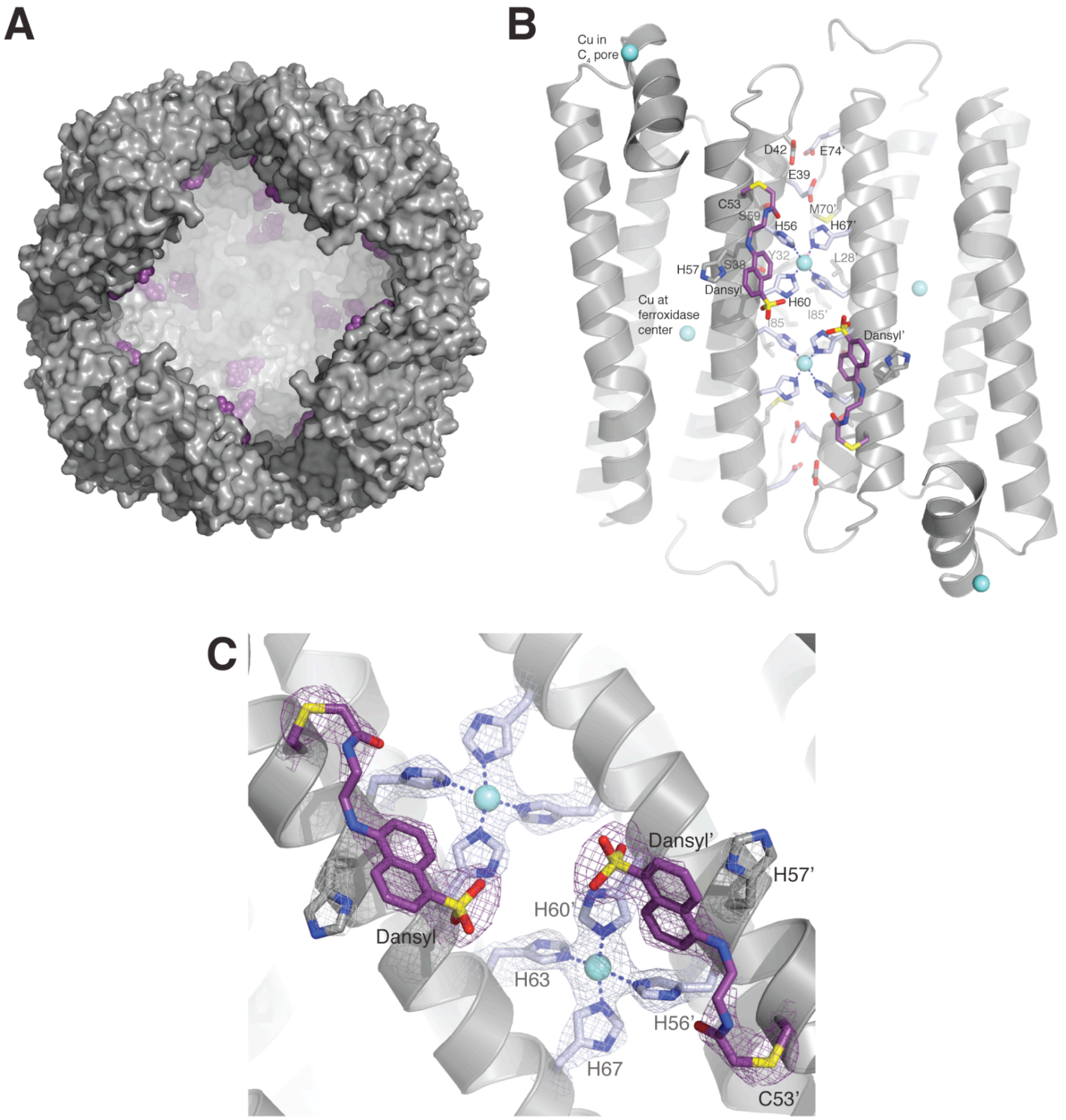

Figure 4.4. Dansyl-modified ^{C53}MIC1 cage. A) View of the Cu-^{C53}MIC1 cage with AEDANS modification. The dansyl substrate is colored violet-purple, and lies within the cage interior. Each ^{C53}MIC1 monomer has one bound dansyl moiety, and thus the cargo of the nanocage is very much under stoichiometric control, due to the active mode of guest encapsulation. B) View of the C_2 dimer interface of the Cu-cage of dansyl-^{C53}MIC1. The AEDANS molecules are shown in violet-purple, along with the C53 residues to which they are bound. Relevant mutations constituting MIC1 (copper coordination motif, E39, and E74) are colored silver-blue. Blue dashes indicate interactions of the copper ions (aquamarine spheres) with the coordination motifs. C) Close-up view of the C_2 dimerization interface, highlighting the location of the dansyl moieties in the context of the Cu-4His coordination site. The $2F_o$-F_c electron density maps are contoured at 1.5 σ (silver-blue mesh) and 0.8 σ (violet-purple mesh).

References

1. Liu, X.F. and E.C. Theil, *Ferritins: Dynamic management of biological iron and oxygen chemistry.* Accounts of Chemical Research, 2005. **38**(3): p. 167-175.

2. Douglas, T. and M. Young, *Viruses: Making friends with old foes.* Science, 2006. **312**(5775): p. 873-875.

3. de la Escosura, A., R.J.M. Nolte, and J.J.L.M. Cornelissen, *Viruses and protein cages as nanocontainers and nanoreactors.* Journal of Materials Chemistry, 2009. **19**: p. 2274-2278.

4. Vriezema, D.M., et al., *Self-assembled nanoreactors.* Chemical Reviews, 2005. **105**(4): p. 1445-1489.

5. Abe, S., et al., *Polymerization of Phenylacetylene by Rhodium Complexes within a Discrete Space of apo-Ferritin.* Journal of the American Chemical Society, 2009. **131**(20): p. 6958-6960.

6. Suzuki, M., et al., *Preparation and catalytic reaction of Au/Pd bimetallic nanoparticles in apo-ferritin.* Chemical Communications, 2009(32): p. 4871-4873.

7. Meldrum, F.C., et al., *Synthesis of inorganic nanophase materials in supramolecular protein cages.* Nature, 1991. **349**: p. 684-687.

8. Allen, M., et al., *Protein Cage Constrained Synthesis of Ferrimagnetic Iron Oxide Nanoparticles.* Advanced Materials, 2002. **14**(21): p. 1562-1565.

9. Galvez, N., et al., *A bioinspired approach to the synthesis of bimetallic CoNi nanoparticles.* Inorganic Chemistry, 2010. **49**(4): p. 1705-1711.

10. Kasyutich, O., et al., *Silver ion incorporation and nanoparticle formation inside the cavity of Pyrococcus furiosus ferritin: structural and size-distribution analyses.* Journal of the American Chemical Society, 2010. **132**(10): p. 3621-3627.

11. Polanams, J., A.D. Ray, and R.K. Watt, *Nanophase iron phosphate, iron arsenate, iron vanadate, and iron molybdate minerals synthesized within the protein cage of ferritin.* Inorganic Chemistry, 2005. **44**(9): p. 3203-3209.

12. Sun, C., et al., *Controlling assembly of paired gold clusters within apoferritin nanoreactor for in vivo kidney targeting and biomedical imaging.* Journal of the American Chemical Society, 2011. **133**(22): p. 8617-8624.

13. Wu, H., et al., *Synthesis of lutetium phosphate-apoferritin core-shell for potential applications in radioimmunoimaging and radioimmunotherapy of cancers.* Journal of Materials Chemistry, 2008. **18**: p. 1779-1783.

14. Webb, B., et al., *Molecular Entrapment of Small Molecules within the Interior of Horse Spleen Ferritin.* Archives of Biochemistry and Biophysics, 1994. **309**(1): p. 178-183.

15. Aime, S., L. Frullano, and S.G. Crich, *Compartmentalization of a gadolinium complex in the apoferritin cavity: A route to obtain high relaxivity contrast agents for magnetic resonance imaging.* Angewandte Chemie-International Edition, 2002. **41**(6): p. 1059-1061.

16. Xing, R.M., et al., *Characterization and cellular uptake of platinum anticancer drugs encapsulated in apoferritin.* Journal of Inorganic Biochemistry, 2009. **103**(7): p. 1039-1044.

17. Yang, Z., et al., *Encapsulation of platinum anticancer drugs by apoferritin.* Chemical Communications, 2007(33): p. 3453-3455.

18. Ni, T.W. and F.A. Tezcan, *Structural characterization of a microperoxidase inside a metal-directed protein cage.* Angewandte Chemie International Edition (English), 2010. **49**(39): p. 7014-7018.

19. Winn, M.D., et al., *Overview of the CCP4 suite and current developments.* Acta Crystallographica Section D-Biological Crystallography, 2011. **67**: p. 235-242.

20. Vagin, A. and A. Teplyakov, *MOLREP: an automated program for molecular replacement.* Journal of Applied Crystallography, 1997. **30**: p. 1022-1025.

21. Lawson, D.M., et al., *Solving the Structure of Human H-Ferritin by Genetically Engineering Intermolecular Crystal Contacts.* Nature, 1991. **349**(6309): p. 541-544.

22. Baudet-Nessler, S., et al., *Crystal structure of a fluorescent derivative of RNase A.* Biochemistry, 1993. **32**(33): p. 8457-8464.

23. Murshudov, G.N., A.A. Vagin, and E.J. Dodson, *Refinement of macromolecular structures by the maximum-likelihood method.* Acta Crystallographica Section D-Biological Crystallography, 1997. **53**: p. 240-255.

24. Emsley, P. and K. Cowtan, *Coot: model-building tools for molecular graphics.* Acta Crystallographica Section D-Biological Crystallography, 2004. **60**: p. 2126-2132.

25. DeLano, W.L., *The PYMOL Molecular Graphics System.* 2003.

Chapter 5.

Dissertation Conclusions and Future Directions of Research

Dissertation Conclusions

The goal of this dissertation was to engineer chemical control over the self-assembly of cage-like protein human H-ferritin, with the expectation of gaining a better understanding of the protein-protein interactions that govern this system as well as creating a means to better exploit it for practical applications. The strategy employed to render the HuHF oligomerization state responsive to external stimuli, in the form of a metal binding event, was termed rMeTIR, or reverse metal-templated interface redesign. The rMeTIR methodology is comprised of two phases. In the first phase, metal coordination motifs are grafted onto a symmetry-related protein-protein interface to provide a means of effectively stitching up that interface upon metal binding. During the second stage or redesign, the PPI interface is subjected to mutagenic perturbation such that PPIs become exclusively metal-driven.

The C_2 dimerization interface of HuHF template protein ΔC^* was targeted for redesign. Two sets of 4His metal coordination motifs were installed onto the template, and shown crystallographically to bind Cu^{II} with square planar geometry; this variant was termed 4His-ΔC^*. A number of C_2 interface residues were then screened via site-directed mutagenesis to create an HuHF variant with the characteristic of being exclusively monomeric in the absence of metal ions, and capable of forming 24-meric ferritin cages upon the addition of, in particular, Cu^{II}. The variant with the best “switch” capability was termed MIC1, for metal-induced cage variant 1.

The MIC1 protein was shown to completely undergo the monomer-to-cage transition when exposed to Cu^{II}. As predicted, other divalent late-first-row transition metal ions such as Ni^{II} and Zn^{II} proved incapable of the same degree of cage conversion. This inefficiency is due to the alternative stereochemical preferences of these other metal ions. Interestingly, as confirmed by a variety of experimental means, the Cu "glue" responsible for directing MIC1 self-assembly into nanocages can be removed from the 24mer without the consequence of losing its cage-like architecture. Cu^{II} behaves as a true template for cage formation in that, once it helps guide the correct alignment of MIC1 monomers at the C_2 PPI interface (thereby overriding perturbations put into place with mutations Y39E, N74E and P88A), it can be removed with the thermodynamically- and kinetically-stable cage intact. Our findings suggest that the polar interactions altered in the process of designing MIC1 are responsible for providing the geometric specificity (now imposed by Cu-binding) allowing cage formation in the native system.

An exploration of the thermodyamics of folding and self-assembly of the MIC1 protein system led to some conclusions about the early stages of the assembly mechanism of HuHF and other ferritins. It has been proposed that cage formation is initiated by first a folding event of the monomeric protein that precludes dimerization and ultimately 24mer production; C_2 dimers are the basic building blocks of the nanocages. Circular dichroism studies of the MIC1 protein showed that indeed the monomer already exists in an α-helical state, with little helicity gained in the transition from monomeric MIC1 to Cu-cage MIC1. The binding of metal ions to MIC1 monomers imparts no additional helicity to them, thereby refuting the hypothesis that Cu^{II} in particular pre-organizes the protein for a dimerization event; this finding also corroborates the idea that Cu^{II} is a template for the C_2 dimer. Chemical and thermal denaturation titrations showed that the relatively unstable MIC1 monomer could be substantially stabilized (by 30 kJ/mol) in the cage form, and that the presence of Cu in the MIC1 cage contributed little to its overall stability, despite the fact that the metal ion is essential to the formation of the 24mer oligomerization state. This finding again suggests that the polar interactions that were replaced by Cu coordination may primarily guide the cage assembly process of the HuHF system without providing a significant thermodynamic driving force.

Imparting chemical control over the monomer-to-cage transition of MIC1 through a metal-binding event provides a handle to better exploit the HuHF system in materials applications. The scope of potential guest molecules is no longer restricted to species that can passively diffuse into the cage interior, or that might be trapped in a stoichiometrically-uncontrollable fashion through the pH-driven disassembly/reassembly strategy that precludes most methodologies for chemical modifications of proteins. Having access to MIC1 monomers, at neutral pH, directly allows for a means of accessing the ferritin core with a new host of substrates. To demonstrate the utility of metal-directed protein self-assembly with the MIC1 protein, monomers were modified with a dansyl guest, and Cu^{II} binding was utilized to trigger 24mer formation and thus encapsulation of the AEDANS substrate. The relatively facile crystallization of MIC1 was employed to access the crystal structure of the trapped dansyl moiety. It is foreseeable to use the same strategy to access the crystal structures of other guest molecules, including perhaps crystallographically recalcitrant species. Beyond crystallography, monomer-to-cage conversion driven by metal binding has the potential to enhance the scope of actively encapsulated guests for applications in biosensor development, catalysis, drug delivery, and synthesis (applications to which ferritin has already been employed).

It is envisioned that the top-down approach of protein-protein interface redesign through rMeTIR might be translated into other systems. The basic requirement for success is that the system contains a symmetry-related interface amenable to mutagenic engineering. The rMeTIR strategy could be used to flesh out enhanced understandings of a variety of subcellular systems and processes, with the ultimate goal of being able to control them for applications purposes.

Future Directions of Research

Probing the assembly mechanism of HuHF. The self-assembly mechanism of ferritin has been debated in the literature for decades.[1] The canonical consensus has been that the basic building block of ferritin nanocages is the C_2 dimer. This dimer is postulated to form following the correct folding of the monomeric species into a stable, four-helix bundle subunit: $24M_1 \rightarrow 24\mathrm{M}_1 \rightarrow \mathrm{nM}_1 + \mathrm{mM}_2$.[2, 3] (Here, M_1 and M_1 refer to the unfolded and folded monomers, respectively, subscripts refer to the number of subunits in an intermediate, and n and m are integers whose sum totals 24.) Beyond dimerization, the order of oligomerization is debated, with trimer (M_3) or tetramer (M_4) pathways being favored. We were able to show, with circular dichroism studies of the HuHF variant MIC1, that monomeric MIC1 exists in a fully-folded four-helix bundle state, and it is from this state (M_1) that dimerization events proceed, in this case through $\mathrm{Cu}^{\mathrm{II}}$ binding. These findings invalidate the proposed $24M_1 \rightarrow 24\mathrm{M}_1$ pathway, which was formulated without a means of accessing monomeric ferritin under conditions that uncouple monomer folding from self-assembly.

We wish to move beyond this first step of the assembly mechanism, the dimerization event, and explore the route to which ferritin nanocages form. One hope was to crystallographically isolate and characterize discrete intermediates in the assembly pathway. To this end, MIC1 and other non-self-associating variants reacted with various metal ions have been employed. Yet, to date, only fully oligomerized 24mers have been observed crystallographically. One means to combat the favoring of cages in the crystalline state might be to remove the K86Q[4] mutation, whose utility has proved requisite in the structures obtained thus far of HuHF variants.

Solution-state experiments offer another avenue with which to characterize intermediates formed during the self-assembly process of ferritin monomer-to-cage formation. Typically, as in the case of the MIC1 system, the only discernable oligomerization states include monomer, dimer, and 24mer. Aside from the use of site-directed mutagenesis to access some of the other assembly products, such as trimer or tetramer, we have attempted to use Pd^{II} to kinetically trap intermediate species. Pd^{II} favors the square planar geometry that allows Cu^{II} to properly organize MIC1 into nanocages, and is thus expected to eventually facilitate cage formation. However, reactions with Pd^{II} are kinetically slow, and we hypothesized that perhaps discrete intermediates might be isolable in the assembly process using MIC1 and this metal ion. Initial experiments involving reactions of Pd^{II} with MIC1 have highlighted the monomer-to-dimer transition, and in some cases show an indiscrete smear of reaction products (Figure 5.1). Work is being done to optimize the reaction towards the goal of characterizing intermediate oligomerization states of higher order than dimer.

Toward the goal of understanding the self-assembly process of ferritin nanocage formation, we have also employed mutagenic screening studies. In particular, it was noted that in essentially all crystal structures obtained (in our hands) of HuHF variants, metal ions were found to be bound to the same sites at the C_3 and C_4 symmetry interfaces (Figure 5.2). At the C_3 pore, Ca^{II} is always found to bind three sets of residues D131 and E134. In the C_4 interface, metal ions such as Cu^{II}

bind the four interfacial H173 residues that are, in the apo-form, within H-bonding distance from one another. We hypothesized that these metal-binding events might play a role in the organization of these interfaces, just as Cu^{II} directs the C_2 dimerization of MIC1. Variants were prepared with elimination mutations D131A/E134A and H173A on the MIC1 template, and the resulting mutants were examined for their assembly properties.

Removal of the C_3 metal chelating residues D131 and E134 with alanine substitution on the MIC1 scaffold yielded a mutant that, like its parent protein, was expressed in inclusion bodies. The majority of this variant, upon isolation and renaturation, existed in a soluble aggregate state, as opposed to the case of MIC1, whose pure fraction was minimally comprised of such aggregates (Figure 5.3 A). Isolated monomers of $^{A131/134}$MIC1, while being lower in yield, proved capable of monomer-to-cage conversion upon exchange into a Cu^{II}-containing buffer (Figure 5.3 B). Thus, MIC1 metal responsiveness is preserved despite the loss of ability to bind metals at the C_3 pore. Based upon the propensity of this variant toward aggregation upon isolation, one might conclude that residues D131 and E134 (which participate in the enzymatic function of ferritin)[5] act to solubilize/stabilize the MIC1 monomer, but play no role in the oligomerization process of 24mer cage formation.

Contrastingly, metal-binding residue H173 at the C_4 interface of HuHF appears to have a degree of importance in the cage assembly process. In the absence of metal ions, H173 is capable of hydrogen bonding with its neighboring self at the C_4 pore. In our hands, most HuHF variant crystal structures obtained show this residue bound to metal ions such as Cu^{II}, with all four interfacial subunits donating an H173 residue for chelation. The mutation H173A on the MIC1 scaffold yielded variant protein that is expressed in inclusion bodies. Approximately half of the protein exists as a soluble aggregate, which is intermediate between results obtained for MIC1 and $^{A131/134}$MIC1 (Figure 5.4 A). Cu^{II}-driven monomer-to-cage turnover assays indicate that, at the concentration typically tested (100 μM), ^{A173}MIC1 is incapable of ferritin cage formation as determined by size exclusion chromatography. However, upon sample concentration (to prepare samples for sedimentation velocity measurements) the Cu-reacted lower-level oligomers self-assembled into 24mers (Figure 5.4 B). (This concentration-dependent oligomerization was seen before in the case of isolated Zn^{II}-MIC1 dimers.) Applying the H173A mutation to the 4His-ΔC* scaffold resulted in a variant that purifies as a nanocage in the absence of metal ions.

In the context of MIC1, H173 appears to play a role in cage self-assembly, either through means of hydrogen bond formation at the C_4 pore, or through metal-binding interactions, such as with Cu^{II}. Whether this residue (or the C_4 interface itself) is critical for 24mer formation has yet to be determined. The H173A mutation appears to attenuate oligomerization post Cu^{II}-reaction in a concentration-dependent manner, as seen with solution studies. Crystallographically, it was also confirmed that ^{A173}MIC1 is capable of forming 24mers in the solid state with a 1.95 Å crystal structure (see Table 5.1 for refinement statistics), again in the presence of Cu^{II} (Figure 5.5 A). TEM imaging also corroborates the solid-state cage nature of the ^{A173}MIC1 variant (Figure 5.5 B). Other mutagenic studies are currently underway to further explore residue-specific contributions to cage formation, with the ultimate goal of better understanding the self-assembly mechanism of ferritin and possibly constructing a fully reversible cage system.

Advancing MIC1 and Cu^{II}-induced cage formation in the realm of crystallography applications. The functional utility of harnessing chemical control over the self-assembly process of HuHF was demonstrated previously by the active encapsulation and crystallographic characterization of a dansyl moiety within the cage of the ^{C53}MIC1 variant driven by Cu binding. We wish to expand upon this new method of active guest encapsulation, in particular for the purposes of pushing the MIC1 system toward the characterization of other new, possibly more crystallographically-recalcitrant substrates. The primary strategy for variant modification takes advantage of cysteine chemistry. There are a host of thiol-reactive substrates available with which to decorate the MIC1 proteins, and many examples in the literature of thiol-mediated cage-like protein decoration[6-9]. The ^{C53}MIC1 variant, along with HuHF mutants containing either the H57C, H136C, or K143C mutations are being focused on. Residues at position 53 and its named alternatives face inward toward the interior of the ferritin nanocage (Figure 5.6), and, when modified, should allow for guest encapsulation without substrate projection into the C_2 interface, the result of which could prohibit Cu^{II}-initiated dimerization and cage formation events.

Dansyl modification of the ^{C53}MIC1 template and its subsequent crystallization demonstrated that the relative ease of HuHF crystallization could be exploited to access the crystal structures of ferritin guests. We are continuing this effort of small-molecule crystallization within MIC1 variant cages, with substrates such as hemin (ferriprotoporphyrin IX). Figure 5.7 shows that the scaffold ^{C53}MIC1 has been modified with hemin chloride; protein crystal “hits” have already been identified for this decorated protein, and are actively being screened for diffraction quality. Interestingly, placing hemin near the C_2 interface of HuHF would produce a modified protein reminiscent of bacterioferritin, which contains a heme group actually within its dimer interface.[10]

Aside from exploring the capacity of the MIC1 system to characterize the structures of small-molecule guests, we are interested in interrogating the structural nature of more challenging, crystallographically recalcitrant substrates. I am particularly interested in peptidic targets that fall into two categories: amyloid peptides[11] and peptides that mimic metalloprotein active sites. An example of an amyloid peptide that I am pursuing the crystallographic characterization of is amyloid-β (Aβ), popularized for its implications in Alzheimer's disease.[12, 13] The structure of this peptide has proved canonically elusive, although there exist several solution-state (NMR)[14-17] and crystal structures[18] of various fragments of the peptide. We are attempting encapsulation of either full-length (1-42) or peptidic fragments of Aβ within the MIC1 scaffold with the goal of ascertaining solid-state structural information. One consequence of crystallizing small segments of Aβ will be the attained ability to directly compare known solution-state structures of the peptidic fragments (such as 1-28 and 25-35) with our crystal structures. This will provide a means of possibly validating our technique of structural characterization.

Beyond amyloidogenic peptides, we are interested in probing the structural nature of peptides that have been engineered to mimic the relevant metal-binding sites of metalloenzymes, especially Cu-metalloproteins. Examples of such peptides come from the lab of DeRose, where hemocyanin- and plastocyanin-based peptides have been prepared that bind Cu.[19, 20] In the case of the playstocyanin model, redox activity has even been conferred upon the peptide. Since Cu^{II}-binding initiates cage formation of the MIC1 proteins, incorporating one of these metalloenzyme model peptides as a guest within the nanocage could result in accessing the desired Cu-bound form of the substrates. Available knowledge about the Cu-binding nature of these peptides (obtained through spectroscopic or other measurements) can corroborate our findings and again validate the utility of the MIC1 system for crystallographic characterization applications.

The primary method for MIC1 variant modification relies upon cysteine chemistry, which we showed could, in a stoichiometrically-controlled fashion, be employed to incorporate a specific number of guest molecules into the ferritin core with the dansyl-^{C53}MIC1 setup. A host of small-molecules that are thiol-reactive can be purchased that either coordinate cysteine themselves (like hemin), or react in a covalent manner through iodine replacement (as with IAEDANS) or maleimide reactions with cysteine. In an effort to modify MIC1 proteins with peptides including those mentioned above, we are exploring the possible modification of the peptides to present an iodide leaving group or maleimide moiety with which to interact with the engineered cysteine residues. Alternatively, linkers providing two reactive maleimide functionalities, such as N,N'-(1,3-phenylene)dimaleimide, are being employed to modify the surface of cysteine-containing MIC1 variants with peptidic targets. Initial trials with this short, relatively rigid bismaleimide linker and ^{C53}MIC1 have indicated that the protein couples with the linker, which is subsequently hydrolyzed prior to further reaction with targets. The system is currently being optimized to mitigate hydrolysis products.

Encapsulation of gadolinium chelates for the preparation of MRI contrast agents. The literature is rife with examples of employing ferritin as a tool for magnetic resonance imaging applications. The natural, stored substrates of the enzyme can themselves act to provide MRI contrast.[21, 22] Alternatively, contrast agents with greatly enhanced relaxivities, including and especially gadolinium chelates, have been incorporated into the ferritin nanocage core, capitalizing on the canonical pH-driven encapsulation technique.[23, 24] Despite the high relaxivity values attained in this way, the gadolinium chelates themselves remain free to rotate within the 24mer interior. If the chelates could be affixed to the inner MIC1 cage protein surface, we hypothesize that even greater MRI contrast agent properties[25, 26] might be achieved, as observed in the case of enhanced relaxivity occurring from the binding of a gadolinium^{III}-containing complex to the surface of human serum albumin.[27]

Cu^{II}-responsive MIC1 self-assembly provides an avenue with which to sequester gadolinium chelates anchored to the interior surface of ferritin nanocages. Maleimide-functionalized versions of DOTA and DTPA (shown in Figure 5.8 with Gd^{III} bound) are, for example, commercially available (Macrocyclics). We are exploring the modification of cysteine-engineered MIC1 variants with these gadolinium chelates to prepared advanced MRI contrast agents. The substantive surface space of the cage interior provides for the possibility of incorporating 24n (n being the number of of cysteine mutations) chelates in a stoichiometrically controlled manner, which affords the possibility of greater sample loading and contrast agent property enhancement.

One control experiment that should be performed prior to attempting gadolinium complex encapsulation is to show that MIC1 cages can form with appended guest substrates upon Cu^{II} binding, in solution. Practical applications of the MIC1 system in the realm of MRI contrast agent development, for example, require that cage formation be possible following monomer modification. The protein crystal structure of AEDANS-^{C53}MIC1 indicates that modified MIC1 monomers are capable of nanocage formation in the solid state, thereby trapping the bound dansyl moiety within. However, we have yet to show that this is the case in solution, and efforts are currently underway to demonstrate this capability.

Metal-mediated control of the oligomerization state of the HuHF variant MIC1 affords the opportunity to exploit the cage-like ferritin protein for materials applications. The MIC1 system has proved its utility in the realm of crystallography, where the ^{C53}MIC1 scaffold was employed to access the crystal structure of a small-molecule guest within the 24mer cage. We are taking steps to expand upon this result to obtain the crystal structures of other guest molecules, with the hopes of eventually gaining insight into the structural nature of challenging targets like the Aβ peptide (and related fragments) and metalloenzyme peptide mimics. We are also capitalizing on the monomer-to-cage conversion, driven by Cu^{II} binding, to actively encapsulate bound gadolinium chelate complexes to prepare enhanced MRI contrast agents. These are a handful of possible applications of the MIC1 system, with other realms including catalysis and drug delivery yet to be broached.

Materials and Methods

Protein expression, purification and characterization. Proteins were expressed, as above, in *E. coli* BL21 (DE3) cells, with expression initiated by IPTG induction. Following cell lysis, proteins were obtained from inclusion body pellets, which required solubilization prior to protein purification. Variants were then purified via metal-affinity and size-exclusion chromatographies using an FPLC, with the protocol previously outlined. In the case of cysteine-containing variants such as ^{C53}MIC1, the reducing agent DTT was employed to prevent random oligomerization of monomers, and was kept present in the protein solution except when inconvenient (as in during metal-affinity purification and modification reactions). Protein purity and veracity were determined through SDS-PAGE gel electrophoresis MALDI-TOF mass spectrometry analyses, respectively.

Metal-Mediated self-assembly of MIC1 variants. Purified, monomeric MIC1 variants were concentrated to 100 μM in 15 mM Tris containing 150 mM NaCl and buffered at pH 7.4 (standard buffer); the buffer was supplemented with 10 mM EDTA.

7-mL portions of the protein stock solutions were dialyzed against 2 x 5 L of solutions containing equimolar $CuCl_2$ prepared in the standard buffer. Dialysis proceeded for a total of 40 hours at 4 °C. Following dialysis, the metal-reacted protein samples were centrifuged for 10 minutes at a speed of 10,000 rpm at 4 °C to remove precipitated protein. Metal-mediated assemblies were then characterized with size-exclusion chromatography and sedimentation velocity analysis.

In the case of Pd^{II} reactions, it was not feasible to dialyze against such large volumes of Pd-containing buffer to attempt monomer-to-cage formation with MIC1. Instead, $Pd(NO_3)_2$ was added directly to the MIC1 protein (in the standard buffer) at 1:1 or 2:1 Pd^{II} ion/MIC1 monomer ratios. The reaction volumes were each 500 μL, with a MIC1 protein concentration of 45 μM as determined by the Bradford assay. Reactions proceeded for three days at either room temperature or 37 °C. Immediately prior to performing sedimentation velocity measurements on the reaction products, the protein solutions were centrifuged at 12,000 rpm for 10 minutes at 4 °C.

Analytical ultracentrifugation. Sedimentation velocity experiments were performed as previously described. In brief, measurements were taken on a Beckman-Optima XL-I Analytical Ultracentrifuge equipped with an An-60 Ti rotor. Protein samples were prepared in the standard buffer; in the case of metal-free experimental conditions, 10 mM EDTA was included in the buffer solution. Protein concentrations were typically set to 50 μM, except when performing runs on the MIC1-Pd^{II} reactions where the concentration of protein was 45 μM. The wavelength used for sample detection was 280 nm, and the instrument was operated at 41,000 rpm with the temperature maintained at 25 °C for the experimental duration.

Sedimentation velocity data were processed using the program SEDFIT[28] as before, with implementation of a continuous c(s) model fit. Key buffer properties were calculated (with standardization at 25 °C) with SEDNTERP, available for free at http://www.jphilo.mailway.com. MIC1 and variant partial specific volumes, as well as oligomer theoretical sedimentation coefficients, were calculated with HYDROPRO.[29]

X-ray crystallography. Protein crystals of Cu-bound A173MIC1 were obtained by the sitting-drop vapor diffusion method. The sitting drops yielding diffraction-quality crystals consisted of 2 μL of protein solution and 2 μL of precipitant solution. The wells contained 500 μL of precipitant solution. The protein solution was made of 668 μM of ^{A173}MIC1 protein in the standard buffer. The precipitant consisted of 50 mM Tris buffered at pH 8.0, with 10 mM $CaCl_2$ and 700 μM $CuCl_2$. The precipitant also contained 8% (by weight) PEG 1900 MME. The protein crystals grew at room temperature within a one-month period. For cryoprotection, ~1 μL of glycerol was added directly to the 4-μL well solution containing crystals, and the crystals were pulled through this glycerol layer and immediately submerged and frozen in liquid N_2.

X-ray diffraction data were collected at 100 K at Beamline 9-2 of the SSRL facility using 0.98-Å radiation. Diffraction data were processed using MOSFLM and SCALA.[30] The protein crystal structure was solved with molecular replacement by MOLREP[31] with the structure of HuHF mutant K86Q[4] (PDB ID: 2CEI) used as the model. Rigid-body, positional and thermal refinement was carried out using REFMAC,[32] along with iterative manual model building with COOT.[33] Atomic coordinates and structure factors have not yet been deposited into the Protein Data Bank. All structural figures were produced using PYMOL.[34]

Transmission electron microscopy imaging. The propensity of ^{A173}MIC1 to assemble into ferritin nanocages in the presence of Cu^{II} at elevated protein concentrations was corroborated with TEM imaging. Samples of ^{A173}MIC1 previously reacted with $CuCl_2$ at 100 μM (normal self-assembly assay conditions) were concentrated such that the final protein concentration was 600 μM in the standard buffer. After overnight incubation at 4 °C, the protein specimens were diluted to 5 μM with standard buffer for imaging. Having been concentrated post-Cu^{II}-reaction, the protein appears as nanocages in the TEM micrographs. This result mirrors sedimentation velocity data suggesting that small oligomers of Cu^{II}-treated ^{A173}MIC1 isolated with size-exclusion chromatography can, upon concentration (enacted when preparing samples for SV measurements) form nanocages.

Copper-coated carbon grids were glow discharged for ~1 minute in an Emitech K350 evaporation unit, immediately followed by deposition of 3 μL aliquots of protein samples onto the grids. After an incubation span of 1 minute, the grids were washed with double-distilled water, and the excess solution was wicked away. The samples were then stained twice with 3 μL of a 1% uranyl acetate solution. After drying, the grids were imaged on an FEI Sphera transmission electron microscope equipped with an LaB_6 electron gun operating at 200 keV. Objective lens underfocus settings ranging from 400-800 nm on a Gatan $2K^2$ CCD were employed. Analysis of the resulting TEM micrographs was carried out with Image J, freeware made available through the National Institutes of Health, USA.

Modification of cysteine-containing MIC1 variants. The strategy employed to modify cysteine residues engineered onto the interior surface of HuHF cages, such as C53, is elaborated here in a generalized format. Cysteine-containing protein in the standard buffer supplemented with 10 mM EDTA and at least 1 mM fresh DTT (to ensure monomeric starting material) was degassed and brought into an anaerobic environment. (In all cases, the protein utilized did not have soluble aggregates removed prior to modification.) Small quantities of the protein (~10 mL) were then dialyzed against 2 L of degassed EDTA-containing standard buffer to remove the DTT reducing agent. The protein samples, typically in concentrations ranging from 10-50 μM, were next reacted with an excess of modifier. For example, in the case of modification of ^{C53}MIC1 with hemin chloride (Strem Chemicals), a 162-fold excess of the small molecule was used with respect to ferritin monomer concentration. Reaction mixtures stirred for at least an hour (in darkness when necessary) while remaining in an anaerobic state. Free, unreacted modifier was removed first by exhaustive dialysis against the standard buffer containing 10 mM EDTA, and then by buffer exchange, using the same EDTA-treated standard buffer as eluent, with an Econo-Pac 10DG Desalting Column. Modified protein was then subjected to size-exclusion chromatography, to remove soluble aggregates, and characterized by MALDI-TOF mass spectrometry to UV-VIS absorbance measurements to ensure veracity and extent of modification.

Chapter 5 presents materials that this author significantly contributed to as a researcher, with contributions from K. M. Kane and F. A. Tezcan. The subject matter has not yet been organized for publication.

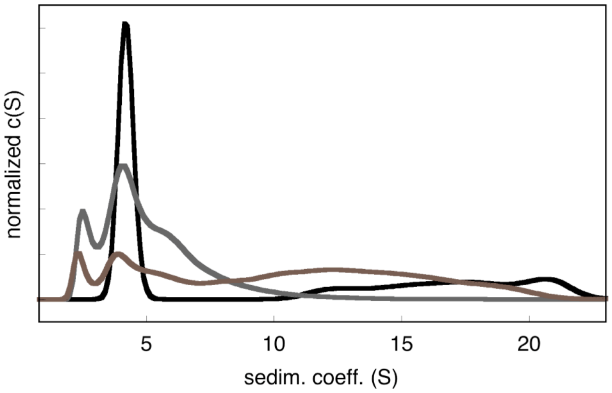

Figure 5.1. Characterization of solution-state reaction products of Pd^{II} with MIC1 by sedimentation velocity measurements. MIC1 protein was allowed to react with $Pd(NO_3)_2$ for three days prior to SV experiments being performed. The black trace corresponds to 1:1 Pd^{II}/MIC1 reaction ratios, with the monomeric protein concentration set at 45 μM and the reaction temperature ~25 °C (room temperature). A majority of the protein exists in the dimer state, with heavier oligomerization species also being populated. The charcoal-colored trace represents similar reaction conditions, performed this time with a ratio of 2:1 Pd^{II}/MIC1. Monomer, dimer, and other intermediate species are present. The brown trace corresponds to the same 2:1 reaction, having been incubated at 37 °C rather than room temperature. The elevated temperature appears to enhance population of larger oligomers, but in an indiscreet manner.

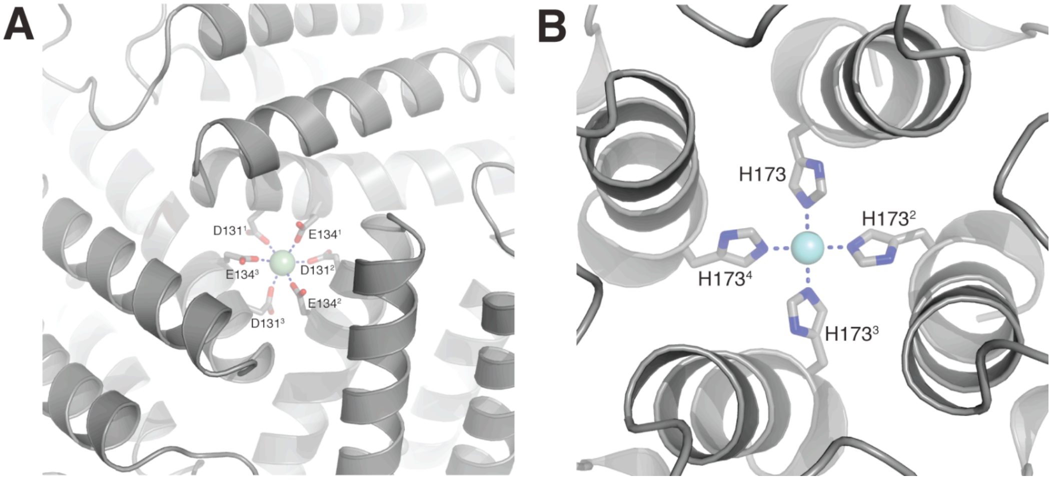

Figure 5.2. Alternative metal-binding positions commonly found populated with metal ions in protein crystal structures of HuHF variants. A) Close-up view of the C_3 interface pore, where three sets of residues D131 and E134 bind a Ca^{II} ion (pale green sphere), as indicated by blue dashes. B) Zoomed-in view down the C_4 symmetry interface highlighting Cu^{II} binding (represented by blue dashes) to four H173 residues. The Cu^{II} ion is shown as an aquamarine sphere. The Cu-MIC1 structure (PDB ID: 4DYY) was used here for figure preparation.

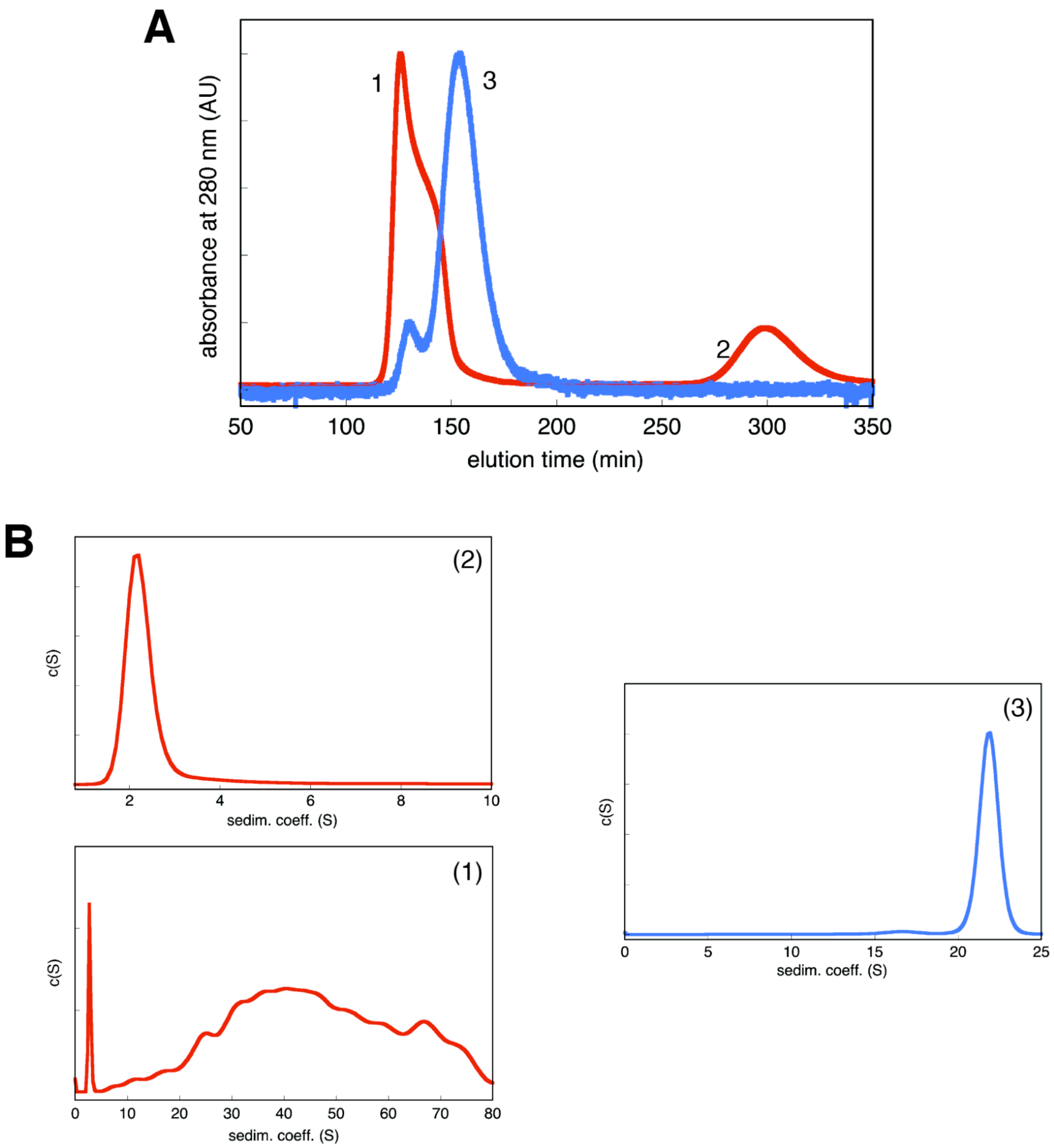

Figure 5.3. Hydrodynamic characterization of C$_3$-interface variant $^{A131/134}$MIC1 and its capacity to undergo the Cu^{II}-induced monomer-to-cage transition. A) Size-exclusion chromatogram overlay showing the solution state of the C$_3$ variant as isolated and under metal-free conditions (red trace) and after being reacted with Cu^{II} (blue trace). B) Sedimentation velocity characterization of size-exclusion elution peaks from (A). In the as-isolated, metal-free form, the protein exists as a mixture of soluble aggregates (peak 1) and monomers (peak 2). Following treatment with Cu^{II}, the protein is converted into ferritin nanocages, just as in the case of MIC1 (peak 3).

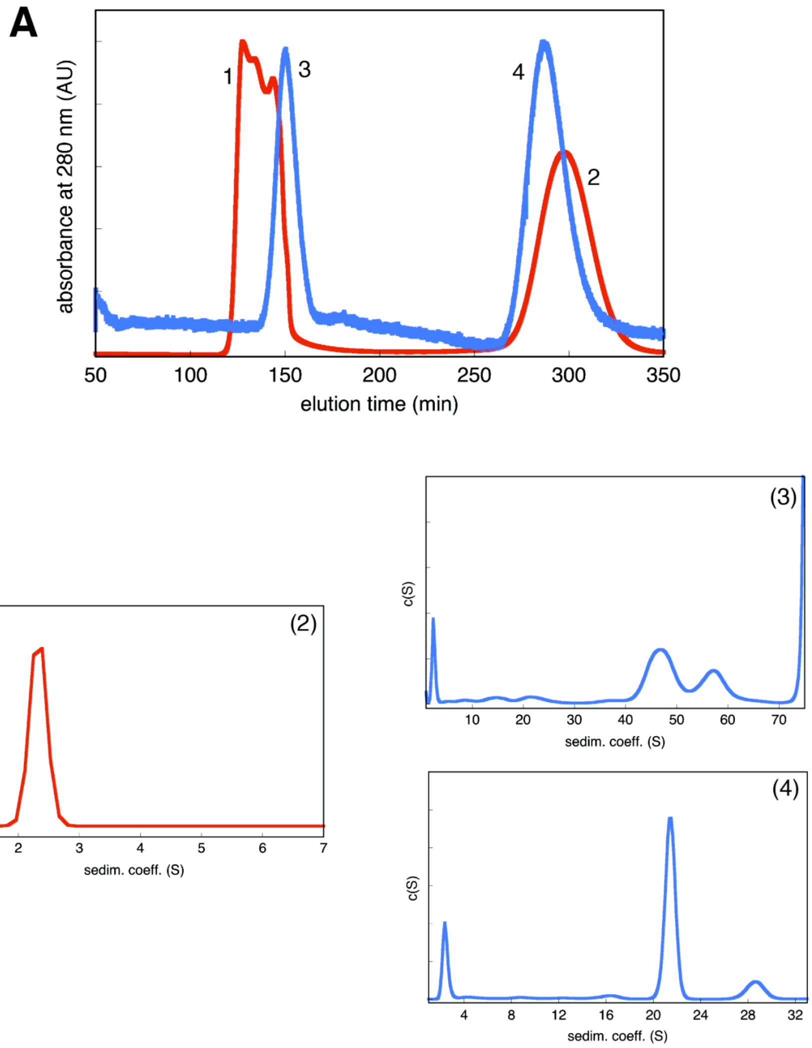

Figure 5.4. Solution-state characterization of C_4-interface variant ^{A173}MIC1 and its propensity toward Cu^{II}-induced 24mer formation. A) Size-exclusion chromatogram overlay depicting the oligomerization state of ^{A173}MIC1 in its as-isolated, metal-free form (red trace, peaks 1 and 2), and solution states following reaction of the protein with Cu^{II} (blue trace, peaks 3 and 4). B) Sedimentation velocity characterization of size-exclusion elution peaks of various states of ^{A173}MIC1. In its as-isolated form under metal-free conditions, the protein exists as a mixture of soluble aggregates (peak 1) and monomers (peak 2). Reacting monomers of this variant with Cu^{II} to test monomer-to-cage conversion capability yields a mixture of soluble aggregates (peak 3) and monomers and dimers (peak 4); the latter two species are able to generate cages upon concentration to prepare the sedimentation velocity experiment samples.

Table 5.1. X-ray data collection and refinement statistics for the protein crystal structure of Cu-^{A173}MIC1. * denotes highest resolution shell.

	Cu-^{A173}MIC1
Data Collection Location	SSRL BL 9-2
Unit Cell Dimensions	a = b = c = 179.7 Å
	$\alpha = \beta = \gamma = 90°$
Symmetry Group	F432
Resolution (Å)	63.55-1.95
X-Ray Wavelength (Å)	0.98
Number of Unique Reflections	18682
Redundancy	41.2
Completeness (%)*	99.9 (99.9)
$\langle I/\sigma I \rangle$*	4.9 (1.4)
R_{symm} (%)*	12.5 (47.9)
R_{work} (%)*	17.9 (21.6)
R_{free} (%)*	21.7 (27.7)
Number of Atoms	
Protein (including alternative side chain conformations)	1452
Ligands/Ions	17
Water	86
B-Factors (Å^2)	
Protein	13.2
Ligands/Ions	50.8
Water	17.5
RMS Deviations	
Bond Lengths (Å)	0.024
Bond Angles (^{o})	1.781
Ramachandran plot (%)	
Residues in favored regions	97.0
Residues in allowed regions	1.8
Residues in generously allowed regions	0.0
Residues in disallowed regions	1.2

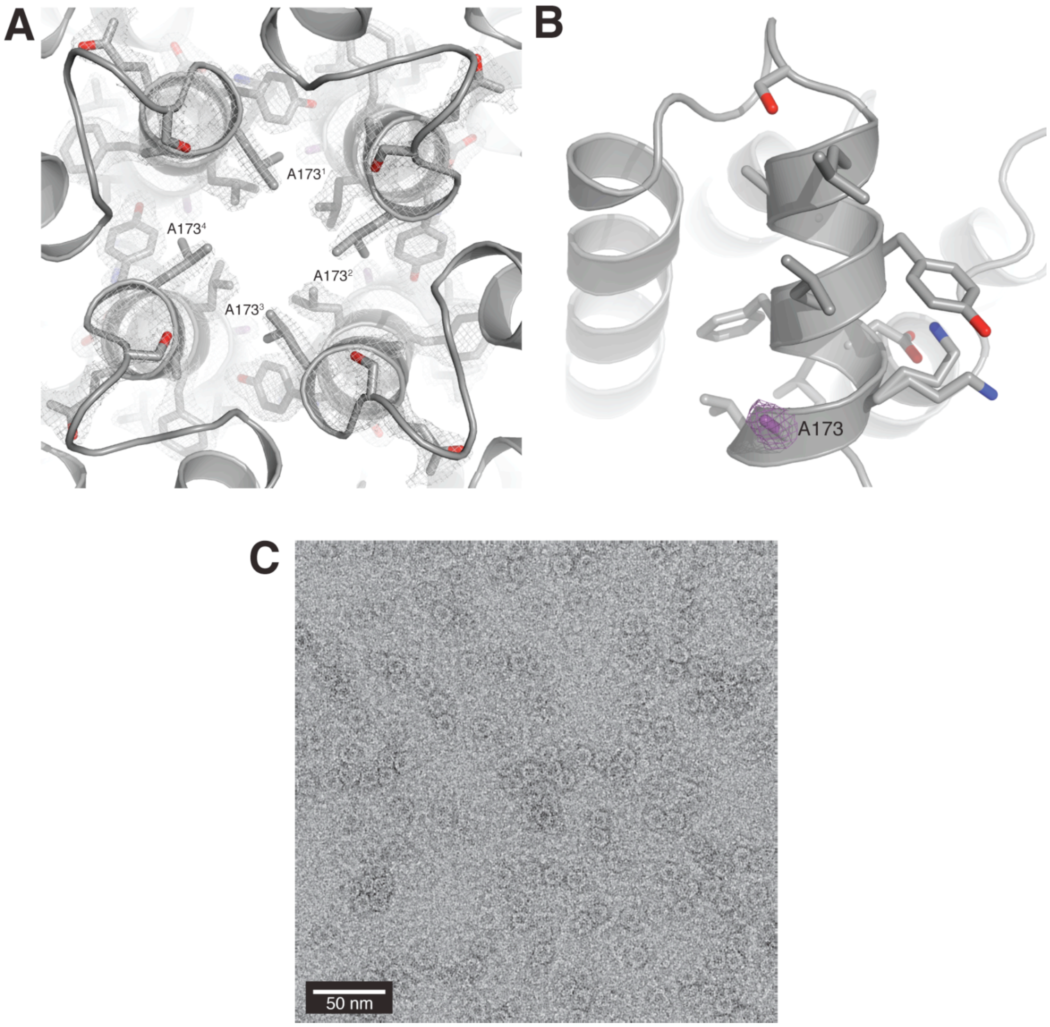

Figure 5.5. Solid-state characterization of C_4-interface variant ^{A173}MIC1 in its Cu^{II}-reacted form through protein crystallography and TEM imaging. A) Close-up view looking down the C_4 pore of ^{A173}MIC1, highlighting electron density ascribed to the region. The $2F_o$-F_c electron density map is contoured at 1.6 σ (gray mesh), with mutated residue A173 named and indicated with violet-purple coloration. B) Zoomed-in view of the short C_4-interface helix (in the context of a protein monomer) on which A173 resides, highlighting the mutated residue. The $2F_o$-F_c electron density map corresponding to A173 is shown as a violet-purple mesh contoured at 1.6 σ. C) Negatively stained TEM image of the ferritin nanocages formed by A173 following reaction with Cu^{II} and concentration to 600 μM; protein was diluted to 5 μM immediately prior to imaging.

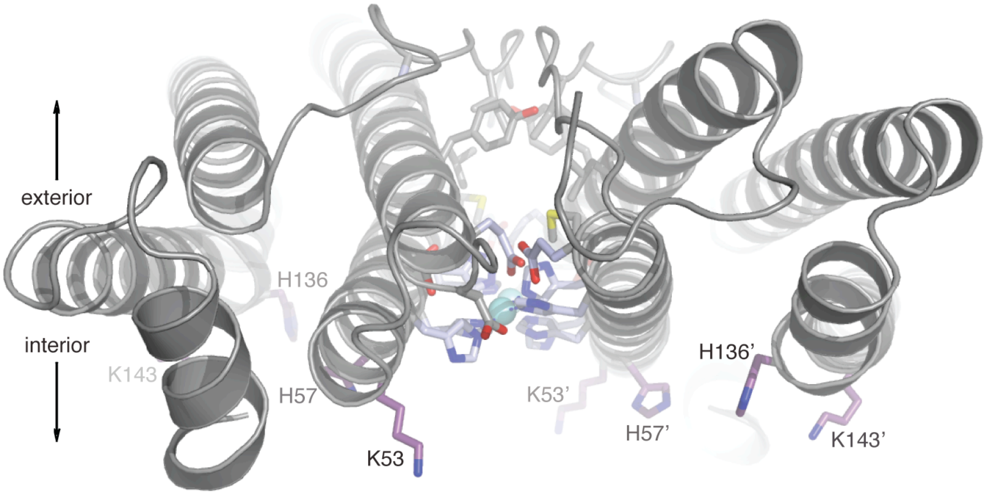

Figure 5.6. Proposed sites of mutagenic cysteine placement on the interior surface of the MIC1 HuHF variant nanocage. Aside from the K53C mutation on MIC1, which has been crystallographically characterized (with a dansyl modification, PDB ID: 4DZ0), residues H57, H136, and K143 have been targeted for cysteine engineering. These residues are highlighted above in violet-purple, and shown in the context of the C_2 dimer of MIC1 with copper bound (4His clamps in silver-blue, Cu^{II} as aquamarine sphere).

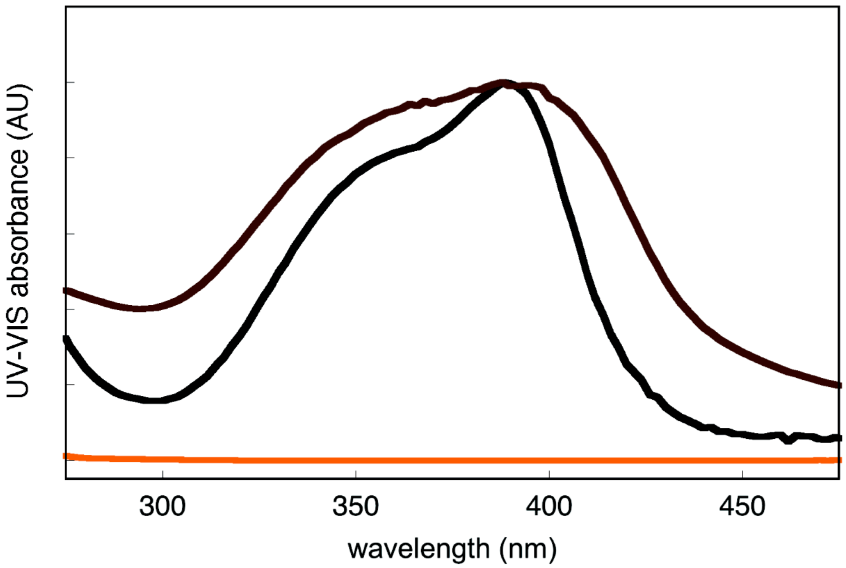

Figure 5.7. Spectroscopic characterization of the modification product resulting from the reaction of the ^{C53}MIC1 variant of HuHF with hemin chloride. The modification reaction proceeded in the standard buffer (15 mM Tris buffered at pH 7.4 and including 150 mM NaCl) supplemented with 10 mM EDTA. The spectroscopic signature of the reaction buffer is given as the orange trace. Free hemin chloride in the reaction buffer is shown by the black trace. Upon protein modification (purportedly at residue C53), the absorbance spectra of bound hemin broadens to that indicated by the brown trace.

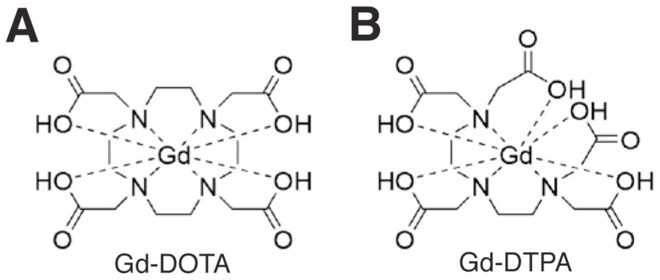

Figure 5.8. Chemical structures of Gd^{III}-based chelate complexes utilized commonly as MRI contrast agents. Both are commercially available with monopodal maleimide functionalization. A) Gd-DOTA complex. B) Gd-DTPA chelate complex. (Both figures are reproduced from reference 24.)

References

1. Stefanini, S., P. Vecchini, and E. Chiancone, *On the Mechanism of Horse Spleen Apoferritin Assembly - a Sedimentation-Velocity and Circular-Dichroism Study.* Biochemistry, 1987. **26**(7): p. 1831-1837.

2. Gerl, M., et al., *Self-Assembly of Apoferritin from Horse Spleen after Reversible Chemical Modification with 2,3-Dimethylmaleic Anhydride.* Biochemistry, 1988. **27**(11): p. 4089-4096.

3. Jaenicke, R., *Protein Folding and Protein Association.* Angewandte Chemie International Edition in English, 1984. **23**(6): p. 395-413.

4. Lawson, D.M., et al., *Solving the Structure of Human H-Ferritin by Genetically Engineering Intermolecular Crystal Contacts.* Nature, 1991. **349**(6309): p. 541-544.

5. Theil, E.C., *Ferritin protein nanocages use ion channels, catalytic sites, and nucleation channels to manage iron/oxygen chemistry.* Current Opinion in Chemical Biology, 2011. **15**(2): p. 304-311.

6. Flenniken, M.L., et al., *The Small Heat Shock Protein Cage from Methanococcus jannaschii Is a Versatile Nanoscale Platform for Genetic and Chemical Modification.* Nano Letters, 2003. **3**(11): p. 1573-1576.

7. Gillitzer, E., et al., *Chemical modification of a viral cage for multivalent presentation.* Chemical Communications, 2002(20): p. 2390-2391.

8. Santambrogio, P., et al., *Effects of modifications near the 2-, 3- and 4-fold symmetry axes an human ferritin renaturation.* Biochemical Journal, 1997. **322**: p. 461-468.

9. Wang, Q., et al., *Natural supramolecular building blocks. Cysteine-added mutants of cowpea mosaic virus.* Chemistry & Biology, 2002. **9**(7): p. 813-819.

10. Frolow, F., A.J. Kalb, and J. Yariv, *Structure of a unique twofold symmetric haem-binding site.* Nature Structural Biology, 1994. **1**(7): p. 453-460.

11. Harrison, R.S., et al., *Amyloid peptides and proteins in review.* Reviews of Physiology, Biochemistry & Pharmacology, 2007. **159**: p. 1-77.

12. Glenner, G.G., et al., *The amyloid deposits in Alzheimer's disease: their nature and pathogenesis.* Applied Pathology, 1984. **2**(6): p. 357-369.

13. Selkoe, D.J., *Alzheimer's disease: a central role for amyloid.* Journal of Neuropathology & Experimental Neurology, 1994. **53**(5): p. 438-447.

14. D'Ursi, A.M., et al., *Solution structure of amyloid beta-peptide (25-35) in different media.* Journal of Medicinal Chemistry, 2004. **47**(17): p. 4231-4238.

15. Kohno, T., et al., *Three-dimensional structures of the amyloid beta peptide (25-35) in membrane-mimicking environment.* Biochemistry, 1996. **35**(50): p. 16094-16104.

16. Poulsen, S.A., et al., *Solution structures in aqueous SDS micelles of two amyloid beta peptides of A beta(1-28) mutated at the alpha-secretase cleavage site (K16E, K16F).* Journal of Structural Biology, 2000. **130**(2-3): p. 142-152.

17. Watson, A.A., D.P. Fairlie, and D.J. Craik, *Solution structure of methionine-oxidized amyloid beta-peptide (1-40). Does oxidation affect conformational switching?* Biochemistry, 1998. **37**(37): p. 12700-12706.

18. Colletier, J.P., et al., *Molecular basis for amyloid-beta polymorphism.* Proceedings of the National Academy of Sciences of the United States of America, 2011. **108**(41): p. 16938-16943.

19. Rockcliffe, D.A., et al., *De novo design and spectroscopic characterization of a dinucleating copper-binding pentadecapeptide.* Inorganic Chemistry, 2006. **45**(2): p. 472-474.

20. Daugherty, R.G., et al., *Design and spectroscopic characterization of peptide models for the plastocyanin copper-binding loop.* Inorganic Chemistry, 2002. **41**(10): p. 2623-2632.

21. Cohen, B., et al., *Ferritin as an Endogenous MRI Reporter for Noninvasive Imaging of Gene Expression in C6 Glioma Tumors.* Neoplasia, 2005. **7**(2): p. 109-117.

22. Vymazal, J., et al., *T1 and T2 of ferritin at different field strengths: effect on MRI.* Magnetic Resonance in Medicine, 1992. **27**(2): p. 368-374.

23. Aime, S., L. Frullano, and S.G. Crich, *Compartmentalization of a gadolinium complex in the apoferritin cavity: A route to obtain high relaxivity contrast agents for magnetic resonance imaging.* Angewandte Chemie-International Edition, 2002. **41**(6): p. 1059-1061.

24. Makino, A., et al., *Effective encapsulation of a new cationic gadolinium chelate into apoferritin and its evaluation as an MRI contrast agent.* Nanomedicine: Nanotechnology, Biology, and Medicine, 2011. **7**: p. 638-646.

25. Caravan, P., et al., *Gadolinium(III) Chelates as MRI Contrast Agents: Structure, Dynamics, and Applications.* Chemical Reviews, 1999. **99**: p. 2293-2352.

26. Lauffer, R.B., *Paramagnetic Metal Complexes as Water Proton Relaxation Agents for NMR Imaging: Theory and Design.* Chemical Reviews, 1987. **87**: p. 901-927.

27. Aime, S., et al., *Towards MRI contrast agents of improved efficacy. NMR relaxometric investigations of the binding interaction to HSA of a novel heptadentate macrocyclic triphosphonate Gd(III)-complex.* Journal of Biological Inorganic Chemistry, 1997. **2**(4): p. 470-479.

28. Schuck, P., *A model for sedimentation in inhomogeneous media. I. Dynamic density gradients from sedimenting co-solutes.* Biophysical Chemistry, 2004. **108**(1-3): p. 187-200.

29. de la Torre, J.G., M.L. Huertas, and B. Carrasco, *Calculation of hydrodynamic properties of globular proteins from their atomic-level structure.* Biophysical Journal, 2000. **78**(2): p. 719-730.

30. Winn, M.D., et al., *Overview of the CCP4 suite and current developments.* Acta Crystallographica Section D-Biological Crystallography, 2011. **67**: p. 235-242.

31. Vagin, A. and A. Teplyakov, *MOLREP: an automated program for molecular replacement.* Journal of Applied Crystallography, 1997. **30**: p. 1022-1025.

32. Murshudov, G.N., A.A. Vagin, and E.J. Dodson, *Refinement of macromolecular structures by the maximum-likelihood method.* Acta Crystallographica Section D-Biological Crystallography, 1997. **53**: p. 240-255.

33. Emsley, P. and K. Cowtan, *Coot: model-building tools for molecular graphics.* Acta Crystallographica Section D-Biological Crystallography, 2004. **60**: p. 2126-2132.

34. DeLano, W.L., *The PYMOL Molecular Graphics System.* 2003.

Appendix

HuHF Variant Construction

DNA coding for wild-type HuHF was obtained directly from DNA 2.0 (Menlo Park, CA) on a pJexpress bacterial vector optimized for expression in *E. coli* cells. The amino acid residues, paired with their respective DNA codons, are given in Table A1.1. The primary structure of HuHF is recapitulated in Figure A1.1, with regions comprising the four α-helices A-D highlighted by color, as well as the sequence corresponding to the BC loop at the C_2 interface. All variants prepared in this dissertation stemmed from this initial, native HuHF plasmid.

The template protein onto which metal coordination motifs were to be grafted, as per the first phase of reverse metal-templated interface redesign, was the HuHF variant ΔC*.[1] This variant has all native cysteine residues replaced through site-directed mutagenesis so as to eliminate the possibility of random subunit associations due to disulfide bond formation; the substitutions include C90E, C102A, and C130A. It also contains the K86Q mutation[2] that facilitates the crystallization of HuHF and its variant forms. Table A1.2 summarizes the mutagenic primers employed in the preparation of the ΔC* mutant.

Following the construction of the template variant ΔC*, the first phase of rMeTIR was initiated by the grafting of 4His coordination motifs onto the surface of the C_2 interface of ΔC*. Two versions of the metal-binding motifs were prepared. One was engineered at the C_2 dimerization interface near the cage interior, and was comprised of native residue H60 and the mutations L56H, R63H, and E67H. This variant was termed 4His-ΔC*. The alternative coordination motif was installed on the BC loop portion of the C_2 symmetry interface, on the nanocage exterior. The mutations employed in its creation included F81H, Q83H, K87H, and D91H, and the mutant was named 4His-loop-ΔC*. The mutagenic primers utilized in the preparation of both metal-binding motif variants are given in Table A1.3.

The second phase of rMeTIR calls for the engineering of mutations at a protein-protein interface that perturb native PPIs, thereby disallowing them in the absence of a metal-binding event. The C_2 interface of the two HuHF variants bearing the 4His metal-coordination motif was screened with site-directed mutagenesis to find a ferritin mutant that was capable of self-assembly only in the presence of metal ions, particularly Cu^{II} ions, as the geometry of the 4His motif dictates. A variety of mutations were installed on the 4His-ΔC* and 4His-loop-ΔC* templates; the primers utilized to carry out these mutations are summarized in tabular form in Table A1.4. The result of the mutagenic screening process was the discovery of the MIC1 variant (4His-ΔC* containing mutations Y39E, N74E, and P88A), which demonstrated the greatest oligomeric response to Cu^{II} ions.

Variant MIC1, with its propensity toward metal-induced self-assembly, was employed toward active encapsulation endeavors through modification of the protein monomeric units. Modification efforts relied upon cysteine chemistry, and toward this end cysteine residues were installed on the inner surface of the ferritin nanocage that could be decorated with thiol-reactive substrates. Initially, position 53 was chosen for mutation, and it was shown crystallographically that ^{C53}MIC1 could be stoichiometrically labeled with a dansyl moiety. Alternate positions were also selected for cysteine installment, including 57, 136, and 143; all of these residues face inward toward the center of the HuHF cage. Table A1.5 provides the primers utilized in the installation of cysteine residues on the MIC1 template.

The HuHF variant MIC1 underwent additional site-directed mutagenesis with the goal of creating extra instability on the template protein. These mutagenic efforts served two purposes. Firstly, the 4His metal-coordination motif was targeted for mutagenesis, to determine whether MIC1 could self-assemble in the presence of Cu^{II} without an obvious site for the metal to bind to trigger oligomerization. Variants were prepared with native H60 substituted by an alanine residue, or with reversion of the installed histidine clamp residues on MIC1 to wild-type L56, R63, and E67. Secondly, C_3 and C_4 interfacial metal-binding residues were changed to alanines to probe the importance D131, E134, and H173 might have in MIC1 cage assembly. The primers used to incorporate the two sets of destabilizing mutations onto the MIC1 template are given in Table A1.6.

Structural Characterization of ^{D32}4His-ΔC* and ^{A60}MIC1 Variants

The second phase of rMeTIR involves the incorporation of instability into a protein-protein interface (accomplished through mutagenic screening) that results in the construction of a non-self-associating monomeric species. In the case of HuHF, mutations Y39E, N74E, and P88A on the 4His-ΔC* template yielded a monomeric ferritin variant only capable of forming the 24-meric ferritin nanocage in the presence of Cu^{II}. During the mutagenic screening process, a variety of muteins were prepared that did not quite satisfy the monomer-to-cage switch characteristic found in MIC1. Two of these variants, ^{D32}4His-ΔC* and ^{A60}MIC1, were crystallographically characterized.

The protein crystal structure of ^{D32}4His-ΔC* was determined at 2.30 Å resolution (refer to Table A2.1 for refinement statistics). Despite the fact that the crystals were grown in the presence of Zn^{II}, (see Table A2.2 for crystal growth conditions) opportunistic Cu is found coordinated to the 4His binding motifs in the structure (Figure A2.1); this is likely a purification artifact. The structure clearly shows residue D32 jutting into the inner C_2 interface space, which is primarily hydrophobic in nature. Overall, the rmsd between the 4His-ΔC* and ^{D32}4His-ΔC* C_2 dimer is 0.110 Å, as measured over all C_α positions. The instability incurred from engineering the Y32D mutation into the C_2 dimerization interface manifests in expression of the protein in inclusion bodies, and partial isolation of the protein in a monomeric state. This variant was not pursued because it failed to show complete monomerization in the absence of metal ions.

The variant ^{60A}MIC1 was also crystallographically characterized, with a protein crystal structure obtained at a resolution of 2.20 Å. The refinement statistics for this structure are summarized in Table A2.3, with crystal growth conditions given in Table A2.2. Crystal growth was facilitated by the addition of Cu^{II}, and these metal ions were found present at both the 3His coordination sites (the fourth His at position 60 and 60' is now an Ala) as well as the ferroxidase center (Figure A2.2). The copper ions located at the 3His clamps appear coordinatively unsaturated (the resolution of the crystal structure did not permit placement of water molecules near these copper centers) which could have interesting redox-chemistry implications. The structure of ^{A60}MIC1 superimposes well with that of MIC1, with an rmsd over all C_α positions measured at 0.196 Å. As in the Cu-bound crystal structure of MIC1, residue D42 assumes multiple conformations, due to repulsive interactions with E74'. As in the case of ^{D32}4His-ΔC*, the metal-responsive assembly properties of ^{A60}MIC1 did not warrant its further experimental pursuit.

MIC1 Molar Ellipticity Data Conversion and α-Helical Content Analysis

Circular dichroism studies of the MIC1 protein (in both its monomeric and Cu-induced cage forms) were performed to determine the nature of MIC1 secondary structure and probe whether 24-merization results in increased helical content. Additionally, CD spectra of monomeric MIC1 in the presence of Cu^{II}, Ni^{II}, and Zn^{II} were collected to ascertain the extent to which these divalent late-first-row transition metal ions preorganize monomers for dimerization at dilute concentrations (see Figure 3.7 A). The data presented in the figure show molar ellipticity as a function of wavelength. The CD experiments themselves provide measurements in terms of CD signal as a function of wavelength probed, and therefore to create the given plot, CD signal had to be converted to molar ellipticity.

Conversion of CD signal to molar ellipticity, or [θ], involves utilization of the following relationship, which is outlined in Juban *et al.*:

$$[\theta] = [\theta]_{obs}*(MRW/10cd)$$

where $[\theta]_{obs}$ is the experimentally measured CD signal or ellipticity, MRW is the mean residue molecular weight of the protein (molecular weight divided by the number of peptide bonds), c is the concentration of the sample in mg/mL, and d is the optical pathlength of the cuvette in cm.[3] The overall units of [θ] are generally presented in $[\theta] \times 10^{-3} deg*cm^2*dmol^{-1}$. In the case of the MIC1 measurements, the value of MRW was found by the ratio of 21,024.52 g/mol and 181 peptide bonds. The concentration of the protein utilized, c, was ~0.042 mg/mL. The pathlength of the cell, d, was 1 cm.

Along with MIC1 molar ellipticities, the percent of α-helical content was determined for the various states of MIC1 outlined in Figure 3.7 A. The percentages of α-helicity were calculated using data from both 208- and 222 nm CD signatures; these values are summarized in Table A3.1. The percentage of α-helicity of the MIC1 proteins corresponding to CD measurements made at 208 nm was found with the method of Greenfield *et al.*[4] Essentially, helicity is given by the ratio:

$$\% \ \alpha\text{-helix} = \frac{[\theta]_{208nm} - 4{,}000}{33{,}000 - 4{,}000}$$

Alternatively, employing the strategy of McLean *et al.*, the percentage of α-helicity can be calculated with CD signal monitored at 222 nm.[5] This approach uses the formula:

$$\% \ \alpha\text{-helix} = \frac{-100([\theta]_{222nm} + 3{,}000)}{33{,}000}$$

Both methods for exploring the helical content of the MIC1 mutant in various states yield results fairly consistent with one another, with α-helicity in all cases found to be ~40%.

Data Fitting and Analysis of MIC1 Unfolding Titrations

Chemical unfolding experiments were performed on the MIC1 HuHF variant in several oligomeric states with guanidine hydrochloride (GuHCl) as denaturant. The results of the titrations are presented in Figure 3.7 B, where the fraction of unfolded protein (f_U) is plotted as a function of [GuHCl]. Curves were fit to the plots assuming a two-state folding-unfolding process. The curve for monomeric apo-MIC1 was fit using Kaleidagraph (Synergy Software) to the expression:

$$f_U = \frac{e^{\left(\frac{-\mathrm{m1} \times (\mathrm{m2} - [\mathrm{GuHCl}])}{\mathrm{RT}}\right)}}{1 + e^{\left(\frac{(-\mathrm{m1} \times (\mathrm{m2} - [\mathrm{GuHCl}]))}{\mathrm{RT}}\right)}}$$

where m1 is the slope of the unfolding transition, m2 is the midpoint GuHCl concentration for unfolding, or $[\mathrm{GuHCl}]_u$, R is the universal gas constant, and T is temperature. m1 relates the free energy of folding ($\Delta G_{folding}$) and [GuHCl] as described by Pace *et al.*[6] using the relationship:

$$\Delta G_{folding} = \Delta G^{\circ}_{folding} + m1[\mathrm{GuHCl}]$$

where $\Delta G^{\circ}_{folding}$ is the folding free energy at [GuHCl] = 0 M. Given that $\Delta G_{folding} = 0$ at the transition midpoint ($m2 = [\mathrm{GuHCl}]_m$), it follows that $\Delta G^{\circ}_{folding} = m2 \times [\mathrm{GuHCl}]_m$.

For obtaining the folding free energy of the cages, we assumed a “folded 24mer-to-unfolded monomer” equilibrium with no observable intermediates; this assumption follows the treatment of Swift *et al.*[7] in fitting similar data obtained for dodecameric ferritin-like protein Dps. The chemical denaturation data were treated by plotting [GuHCl] against the free energy ($\Delta G_{folding}/n$) of folding for the 24mer protein cage on a per subunit basis, where n = 24 (see Figure 3.9). The expression employed in the calculation of $\Delta G_{folding}$ is:

$$\Delta G_{folding} = -RT\ln(f_{Ft}/nf_U) + (n-1)RT\ln(f_U P_t).$$

In this expression, f_U is again defined as the fraction of unfolded protein. f_{Ft} is the fraction of total folded protein present as both monomer and 24mer and is given by $f_{Ft} = 1-f_U$. P_t represents the total protein concentration in mol/L. As before, R is the universal gas constant and T is the temperature. $G_{folding}{}^{\circ}/n$ for each cage variant was obtained by extrapolating the linear region of the $\Delta G_{folding}/n$ versus [GuHCl] curve to 0 M GuHCl, again using the assumption by Pace.[6] The equations for these linear fits are given on Figure 3.9.

Thermal unfolding experiments were conducted on the MIC1 protein in various oligomeric states to compliment the chemical denaturation titrations. Although the thermal unfolding of HuHF variants is not completely reversible, as seen with MIC1, the resulting unfolding curves were fit to a two-state model as described by John and Weeks[8] to obtain an apparent midpoint of denaturation, T_m. The thermal unfolding plots are given in Figure 3.7 C. Unfolding data were fit with the following relationship using Kaleidagraph:

$$f_U = \frac{e^{\left(\left(\frac{\Delta H_{vH}}{R}\right)\times\left(\left(\frac{1}{T_m}\right)-\left(\frac{1}{T}\right)\right)\right)}}{1+e^{\left(\left(\frac{\Delta H_{vH}}{R}\right)\times\left(\left(\frac{1}{T_m}\right)-\left(\frac{1}{T}\right)\right)\right)}}$$

Here, f_U represents the fraction of unfolded protein, ΔH_{vH} is the change in the van't Hoff transition enthalpy, R is the universal gas constant, T_m stands for the melting point (which determines the transition midpoint), and T is the temperature in Kelvin.

Table A1.1. Amino acid (top) and DNA (bottom) sequences of wild-type HuHF. Residue numbers (in bold) at left flank the sequence columns.

1	T ACC	T ACT	A GCT	S AGC	T ACC	S AGC	Q CAA	V GTT	R CGT	Q CAA
11	N AAC	Y TAT	H CAT	Q CAA	D GAT	S AGC	E GAA	A GCA	A GCG	I ATT
21	N AAC	R CGC	Q CAG	I ATT	N AAC	L TTG	E GAG	L CTG	Y TAT	A GCG
31	S TCG	Y TAC	V GTT	Y TAT	L CTG	S TCT	M ATG	S AGC	Y TAT	Y TAC
41	F TTC	D GAC	R CGT	D GAC	D GAT	V GTG	A GCC	L CTG	K AAA	N AAC
51	F TTT	A GCG	K AAA	Y TAC	F TTC	L CTG	H CAT	Q CAG	S AGC	H CAT
61	E GAA	E GAA	R CGC	E GAG	H CAC	A GCA	E GAG	K AAA	L CTG	M ATG
71	K AAA	L CTG	Q CAG	N AAT	Q CAG	R CGT	G GGT	G GGC	R CGC	I ATC
81	F TTT	L CTG	Q CAG	D GAC	I ATT	K AAG	K AAG	P CCG	D GAT	C TGC
91	D GAC	D GAT	W TGG	E GAA	S AGC	G GGC	L CTG	N AAT	A GCG	M ATG
101	E GAG	C TGT	A GCG	L CTG	H CAT	L CTG	E GAG	K AAG	N AAT	V GTC
111	N AAT	Q CAG	S AGC	L CTG	L CTG	E GAG	L CTG	H CAC	K AAG	L CTG
121	A GCA	T ACG	D GAT	K AAG	N AAT	D GAT	P CCG	H CAC	L CTG	C TGC
131	D GAT	F TTC	I ATC	E GAA	T ACG	H CAT	Y TAC	L CTG	N AAC	E GAG
141	Q CAA	V GTG	K AAA	A GCG	I ATC	K AAA	E GAG	L TTG	G GGC	D GAC
151	H CAC	V GTC	T ACC	N AAC	L CTG	R CGT	K AAG	M ATG	G GGT	A GCA
161	P CCG	E GAA	S TCC	G GGT	L CTG	A GCC	E GAG	Y TAC	L CTG	F TTT
171	D GAC	K AAG	H CAC	T ACC	L TTG	G GGT	D GAC	S TCC	D GAC	N AAT
181	E GAA	S AGC								

TTASTSQVRQNYHQDSEAAINRQINLELYASYVYLSMSYYFDRDDVALKNFAK

YFLHQSHEEREHAEKLMKLQNQRGGRIFLQDIKKPDCDDWESGLNAMECALH

LEKNVNQSLLELHKLATDKNDPHLCDFIETHYLNEQVKAIKELGDHVTNLRKMG

APESGLAEYLFDKHTLGDSDNES

Figure A1.1. The primary structure of wild-type HuHF. The amino acids are color-coded to reflect the four different α-helices (A-D) as well as the BC loop region. Helix A is colored blue. Helix B is highlighted with red coloration. Helix C is colored purple. Helix D is shown with orange coloration. The BC loop region is indicated with green coloring.

Table A1.2. Primers utilized toward the preparation of ΔC* from wild-type HuHF.

Variant	Mutation (order of addition)	Primer Sequence (5’-3’)
ΔC*	K86Q + C90E	GCAGGACATTCAGAAGCCGGATGAGGACGATTGGG
		CCCAATCGTCCTCATCCGGCTTCTGAATGTCCTGC
	C102A	GGCCTGAATGCGATGGAGGCGGCGCTGCATCTGG
		CCAGATGCAGCGCCGCCTCCATCGCATTCAGGCC
	C130A	GAATGATCCGCACCTGGCGGATTTCATCGAAACGC
		GCGTTTCGATGAAATCCGCCAGGTGCGGATCATTC

Table A1.3. Primers employed to prepare variants 4His-ΔC* and 4His-loop-ΔC*, which display metal coordination motifs, from the ΔC* template.

Variant	**Mutation (order of addition)**	**Primer Sequence (5'-3')**
4HisΔC*	R63H	GCCATGAAGAACACGAGCACGCAGAG
		CTCTGCGTGCTCGTGTTCTTCATGGC
	L56H	GAAAAACTTTGCGAAATACTTCCATCATCAGAGCCATGAAGAACACG
		CGTGTTCTTCATGGCTCTGATGATGGAAGTATTTCGCAAAGTTTTTC
	E67H	TGAAGAACACGAGCACGCACATAAACTGATGAAACTGCAGA
		TCTGCAGTTTCATCAGTTTATGTGCGTGCTCGTGTTCTTCA
4His-loop-ΔC*	F81H + Q83H	CGTGGTGGCCGCATCCATCTGCATGACATTCAGAAGCCG
		CGGCTTCTGAATGTCATGCAGATGGATGCGGCCACCACG
	K87H + D91H	CTGCATGACATTCAGCATCCGGATGAGCACGATTGGGAAAGCG
		CGCTTTCCCAATCGTGCTCATCCGGATGCTGAATGTCATGCAG

Table A1.4. Primers utilized in the mutagenic C_2 interface perturbation screen. The mutations were performed on either the 4His-ΔC* or 4His-loop-ΔC* templates. All mutations were designed to be compatible with one another on the two templates, with the exception of the pair L28E and Y32D. The variant moved forward with following this mutagenic screen, MIC1, contains mutations Y39E, N74E, and P88A on the 4His-ΔC* template.

Mutation	**Primer Sequence (5'-3')**
L28E	CCGCCAGATTAACTTGGAGGAGTATGCGTCGTACGTTTAT
	ATAAACGTACGACGCATACTCCTCCAAGTTAATCTGGCGG
Y32D	TGGAGCTGTATGCGTCGGACGTTTATCTGTCTATG
	CATAGACAGATAAACGTCCGACGCATACAGCTCCA
Y39D	GTTTATCTGTCTATGAGCGATTACTTCGACCGTGACG
	CGTCACGGTCGAAGTAATCGCTCATAGACAGATAAAC
Y39E	GTTTATCTGTCTATGAGCGAGTACTTCGACCGTGACGATG
	CATCGTCACGGTCGAAGTACTCGCTCATAGACAGATAAAC
Y39K	GTTTATCTGTCTATGAGCAAGTACTTCGACCGTGACGATG
	CATCGTCACGGTCGAAGTACTTGCTCATAGACAGATAAAC
N74E	CTGATGAAACTGCAGGAGCAGCGTGGTGGCCGC
	GCGGCCACCACGCTGCTCCTGCAGTTTCATCAG
I85D	GCATCTTTCTGCAGGACGATCAGAAGCCGGATGAGG
	CCTCATCCGGCTTCTGATCGTCCTGCAGAAAGATGC
P88A	GCAGGACATTCAGAAGGCGGATGAGGACGATTG
	CAATCGTCCTCATCCGCCTTCTGAATGTCCTGC
H128A	CGGATAAGAATGATCCGGCCCTGGCGGATTTCATCG
	CGATGAAATCCGCCAGGGCCGGATCATTCTTATCCG

Table A1.5. List of mutagenic primers employed toward the installment of cysteine residues on the MIC1 template for protein modification with thiol-reactive substrates.

Variant	**Mutation**	**Primer Sequence (5'-3')**
^{C53}MIC1	K53C	GTGGCCCTGAAAAACTTTGCGTGCTACTTCCATCATCAGAGCCAT
		ATGGCTCTGATGATGGAAGTAGCACGCAAAGTTTTTCAGGGCCAC
^{C57}MIC1	H57C	CCCTGAAAAACTTTGCGAAATACTTCCATTGTCAGAGCCATGAAGAA
		TTCTTCATGGCTCTGACAATGGAAGTATTTCGCAAAGTTTTTCAGGG
^{C136}MIC1	H136C	GGCGGATTTCATCGAAACGTGTTACCTGAACGAGCAAGTG
		CACTTGCTCGTTCAGGTAACACGTTTCGATGAAATCCGCC
^{C143}MIC1	K143C	CATTACCTGAACGAGCAAGTGTGCGCGATCAAAGAGTTGGGCGAC
		GTCGCCCAACTCTTTGATCGCGCACACTTGCTCGTTCAGGTAATG

Table A1.6. Table of primers related to mutations geared toward the possible destabilization of the MIC1 template to probe Cu^{II}-induced self-assembly properties of the HuHF variant. MIC1 is the starting material for all of the mutations.

Variant	**Mutation (order of addition)**	**Primer Sequence (5'-3')**
^{60A}MIC1	H60A	TACTTCCATCATCAGAGCGCTGAAGAACACGAGCACGC
		GCGTGCTCGTGTTCTTCAGCGCTCTGATGATGGAAGTA
MIC1 reversion mutant	H56L	CTTTGCGAAATACTTCCTGCATCAGAGCCATGAAGAACACG
		CGTGTTCTTCATGGCTCTGATGCAGGAAGTATTTCGCAAAG
	H63R + H67E	CAGAGCCATGAAGAACGCGAGCACGCAGAGAAACTGATGAAACTGC
		GCAGTTTCATCAGTTTCTCTGCGTGCTCGCGTTCTTCATGGCTCTG
$^{A131/134}$MIC1	D131A + E134A	CCGCACCTGGCGGCTTTCATCGCAACGCATTACCTG
		CAGGTAATGCGTTGCGATGAAAGCCGCCAGGTGCG
^{A173}MIC1	H173A	AGTACCTGTTTGACAAGGCCACCTTGGGTGACTCCG
		CGGAGTCACCCAAGGTGGCCTTGTCAAACAGGTACT

Table A2.1. X-ray data collection and refinement statistics for the protein crystal structure of Cu-, Zn-^{D32}4His-ΔC*. *denotes the highest resolution shell.

	Cu-, Zn-^{D32}4His-ΔC*
Data Collection Location	SSRL BL 7-1
Unit Cell Dimensions	a = b = c = 180.1 Å
	$\alpha = \beta = \gamma = 90°$
Symmetry Group	F432
Resolution (Å)	104.0-2.30
X-Ray Wavelength (Å)	0.98
Number of Unique Reflections	11647
Redundancy	15.3
Completeness (%)*	100 (99.9)
$\langle I/\sigma I \rangle$*	4.0 (1.4)
R_{symm} (%)*	16.3 (54.3)
R_{work} (%)*	16.3 (17.0)
R_{free} (%)*	20.3 (21.4)
Number of Atoms	
Protein (including alternative side chain conformations)	1415
Ligands/Ions	14
Water	86
B-Factors (Å^2)	
Protein	12.7
Ligands/Ions	41.7
Water	16.5
RMS Deviations	
Bond Lengths (Å)	0.022
Bond Angles (^{o})	1.681
Ramachandran plot (%)	
Residues in favored regions	97.0
Residues in allowed regions	3.0
Residues in generously allowed regions	0.0
Residues in disallowed regions	0.0

Table A2.2. Table of crystal growth conditions. The sitting drops each consisted of 2 μL protein solution and 2 μL precipitant solution. The wells contained 500 μL precipitant solution.

Protein Crystal	**Temp.**	**Protein**	**Precipitant**
Cu-, Zn-^{D32}4His-ΔC*	25 °C	591 μM in 15 mM Tris (pH 7.4) buffer with 150 mM NaCl	50 mM Tris (pH 8.0), 5 mM $CaCl_2$, 9% (m/v) PEG 6000, 600 μM $ZnCl_2$
Cu-^{A60}MIC1	25 °C	685 μM in 15 mM Tris (pH 7.4) buffer with 150 mM NaCl	50 mM Tris (pH 8.0), 10 mM $CaCl_2$, 50mM NaCl, 10% (m/v) PEG 1900 MME, 700 μM $CuCl_2$

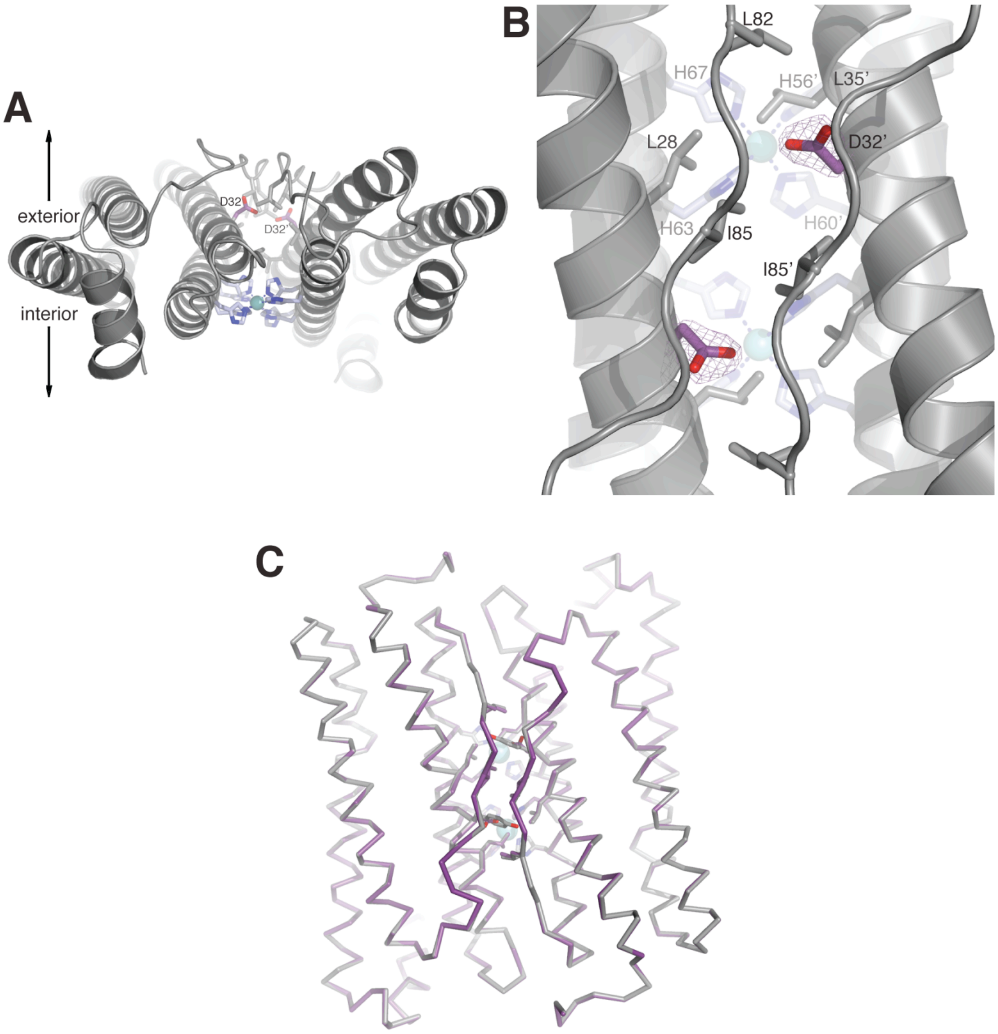

Figure A2.1. Structural features of the C_2 dimer of ^{D32}4His-ΔC*. A) View down the C_2 interface of ^{D32}4His-ΔC*, highlighting the D32 mutation (violet-purple sticks) in the context of the interior of the interface. The 4His coordination motif shows Cu^{II} binding (blue dashes connected to aquamarine spheres representing the metal ions). B) Close-up view of the dimer interface, looking in from the outside of the ferritin cage. The $2F_o$-F_c electron density map of D32 is shown as a violet-purple mesh contoured at 1.6σ. C) Backbone superposition of the C_2 dimers of ^{D32}4His-ΔC* (violet-purple) and 4His-ΔC* (gray) demonstrating their near isostructural nature.

Table A2.3. X-ray data collection and refinement statistics for the protein crystal structure of Cu-^{A60}MIC1. * denotes the highest resolution shell.

	Cu-^{A60}MIC1
Data Collection Location	SSRL BL 9-2
Unit Cell Dimensions	a = b = c = 181.2 Å
	$\alpha = \beta = \gamma = 90°$
Symmetry Group	F432
Resolution (Å)	104.6-2.20
X-Ray Wavelength (Å)	0.98
Number of Unique Reflections	13501
Redundancy	29.7
Completeness (%)*	100 (100)
$\langle I/\sigma I\rangle$*	7.5 (2.7)
R_{symm} (%)*	37.3 (85.6)
R_{work} (%)*	23.6 (68.4)
R_{free} (%)*	27.1 (69.6)
Number of Atoms	
Protein (including alternative side chain conformations)	1412
Ligands/Ions	6
Water	50
B-Factors (Å^2)	
Protein	13.8
Ligands/Ions	50.1
Water	16.4
RMS Deviations	
Bond Lengths (Å)	0.021
Bond Angles (^{o})	1.664
Ramachandran plot (%)	
Residues in favored regions	97.0
Residues in allowed regions	2.4
Residues in generously allowed regions	0.0
Residues in disallowed regions	0.6

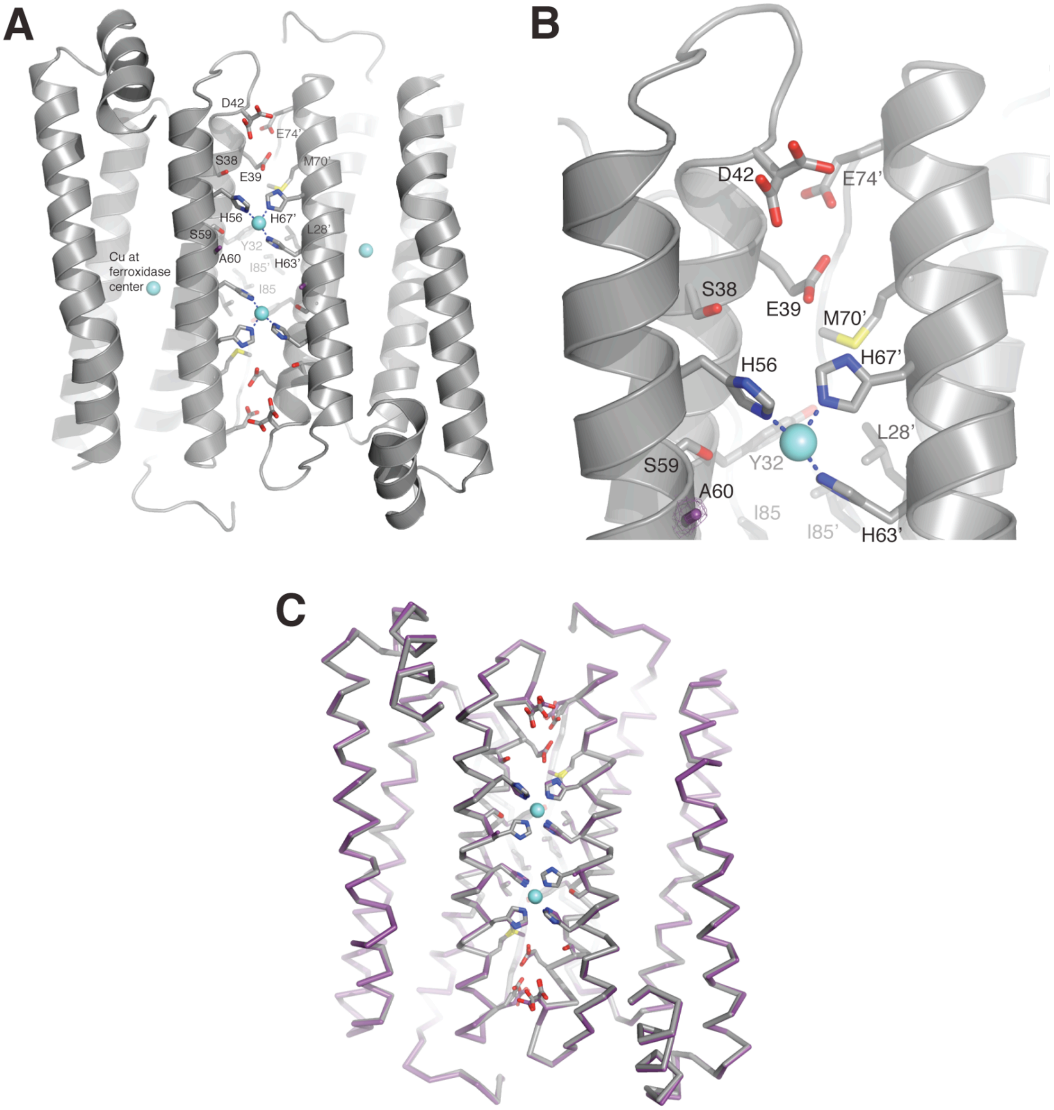

Figure A2.2. Structural characterization of Cu-bound ^{A60}MIC1. A) View of the C_2 dimer of Cu-^{A60}MIC1 with Cu^{II} ions (aquamarine spheres) bound to the 3His clamps and the ferroxidase center. No water molecules could be placed to saturate the coordination sphere of the Cu^{II} ions. The H60A mutation is highlighted in violet-purple. B) Close-up view of the inner C_2 dimer interface, highlighting the 3His coordination motif, with metal binding indicated with blue dashes. The mutated residue A60 is shown wrapped in a violet-purple mesh representing the $2F_o$-F_c electron density map contoured at 1.6σ. Residue D42, as in the case of MIC1, assumes multiple conformations due to electrostatic clashes with E74. C) Backbone superposition of Cu-adducts of ^{A60}MIC1 (violet-purple) and MIC1 (gray), emphasizing minimal structural changes attributed to the H60A mutation.

Table A3.1. Table presenting calculated values for the α-helical content of MIC1 in the states discussed in Figure 3.1 A.

MIC1 State	**% α-Helix, 208 nm Calculation**	**% α-Helix, 222 nm Calculation**
Monomer	36.7	40.4
Cu^{II}-Induced Cage	35.2	45.6
Monomer + 1:1 Cu^{II}	36.1	41.0
Monomer + 1:1 Ni^{II}	38.1	42.0
Monomer + 1:1 Zn^{II}	37.9	42.4

References

1. Santambrogio, P., et al., *Effects of modifications near the 2-, 3- and 4-fold symmetry axes an human ferritin renaturation.* Biochemical Journal, 1997. **322**: p. 461-468.

2. Lawson, D.M., et al., *Solving the Structure of Human H-Ferritin by Genetically Engineering Intermolecular Crystal Contacts.* Nature, 1991. **349**(6309): p. 541-544.

3. Juban, M.M., M.M. Javadpour, and M.D. Barkley, *Circular dichroism studies of secondary structure of peptides.* Methods in Molecular Biology, 1997. **78**: p. 73-78.

4. Greenfield, N. and G.D. Fasman, *Computed circular dichroism spectra for the evaluation of protein conformation.* Biochemistry, 1969. **8**(10): p. 4108-4116.

5. McLean, L.R., et al., *Minimal peptide length for interaction of amphipathic alpha-helical peptides with phosphatidylcholine liposomes.* Biochemistry, 1991. **30**(1): p. 31-37.

6. Pace, N.C. and B.A. Shirley, *Protein Structure: A Practical Approach* ed. T.F. Creighton. 1990, Oxford: IRL Press.

7. Swift, J., et al., *Design of functional ferritin-like proteins with hydrophobic cavities.* Journal of the American Chemical Society, 2006. **128**(20): p. 6611-6619.

8. John, D.M. and K.M. Weeks, *van't Hoff enthalpies without baselines.* Protein Science, 2000. **9**(7): p. 1416-1419.